UNIVERSITA' DEGLI STUDI DI BERGAMO
Facoltà di Ingegneria
Dipartimento di Ingegneria Industriale

DOTTORATO DI RICERCA
IN
TECNOLOGIE PER L'ENERGIA E L'AMBIENTE

XXII ciclo

Anno 2010

INVESTIGATIONS ON THE FLOW INSIDE PUMPS BY MEANS OF 2D PARTICLE IMAGE VELOCIMETRY

Tesi di Dottorato di:
Rinaldo Miorini

Abstract

This work is concerned with the sampling, evaluating and critically interpreting of fluid dynamics phenomena inside two radically different pumps. Large scale flow structures are investigated in the vaned diffuser of a centrifugal pump and in the rotor passage of a water jet axial pump by means of two-dimensional particle image velocimetry (2DPIV).

In the first part of the work, a centrifugal pump is run at various capacities to derive information about the flow around the diffuser vanes. Preliminarily, time resolved pressure measurements have indicated the presence of very large scale non-periodic flow instability at very low flow-rates. Phase-averaged PIV measurements are performed at midspan over the blade to blade plane in the diffuser to describe both the channel flow and the wakes, which indeed dominate the flow in the diffuser. The flow is separated at the convex side of the diffuser vanes at reduced capacities, i.e. below the best efficiency point (BEP). Wakes shed from the impeller are convected in the diffuser passages and distorted because of the different transport velocity at the convex and concave sides of the vane. The measurements have been performed at Laboratorio di Fluidodinamica delle Macchine (LFM) at Politecnico di Milano, Milan, Italy.

In the second part, the tip leakage flow (TLF), tip leakage vortex (TLV) and the vorticity shed by the blade tip are investigated in the meridional plane of an axial pump to shed light over the inner structure of the vortices that develop in the passage, as well as the production of vorticity at the casing end-wall, induced by the presence of the TLV. Turbulence inside the TLV is also investigated. The rolling up of the TLV induces the detachment of the end-wall boundary layer vorticity, the detached flow rearranges in vortices - counter rotating respect with the TLV - that orbit around the TLV centerline and are interlaced with the TLV vorticity until its bursting. The detachment of the end-wall vorticity is unsteady and high level of in plane production of turbulent kinetic energy is found there. The vorticity layer that connects the blade and the TLV is also unsteady and source of large scale unsteadiness; the core of the TLV is unsteady but in plane production of turbulence is almost absent there. The experiments have been performed at the Department of Mechanical Engineering, The Johns Hopkins University (JHU), Baltimore, MD, USA.

Key words: axial pump, centrifugal pump, diffuser, particle image velocimetry, phase average, rotor, tip leakage vortex, wake.

Advisor:

- Prof. Marco Savini - Dipartimento di Ingegneria Industriale, Università degli Studi di Bergamo

Acknowledgements

I would like to gratefully acknowledge Eng. Arnaldo Boccazzi.

I would like to thank all the colleagues and friends working at the LFM Lab. at Politecnico di Milano: Prof. Vincenzo Dossena, Eng. Paolo Gaetani, Eng. Giacomo Persico, Eng. Alessandro Mora, Eng. Gabriele D'Ippolito, Eng. Franco Marinoni, Claudio De Ponti and Paolo Grigatti. Special thanks to Prof. Carlo Osnaghi, it all began attending his Turbomachinery class.

Special thanks to the graduate students and friends at Università degli Studi di Bergamo, and to my PhD advisor Prof. Marco Savini.

I would like to thank my colleagues and friends at the Hopkins: Ming Ming Zhang, Siddartha 'Sid' Talapatra, Jeff Cullina, Kunlun Bai, Balaji Gopalan, Jiarong 'Jerry' Hong, Pranav Joshi, Yuan Lu, Benjamin 'Ben' de Witt, Xiaofeng Liu, Yury Ronzhes and Stephen King; special thanks to Huixuan Wu.

I gratefully acknowledge Prof. Joseph Katz for the opportunity of working in his Lab. and for having changed my perspective on Fluid Dynamics and research in general.

Contents

Nomenclature

Roman letters

b	Blade span [m]
c	Chord [m]
C	Casing curvature [m^{-1}]
D	Impeller diameter or reference flow length [m]
D_{R}	Rotor diameter in the axial pump [m]
f	Frequency [Hz]
g	Gravitational constant [ms^{-2}]
h	tip clearance width [m]
h_{b}	Blade pitch [m]
H	Total head [m]
k_{M}	Torque coefficient
k^*_{2D}	Normalized in plane turbulent kinetic energy
p	Pressure [Pa]
P	Production of turbulent kinetic energy [$\mathrm{m}^2\mathrm{s}^{-3}$]
P^*_{2D}	Normalized, planar production of turbulent kinetic energy
Q	Flow rate [$\mathrm{m}^3\mathrm{s}^{-1}$]
r	radial coordinate [m]
s	Solidity (c/h_b)
S_{ij}	Strain-rate tensor [s^{-1}]
T	Time scale, period [s]
t	Time [s]
U	Characteristic velocity [ms^{-1}]
$\bar{\bar{\mathbf{U}}}$	steady state velocity field [ms^{-1}]
$\bar{\mathbf{U}}$	unsteady velocity induced by the impeller round in the diffuser [ms^{-1}]
$\mathbf{U}^{\mathrm{S}}$	unsteady velocity induced by the impeller passage in the diffuser [ms^{-1}]
$\mathbf{U}, (U, V)$	Averaged velocity, components [ms^{-1}]
$\hat{\mathbf{u}}$	Instantaneous velocity [ms^{-1}]
$\mathbf{u}, (u, v)$	Velocity fluctuation, components (in the centrifugal pump) [ms^{-1}]
$\mathbf{u}', (u'_{\mathrm{r}}, u'_\theta, u'_{\mathrm{z}})$	Velocity fluctuation, components (in the axial pump) [ms^{-1}]
$\mathbf{x}$	Position [m]
z	axial coordinate [m]

Greek letters

Δ	Cyclic unsteadiness, or difference
δ	Delta function, or vector spacing [m]
ρ	Mass per unit volume [kgm^{-3}]
ϕ	Flow coefficient
φ	Rotor phase [°]
ψ	Head coefficient
θ	Circumferential coordinate
ω	Vorticity [s^{-1}]
Ω	Rotating frequency of the shaft [Hz]
Ω_{ij}	Spin tensor [s−1]
ω_s	Specific speed

Subscripts

On any variable X:

X_0	Initial, upstream value
X_1, X_3	Value at inlet section of the impeller, diffuser
X_2, X_4	Value at discharge section of the impeller, diffuser
X_{BEP}	Value at Best Efficiency Point
X_{g}	Geometrical value
X_{max}	Maximum value
X_{H}	Value at blade hub
X_{TIP}	Value at blade tip
X_{z}	Component along the axis of the pump
X_{tng}, X_θ	Component along the tangential direction respect with the rotor

Superscripts and other qualifiers

On any variable X:

X^{T}	total (reservoir) value
X^{S}	in the stator frame of reference
X^{R}	in the rotor frame of reference
$< X >$	ensemble average
$\bar{X}$	mean value

Part I

The Transport of Wakes from the Impeller Through the Vaned Diffuser of a High Specific Speed Centrifugal Pump

Introduction

The Diffuser of a Centrifugal Pump

The specific speed of a pump characterizes its geometry. Given the definition of specific speed, which is not universal, its range spans all the possible applications. It is known that high specific speed pumps are axial, their rotors have broad passages and blades impose a downstream positive static pressure gradient through the aerodynamic action.

The performance of axial pumps decays considerably at low flow-rates because the incidence angle increases, due to tangential realignment of the relative inlet velocity. Profile overloading induces flow separation, and hence diminished performance, and cavitation because of large leading edge depressurization. Moreover, axial machines specifically designed for running at low flow-rates and high heads have high solidities and large wet surfaces.

Low specific speed turbo-pumps are normally centrifugal, they are designed to deliver relatively low flow-rates at high heads by means of the work done by the rotating impeller. It is worth to highlight that the great part of the installed industrial centrifugal pumps have very simplified impeller blades, often merely curved plates; in fact, the source of head is not the aerodynamical performance of the blade but the swirl imposed by the impeller on the flow. High performance centrifugal turbo-pumps are designed to maximize the work, and hence the designing and machining of the impeller blades are accurate.

The pressure jump imposed by the centrifugal action can induce very high pressure at the discharge section of the impeller; in single stage, high head pumps or in multi stage machines the static pressure in the volute largely stresses the casing structure. In order to avoid the casting of heavy and expensive shells, the two halves of the volute can be connected internally by vanes that support the containing stress. Moreover, the flow exits the impeller with relatively large discharge velocity, from which static pressure can be partially recovered. In order to obtain a robust casing structure and to recover pressure, stator vanes must be properly shaped and oriented, to minimize head losses while imposing radial suction on the flow discharged by the impeller, which would otherwise proceed over logarithmic spiral streamlines; this stator is commonly called diffuser.

A properly designed diffuser collects the flow from the impeller through a inlet inter-vane passage whose concave side is commonly a log-spiral close to the leading edge, and proceeds more radially than the spiral in the second part; vanes thickness must be sufficiently large to ensure structural strength. The suction action allows the diffuser to recover pressure while keeping a compact design, but extreme forcing of the compression induces separation on the vanes and decreased performance.

Probing the Flow

In order to validate the design of a diffuser, the pressure-velocity distribution must be sampled on its inside. Static pressure taps have been used in countless investigations both in diffusers and volutes to characterize head losses and, on top of all, unsteadiness; in fact, reliability, cavitation damage and noise are prominent topics in the design of centrifugal pumps.

Directional, point to point probes can be used inside a centrifugal pump with one main advantage, a direct measure of pressure, and many limitations. Assumed that the probe head size is negligible compared with the scale of the machine, and that is not always easy to accomplish, probes must be inserted and oriented avoiding leakage at the stem penetration. As a result, hydro-turbomachines are very difficult to study as the head of the probe must be moved in the inner space while the stem is constrained by a sealed hole. The yaw movement of the probe is allowed but rolling and pitching are

impossible. If the shaft speed is scaled in order to maintain the value of the Reynolds number unchanged, and the fluid is air instead of water, then total pressure probes and hot-wires can be adopted in turbo-pumps, but not every flow feature in the machine follows such a straightforward scaling.

If several probes are mounted at the same time, measurements can be multi-point and instantaneous, assuming that the leakage at the stem is not an issue, but each probe must be placed at the correspondent node of the measurement mesh, inducing flow blockage and mutual disturbances. On the other hand, single probes can be moved over limited paths with sufficient spatial resolution, but then measurement are made at different instants, and only time averaged results can be derived. Large spatial resolution, instantaneous measurements of the flow are precluded to point-to-point probe systems, included Laser Doppler Velocimetry (LDV). Unsteady LDV measurements are less common than unsteady pressure measurements, for instance, researches are performed by Blanco *et al.* [1], Wang and Tsukamoto [2], Ullum *et al.* [3]) and Pavesi *et al.* [4]. The application of LDV over turbulent flows needs some attention; while computing the phase-averaged or total averaged velocity is straightforward, turbulence statistics must be properly evaluated because the velocity is sampled unevenly in time.

CFD and Turbulence Modelling

Turbomachines can be modified in order to host point-to-point probe systems in selected sections, for example the inflow of a turbine stator. Then, the downstream evolution of the flow can be computed by means of Computational Fluid Dynamics (CFD) techniques to predict the performance of a stage and to improve the design.

The CFD approach resolves the problem of fitting many probes in inter-blade channels, providing data enough resolved in space-time to allow the computation of gradients and accurate integrals. The constantly increasing computational power available and the research work of many scientists is providing effective tools both for the analysis and the design of machines.

Both universities and industries adopt CFD largely nowadays. Academic researches are mainly concerned with the detailed investigation of the flow inside a designed or existing machine while engineers need a fast and reliable design tool.

CFD codes have been on the market for years, the most popular ones are based on finite-volume algorithms and solve the continuity, momentum and energy equations over large grids in order to save CPU time, the momentum equation is usually approached with the Reynolds Averaged Navier-Stokes (RANS) technique or the Unsteady RANS (URANS) when the flow is forced by a deterministic external phenomenon. Therefore, interactions with walls and turbulence must be modelled along with the application of wall-functions - when needed - and closure equations. Popular turbulence models are the $k - \varepsilon$, largely adopted on hydro-turbomachines, fans and blowers and the Shear Stress Transport (SST), see Menter [5]. RANS computations are particularly suitable for the evaluation of the mean pressure field in a pump, assuming that it is not working too far from the Best Efficiency Point (BEP), details can be fond in Shi and Tsukamoto [6], Sano *et al.* [7], and Majidi [8], for instance.

In the industry, the rotor-stator interaction is usually investigated with a rough URANS approach called frozen rotor in which the steady state flow is computed at different rotor phases that are fixed in time, and the result is a surrogated of the phase averaged flow. Because the flow in a machine is never in equilibrium, the quasi-static approach fails and the frozen rotor has large limitations, although faster to compute and implement than a proper, time resolved computation.

Particle Image Velocimetry

Universal closure equations that predict turbulence well in a generalized flow are far from being formulated. This is proven by the amount of closure laws available, each one tuned to a particular class of flows. Moreover, closure equations contain coefficients whose value is to be evaluated from detailed statistics of simple flows as shown for example by Johansson and George [9].

Indeed, the simulation of a centrifugal machine can provide accurate and reliable large scale data, i.e. head and efficiency curve, static pressure distribution in the volute at steady state, etc. Detailed inner flow feature can be computed only taking great care of the code and mesh, tuning the closure equations and choosing the correct wall functions, when needed. Even if those points were well covered, a model that predicts the flow in a zone of the machine might be incorrect for the rest because turbomachinery flows are always three dimensional with high Reynolds number, and the flow is anisotropous and unbalanced, thus difficult to model. A detailed prediction of the inner flow in a turbomachine is not available industrially, at this time.

Particle image velocimetry (PIV) provides detailed and instantaneous velocity distributions. PIV results look very similar to CFD outputs because the dataset is given instantaneously on a mesh, and they are useful in the study of machines in steady or transient state. PIV velocity maps can be as spatially resolute as the inertial scale, or more; thus, velocity gradients are reliable and vorticity/strain-rate distributions can be accurate. In fact, boundary layers, stagnation points and separated flows can be studied in detail.

PIV can be performed with various techniques, the simplest one is the 2DPIV, adopted in this research, in which a region is illuminated by a laser plane, the light scattered by the seeding particles in the flow is collected by a CCD sensor in image pairs and the in plane velocity is computed for all the nodes of a 2D grid, references on this version of PIV are countless. If two cameras are adopted, pointing to the same planar region, the entire 3D velocity field can be computed on the 2D mesh; an overview on this technique, called stereoscopic PIV (STEREO-PIV), can be found in Prased [10]. Even though the instantaneous, 3D velocity can be measured with STEREO-PIV, the velocity gradient is known only in the investigated 2D region, i.e. the instantaneous, out of plane velocity gradient is unknown. If the velocity field is averaged in time, multiple parallel planes can be scanned with STEREO-PIV in order to obtain a measured volume, this technique provides the entire averaged Reynolds, spin and strain-rate tensor. Unfortunately, in order to obtain the out of plane velocity derivatives with the same resolution of the in plane gradient, one should measure a plane every fraction on millimeter, i.e. perform time costly and storage memory costly experiments.

Instantaneous 3D velocity fields can be measured over a volume using the holographic PIV (HPIV), a well developed technique, see Pu [11], or the tomographic PIV, which is a very new technique, see Elsinga [12].

The main disadvantage of PIV is that the spatial distribution of the static pressure is not measurable. Moreover, people researching in this field are use to say that the facility is designed to host the PIV system rather than being the system applied to the facility. Indeed, large transparent surfaces are needed both for the laser to enter the flow and the camera to focus on the inside of the machine, and this is not always compatible with the applications. For instance, PIV measurements are easily performed over straight and curved channels or linear cascades of blades. A real, 3D turbomachine is difficult to study with PIV because the inner geometry is complex and materials are not transparent; as a result, there are zones that cannot be scanned because of the casting of shadows, or measurements cannot be done very close to solid surfaces because the laser is reflected

back. Therefore a halo is generated, which saturates the CCD sensor in the very same region where the boundary layer is developing.

The latest improvement in the analysis of the flow in turbomachines via PIV is the optical refractive index matched facility. There are liquids, for example a 62%-64% by weight solution of sodium iodide in water, whose refractive index can match the one of solid, transparent materials such as acrylic. Once the matching is obtained carefully adjusting the concentration of the salt, no shadows or changing in the path of light are possible inside the machine and blades, for example, appear in the images just as dark zone without particles. Moreover, the laser sheet passes through the blades reaching every point of the machine and no distortion is induced at the border of the image; blades and casing walls just disappear.

Works by Sinha [13] and Benrha *et al.* [14], for instance, present the results of 2DPIV measurements in pumps providing very useful information about the flow features with simplified impellers and transparent casings. 2DPIV measurements are also performed over an industrial pump with complex geometry - the so-called SHF Impeller, without matching the refractive index of fluid and structures Dupont *et al.* [15], Wuibaut *et al.* [16].

The interaction between the rotor wake and the stator blade in a single stage axial pump is investigated using PIV by Chow *et al.* [17], as the rotor wake is cut by the stator blade a difference in the advection occurs creating discontinuities in the rotor wake trajectory. These wakes are then transported in the diffuser, where they are mixed by the action of vortices and high strain regions.

Aim of the Research

The flow inside the transparent diffuser of a high specific speed centrifugal pump is investigated by means of 2DPIV. Detailed velocity maps on the midspan blade to blade plane allow the flow distribution to be described in one diffuser channel, at different capacities.

The vorticity generated on the impeller blade sides, and transported through the diffuser by the wakes, is measured and phase averaged in order to evaluate the influence of the impeller position on the velocity distribution in the diffuser as well as the influence of reduced flow rates, separations and reversed flows are easily recognized by PIV samples.

Chapter 1

Facility and Data Acquisition System

1.1 Facility

The test loop is described in Fig. 1.1. The tested pump is fitted between two valves, thus it can be isolated from the rest of the loop, details on the machine are given in §1.1.1. The flow passes through a manual valve which is fully opened during the test and closed for maintenance. Then the flow reaches a magnetic induction flow meter, the operator reads the value of the instantaneous flow rate in order to set the desired value. The flowrate can also be read via computer, the information can be combined with pressure signals providing the head and efficiency curves automatically.

The investigated pump is coupled with a large volume, a tank, with a free level. The volume of the tank is more than half the volume of the entire test loop in order to simulate infinite reservoirs both at the suction and at the discharge of the machine. Because the facility is closed and water is contained by metal walls, resonance may occur and lead to destructive effects. The tank lowers the natural frequency of the facility in order to avoid resonance with the pump. Because the water volume is not infinite, a residual loop effect is expected, and the free level is maintained inside the tank to minimize it. The reservoir is connected to a vacuum pump, the compressed air line and a pressure gauge; therefore, the loop pressure can be set positive or negative, relative to the atmosphere. The loop is under vacuum during the injection of seeding through a tap, point F in Fig. 1.1, and during the de-aeration process. Before starting a test, air must be carefully removed from the liquid because bubbles scatter light as particles, but generally they are bigger and they deliver a too intense light signal that affects PIV measurements negatively. After having removed the air, the loop is set under pressure to avoid cavitation at the impeller.

The water pumped in the loop must be filtered periodically because rust is transported by the flow and accumulates in the pipes when the facility is at rest. Moreover, seeding particles can be removed only by filtering the water. In order to obtain the target flow rate, a motorized valve is mounted upstream the pump, therefore the flow rate can be controlled accurately.

1.1.1 Centrifugal Pump

Impeller

The pump investigated is a hybrid machine built fitting a commercial impeller into a transparent diffuser/volute. In order to connect the impeller frame to the volute without leakage flows, a seal drum and a diffuser hub ring are fitted inside the volute, as illustrated in Fig. 1.2. It is worth to describe the convention for the impeller discharge angle, which is an important parameter for this work and there is no universal agreement for that, see

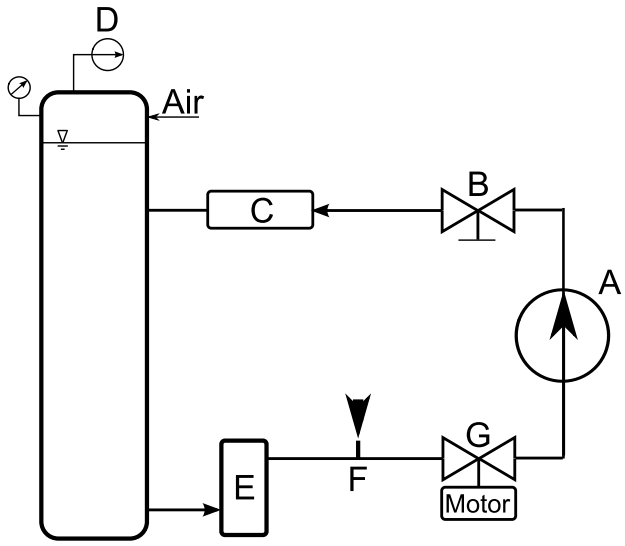

Figure 1.1: **The test loop. A: tested pump. B: manual valve. C: magnetic flowmeter. D: vacuum pump. E: filters. F: seeding insertion point. G: primary valve.**

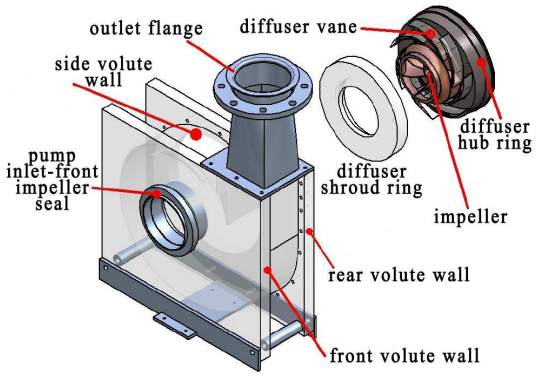

Figure 1.2: **Expanded view of the pump [18]**

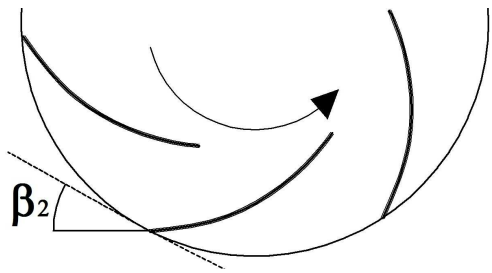

Figure 1.3: **Discharge angle, [18]**

Fig. 1.3. The origin of β_2 is in the tangential direction, i.e $\beta_2 = 90°$ is a perfectly radial flow.

The specific speed of the impeller at best efficiency point (BEP) is computed with (1.1) and shown in Table 1.1, as well as additional data regarding dimensions and the operating condition. Because of the large specific speed, the impeller classification is borderline between centrifugal and mixed-flow; thus the flow at the discharge section can be considered 2D, in the blade to blade plane, but secondary flows - i.e. axial flows - are expected.

$$\omega_s = \frac{\Omega\, Q_{\mathrm{BEP}}^{1/2}}{(\mathrm{g} H_{\mathrm{BEP}})^{3/4}} \tag{1.1}$$

The impeller is made of cast iron and its geometry is largely three dimensional as high specific speed impellers always are. The large blade span at the discharge section and the reduced discharge/inlet diameter ratio are typical of high specific speed machines, and the aerodynamic performance of the blades is an important factor because the centrifugal

Operating condition	
BEP specific speed (ω_s)	1.08
Rotating frequency (Ω [Hz])	8.82
Impeller	
Discharge section diameter (D_2 [mm])	224
Reference radius ($R_2 = D_2/2$ [mm])	112
Inlet diameter (D_1/D_2)	0.688
Discharge blade span (b_2/D_2)	0.089
Discharge blade angle (β_{g2} [°])	29
Discharge rake angle (ς [°])	12
Number of blades	6
Diffuser	
Inlet section diameter (D_3/D_2)	1.040
Discharge section diameter (D_4/D_2)	1.612
Constant vane span (b_3/D_2)	0.088
Inlet vane angle (α_3[°])	18
Number of vanes	7
Vane chord-length (c [mm])	182
Volute	
Constant span / D_2	0.616

Table 1.1: **Pump geometric data**

effect is reduced. Fig. 1.4 illustrates the meridional section of the impeller, passages are wide and the shroud curvature is accentuated, hence the flow is free to distribute spanwisely at reduced capacities.

Table 1.1 indicates the *rake* angle $\varsigma = 12°$, which is the angle that the impeller blade trailing edge forms respect with the axial direction.

When the wake shed from the trailing edge of the impeller blade propagates through a vaneless diffuser and collides with the tongue there is a sudden variation in the momentum that impinges the structure. As the fluid-structure interaction is not steady, vibration and noise are generated. A raked impeller produces a wake that has a spanwise phase mismatch respect to the impeller rotation, and that gradually impinges the tongue, which has always zero rake; therefore the peak of the load on the structure is broad and almost overlaps with the load generated by the following blades, with reduced dynamical effects.

The inlet angle of the flow in the diffuser α_3 is indicated in Table 1.1, with $\alpha_3 = 0°$ along the impeller tangential direction.

Vaned Diffuser and Volute

To ensure optical accessibility, diffuser vanes are made of polymethyl methacrylate (PMMA), commonly known as acrylic, hub and shroud walls are flat plates, and vanes are machined using a numerical control of the shape.

Fig. 1.5 shows part of the diffuser with a close up of the blade, the gap between impeller and diffuser, and the leading edge radius are smaller than in industrial machines to amplify unsteady phenomena related to the blade passage. As wakes reach the leading edge of the diffuser vane, the incidence angle changes suddenly, and a sharp vane is more sensitive to changes in the incoming flow, showing subsequent variations in the separation

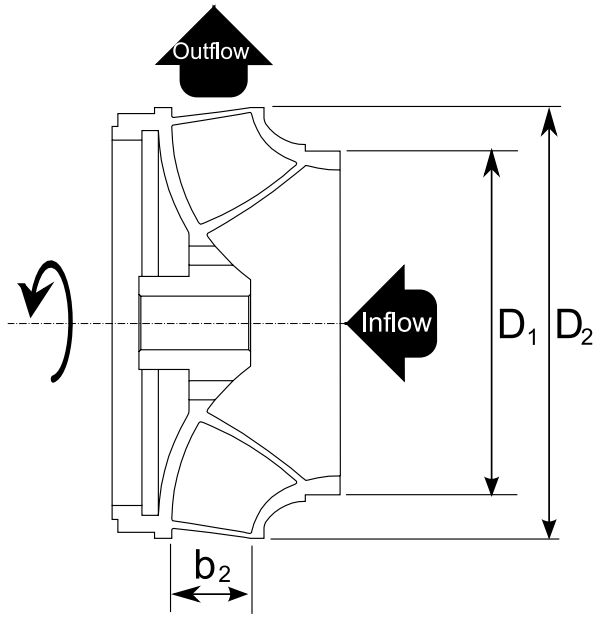

Figure 1.4: **Meridional section of the impeller, [LFM - Politecnico di Milano]**

on the side.

The diffuser vane profile is designed following the classic 2D theory that can be found in Stepanoff [19], the first part of the suction side is a free vortex line, i.e. a log-spiral arc, while the rest of the profile is constructed using circular arcs in order to provide sufficient cross section area for structural strength, and to close the profile at the trailing edge. The span of the diffuser vanes is constant, from the stainless steel hub to the acrylic shroud. The hub hosts seven pressure taps that are located along the centerline of one diffuser channel, only the first and the last are used. Fast response pressure transducers are mounted there in order to achieve pressure spectra at the inflow and discharge sections of the diffuser. Because the diffuser hub can be rotated, different mutual configurations can be tested, with different positions of the diffuser blade respect with the volute tongue, see Fig. 1.6.

The hub and shroud of the volute are made of the same acrylic of the vaned diffuser. The cross section of the volute is rectangular with constant span as described in Table 1.1. The lateral surface is made of poly-carbonate and is designed assuming that the recovering of static pressure is entirely done in the diffuser, thus no additional compression is imposed to the fluid by the volute, which is simply collecting and delivering the fluid. In order to obtain a compact machine, the volute span, in the axial direction, is unusually large. The sudden increasing of the cross section area from the diffuser discharge to the volute inlet creates a pair of strong counter-rotating secondary vortices, those are easily noticeable during the removing of air from the loop as bubbles are entrained by them. The volute is shown in Fig. 1.7, where the horizontal inlet pipe is also visible as well as two of the 120°-spaced pressure taps from which the wall pressure can be measured.

The machine under investigation pumps tap water, hence both laser light and scattered light pass through air, acrylic, and water; this in fact limits the optical performance of the system. Water induces more light dispersion than PMMA and the difference in the refractive index at 532 nm - i.e. the laser wavelength - is 12% of the water index. This

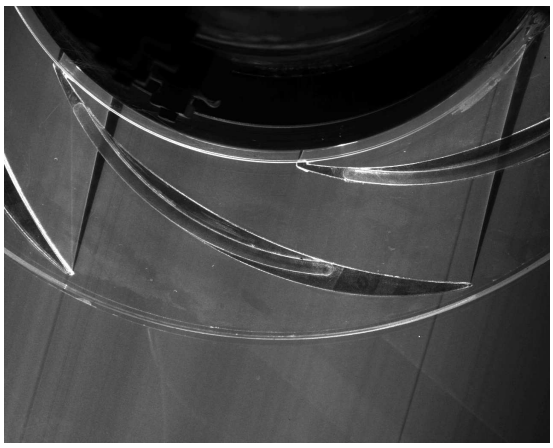

Figure 1.5: **Magnification of a sector of the diffuser, note the leading edge and trailing edge shadows, [LFM - Politecnico di Milano]**

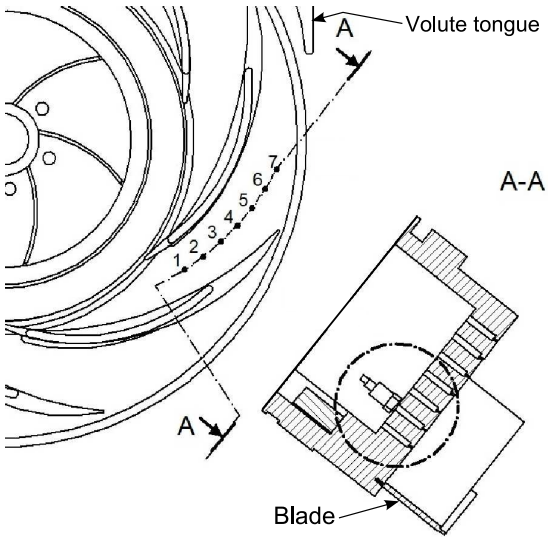

Figure 1.6: **The fast response sensor mounted on the back of the diffuser hub, [LFM - Politecnico di Milano]**

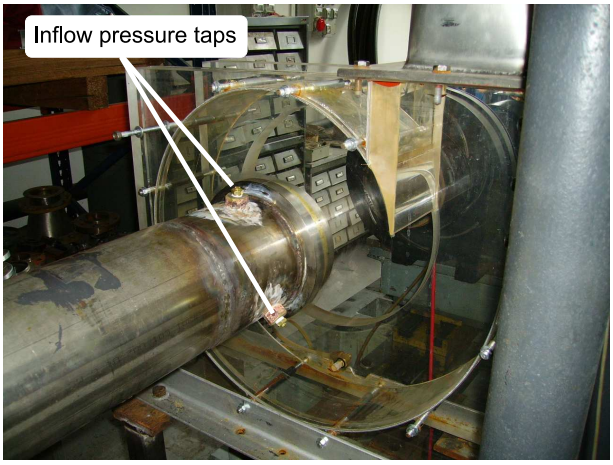

Figure 1.7: **Transparent volute [LFM - Politecnico di Milano]**

difference affects the transmission of the scattered light from the pump to the camera lenses because the light incidence is $\approx 90°$, but only on the optics axis. The large field of the lenses combines with refraction to give a slight deformation at the borders of the image.

As the laser plane enters the diffuser it illuminates high curvature zones - i.e. the leading and trailing edge of the diffuser vane; the light incidence angle changes largely in a very small area, multiple refraction/reflection inside the vane occurs in this situation and light rays are deviated. As a result, leading edges and trailing edges cast shadows over the investigated areas, and particles crossing those areas are invisible, see Fig. 1.5 and Fig. 1.8. The only way to solve this problem is using a medium whose refractive index matches that of the acrylic, unfortunately these liquid solutions are expensive and difficult to manage, while water is cheap and safe.

Supporting Rail, TTL Signal generator and Torquemeter

In order to easily disassemble the pump for cleaning operations without losing the centering of the impeller with the diffuser and volute, the DC motor, the diffuser and the

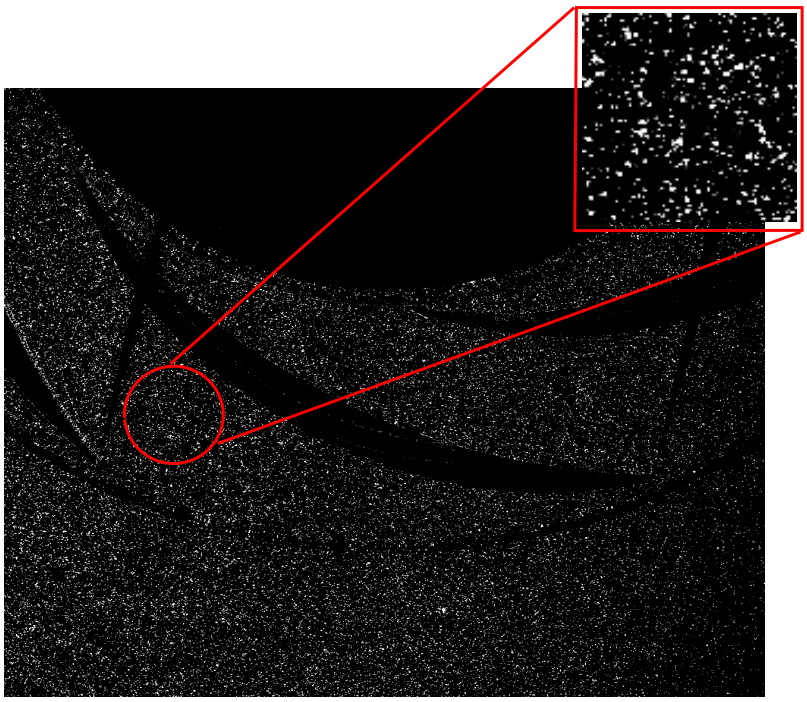

Figure 1.8: **Seeding distribution inside the diffuser, [LFM - Politecnico di Milano]**

impeller are mounted over a rail; the system can slide back from the volute that remains attached to the inlet/discharge pipes; therefore, impeller and sealing drum can be extracted. Maintenance operation are required quite frequently because the impeller rusts easily.

The motor shaft is connected to the pump through a torquemeter, used for measuring the performance curves, see Fig. 2.1. In order to lock the PIV system to the rotor phase, an electro-magnetic TTL signal generator is mounted on the shaft; thus the shaft period is known and the actual rotor phase can be computed. The TTL signal is delivered to the PIV controller where a time delay is set in order to coordinate the laser/camera shots; both the laser double pulse and the camera aperture are synchronized.

1.1.2 Recording and Processing the Images

CCD Camera

The CCD camera adopted for the measurements contains an interline progressive scan CCD sensor cooled by a Peltier stage and then by free convection, the quantization dynamical range can be switched from 8 bit, the range used in this investigation, to 12bit and the sensor is provided with a vertical anti-blooming system. Further information about the sensor can be found in Table 1.2. The camera lens adopted is a macro with adjustable aperture ratio (focal length / diaphragm diameter) and focal length equal to 80 mm.

Laser Device and Optical Bench

In order to produce a laser sheet, a Nd:YAG pulsed laser beam ($\lambda = 532\,\mathrm{nm}$) is irradiated parallel to the machine axis toward a 45° mirror, i.e. it is reflected radially in the diffuser. Immediately after the mirror, a short focal length cylindrical lens converts the beam to a laser plane, see Fig. 1.9. Before starting a measurement session, the beam is pointed toward a target to verify the collimation of the two pulses. If the laser optics are not

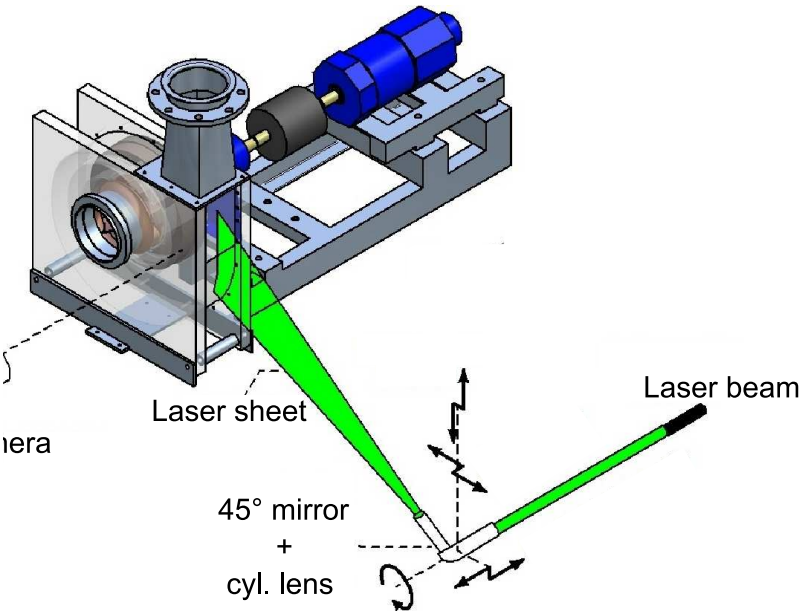

Figure 1.9: **Optical bench converting the laser beam into a laser sheet, [18]**

collimated the laser sheet is doubled and pairs of laser planes do not illuminate the same region, hence this preliminary operation is necessary.

Seeding Particles

The dynamics of a single particle in a fluid stream is a very complex issue, and there is a large amount of particles in the flow; thus, any attempt of modelling the behavior of this multitude of rigid bodies can only be based on statistics, for a exhaustive explanation of the theory see Raffel, [20].

For the present work, 10 µm glass particles have been injected into the loop through a properly designed tap, after having put the loop under moderate vacuum, see Fig. 1.1. Because air must not enter the pipe, a suspension of particles should be prepared in advance and sucked in the facility.

Pixel size [µm]	6.7×6.7
Pixel matrix	1280×1024
Active area [mm]	8.6×6.9
Max. frame-rate [Hz]	4.5
Reading noise [e^-_{RMS}]	$8 \div 13$
Temp. range [°C]	$0 \div 40$
Power [VA]	70

Table 1.2: **Properties of the CCD sensor, [Dantec]**

When the laser illuminates the particles, bright spots are immediately noticeable looking at the PC screen during live recording. The particle luminance per unit of laser energy should be maximized in order to work with low power. Scattered light luminance is a function of the seeding - medium refractive index ratio as well as the particle diameter, shape and orientation. Luminance also depends on the laser polarization. Particles used as PIV tracers scatter light according with the theory by Mie, [20].

Going from theory to practice, it can be stated that:

- particles luminance increases with the square of their diameter,
- large diameter particles scatter light strongly but they are unable to follow the flow properly,
- strong signal from big particles masks smaller particles that may follow the flow better, the distribution of the particles diameter should have as less variance as possible
- very large particles scatter light strongly, and they become a secondary light source for other particles particularly for the out of plane ones, as a result the signal to noise ratio is diminished, this is a serious problem if air bubbles are found in a liquid flow, their emission can be so strong that they can saturate the CCD sensor.

Image Processing

Image processing is a relatively young science that evolved in the past two decades because of the CCD sensors availability at relatively low cost.

PIV images are processed with routines that are usually embedded inside PIV softwares. Image processing can enhance, destroy or corrupt information, i.e. create artifacts, this last is the most dangerous accident. Moreover, images contain more information than human eye can recognize, but a careful analysis of the seeding distribution done by inspection can be very useful.

As an image is indeed a matrix of integers, an algebra can be built over image sets; specifically, in order to eliminate the background from the PIV images it is very useful to compute an image in which only information about the background is present. This can be done easily taking advantage of the fact that sources of information in a PIV image are only particle scattering, background luminance and noise.

Given a set of phase locked images, they share the same background; in order to separate particles from the background it is possible to compute the average image of the set, this image contains the averaged luminance level of the background and particles are substituted by a uniform grey halo due to the fact that in every frame particles have different position.

Subtracting the average from every single original image it is possible to enhance particles erasing the background, see Fig. 1.8; this operation cannot provide perfect results as every image has its own background that is slightly different than in the average because of instantaneous changes in the emission of the laser; nevertheless, removing the average is a large step in the improving of the image quality.

Cross Correlation

Image pairs are sent to a FFT-based cross correlation algorithm (Dantec© Flowmanager®). The interrogation window is 32×32 pixel wide, which is known to optimize the displacement error for a typical 2×2 pixel image particle (Raffel, [20]). The sensor size is 1280×1024 pixels, with an interrogation area of 32×32 pixels and 50% overlap it gives

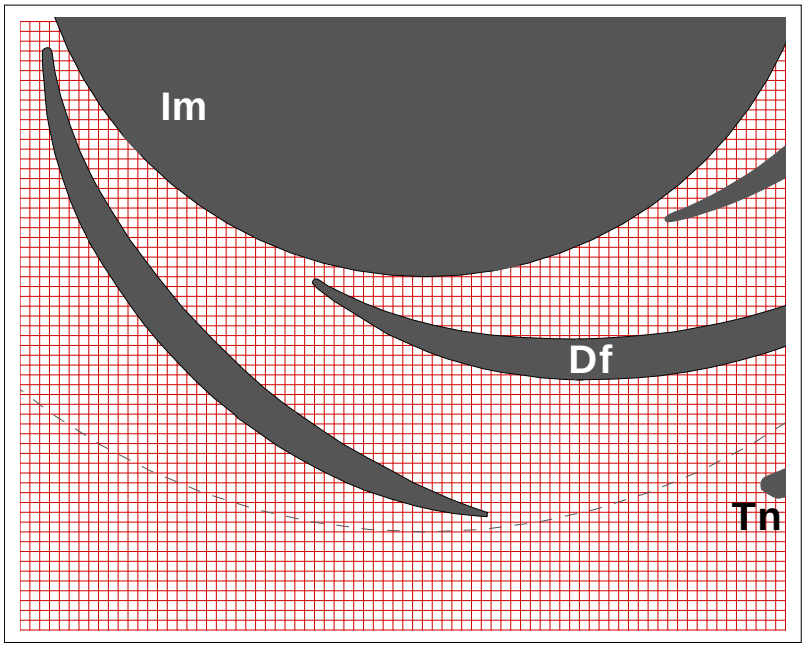

Figure 1.10: **Vector grid and diffuser vanes in the PIV field of view; Im: impeller, Df: diffuser vane, Tn: tongue, [LFM - Politecnico di Milano]**

$(1280/16-1)\times(1024/16-1)=79\times 63$ vectors. The vector spacing is 2.74 mm, equal to $0.0151c$, see Table 1.1, and the scale factor is 171 µm/pixel, see Fig. 1.10.

The time between pulses is not set with the classic N/4 condition, see Raffel [20], because the expected velocity can approach zero in recirculation zones and reach approximately $4\,\mathrm{ms}^{-1}$ in the diffuser throat. The time between pulses is set equal to 50 µs according to previous experiences, to minimize the loss of particles due to out of plane velocity components. It is worth to point out that very low time between pulses lead to large errors due to bias components in the measured displacement, i.e. the peak locking (Raffel, [20]).

The amount of particles in the interrogation window is of great importance for reliable results, the seeding density has been increased step by step until at least 6 particles are noticeable in a 32 pixel window, see Fig. 1.8. In order to further increase the reliability of the results, vectors whose peak ratio is less than 1.2 are rejected; the peak ratio is the ratio between the maximum value of the cross correlation function and the second highest peak value, see Raffel [20] for details.

Chapter 2

Results and Discussion

2.1 Pump Performance Curves

The performance curve of the pump is presented in Fig. 2.1, the reference point is the best efficiency point (BEP) that corresponds to a flow rate of$25 \times 10^{-3}\,\mathrm{m^3s^{-1}}$.

The flow coefficient and the head coefficient are computed with (2.1) and (2.2). The head curve is affected by an increasing data dispersion at the curve plateau and for lower flow rates, this suggests the onset of a large scale instability inside the pump for $\phi/\phi_{\mathrm{BEP}} < 0.6$.

$$\phi = \frac{Q}{\frac{\pi}{4} D_1^2\, U_{\mathrm{tng}}} = \frac{4}{\pi^2}\left(\frac{D_1}{D_2}\right)^2 \frac{Q}{\Omega\, D_2^3} \tag{2.1}$$

$$\psi = \frac{\rho^{-1}\Delta p^{\mathrm{T}}}{\frac{1}{2} U_{\mathrm{tng}}^2} = \left(\frac{2}{\pi^2}\right)\frac{\rho^{-1}\Delta p^{\mathrm{T}}}{\Omega^2\, D_2^2} \approx \left(\frac{2}{\pi^2}\right)\frac{\rho^{-1}\Delta p}{\Omega^2\, D_2^2} \tag{2.2}$$

The approximation in (2.2) is due to the pressure sampling procedure, in fact the pressure has been sampled through taps at the inlet and discharge pipe walls assuming the dynamic pressure to be negligible there respect with the static pressure. The instability around the inflection point of the head curve, and further as the flow rate in decreased, is known to be related to an overlapping of many fluid dynamic phenomena inside the machine. First, as the flow coefficient diminishes, the impeller inlet flow becomes too much tangential overloading the leading edge - i.e. a *pre-swirl vortex* occurs at the inlet section - and a progressive mid-chord to leading edge separation occur. This separation is highly unsteady and affects the diffuser flow cyclically because of the impeller rotation, this leads to noise and vibrations, because the separated wake is turbulent, and the effect is known as *Jet & Wake*. Secondly, if the flow rate is low, the impeller channel cannot be entirely filled with fluid, this is known as the *impeller stall* phenomenon, often resulting in back/recirculating flows start inside the gap between the shroud and the casing wall.

The pump BEP specific speed is equal to 0.872 and it is computed with (2.3), this machine can be classified as borderline between centrifugal and mixed-flow, indeed the transition between centrifugal and mixed flow is not sharp.

$$\Omega_{\mathrm{s}} = \frac{\Omega\, Q_{\mathrm{BEP}}^{1/2}}{(gH_{\mathrm{BEP}})^{3/4}} \tag{2.3}$$

High specific speed impellers are characterized by $D_1/D_2 \approx 1$; moreover, the gap between the shroud and the internal surface of the casing has very limited radial extension and recirculating flows occur easily in the gap between the volute and the impeller shroud.

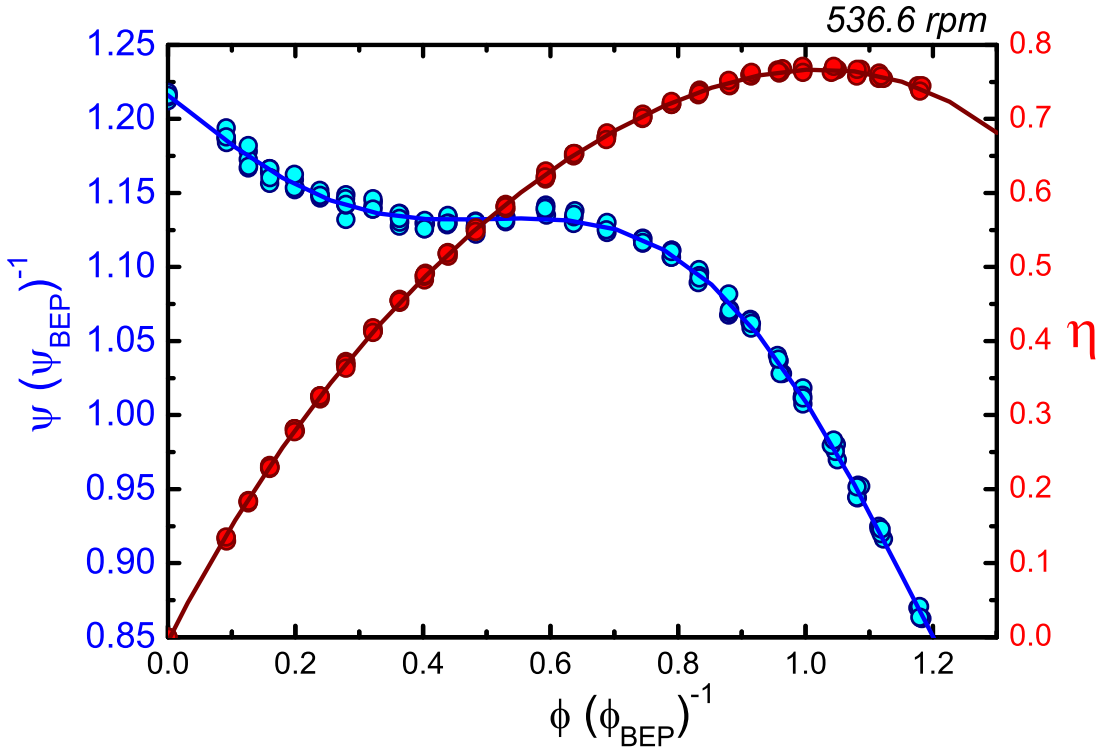

Figure 2.1: **Head coefficient and efficiency of the pump**

2.2 Frequency Domain Analysis

In order to evaluate the instability introduced in §2.1, a series of static pressure samplings are processed and presented in the frequency domain.

First, a standard power spectrum density analysis is performed over two static pressure signals sampled at the hub wall inside the diffuser with fast response pressure transducers, as shown in Fig. 1.6, §1.1.1. The static pressure power spectrum density is illustrated in Fig. 2.2 and Fig. 2.3 where the pressure fluctuation is measured in Pa, and the abscissa is the dimensionless ratio f/Ω - it can be also called a Strouhal number - thus the impeller blade normalized frequency is equal to the number of blades.

Two peaks are clearly visible in the spectrum. The first ($f/\Omega = 1$) marks the impeller round periodicity and it is due to a lack of impeller symmetry; in fact, the impeller is made of cast iron and the manufacturing process cannot provide neither symmetry in the vanes position nor a perfect shaft - impeller centering. The second peak is related to the impeller blade passage; as these two events are very deterministic - i.e. very localized in frequency - their peaks are very narrow[1]. Both peaks are more intense in the diffuser rather than at the impeller inlet section because they are really linked to the impeller discharge flow and the diffuser pressure tap is located very close to the impeller outlet section.

On the other hand, the sub-round behavior of the pump is very complex and the instability is noticeable inside a broad band from a reduced frequency slightly higher than unity to $f/\Omega \approx 0.2$ i.e. five times the impeller round period. Moreover, as the PSD is

[1]Fig. 2.2 presents it doubled because the actual blade passage frequency is equal to 52.9Hz and it is very close to the power supply electrical disturbance (50Hz) that affected the inlet section pressure transducer

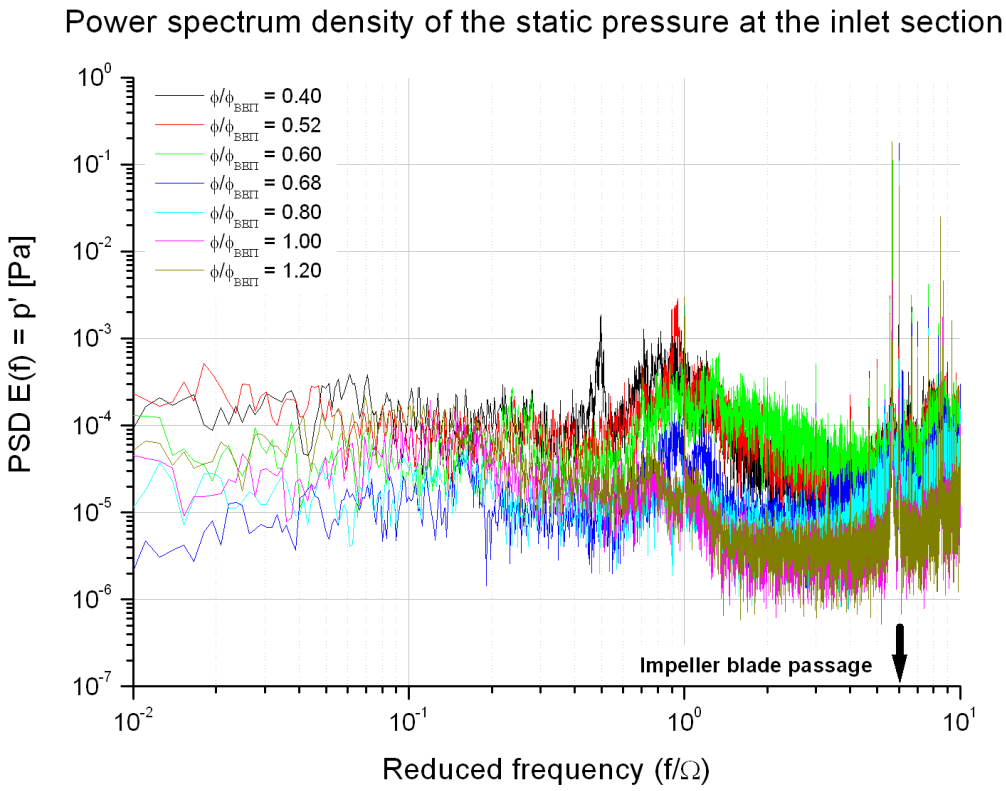

Figure 2.2: **PSD of the static pressure at the impeller inlet section**

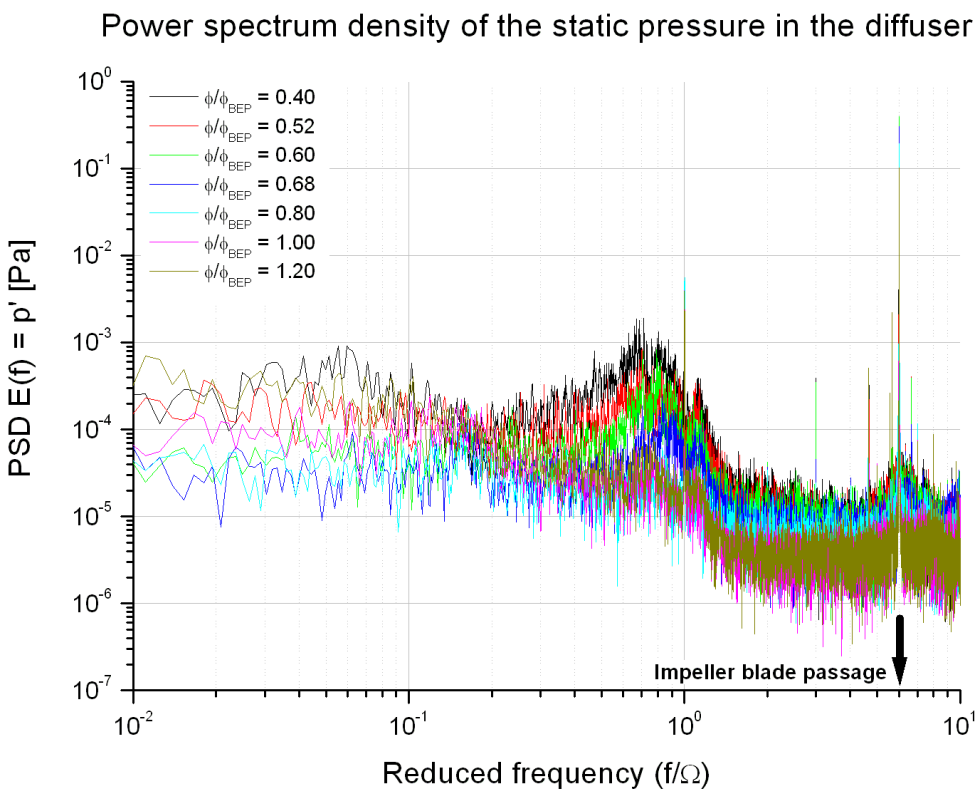

Figure 2.3: **PSD of the static pressure in the diffuser**

computed for a broad range of flow rates, Fig. 2.3 allows the increased noise level at low flow rates to be noticed. Starting from $\phi/\phi_{\mathrm{BEP}} = 0.60$ there is a sudden increase in low frequency harmonics, that continue increasing monotonically until $\phi/\phi_{\mathrm{BEP}} = 0.40$, which is the lowest flow rate tested.

Comparing Fig. 2.2 with Fig. 2.3 it is possible to state that at high flow rates ($0.80 \leq \phi/\phi_{\mathrm{BEP}} \leq 1.20$) the diffuser does not affect the pressure signal largely, except for $f/\Omega \geq 6$ where it behaves as a low-pass filter; thus, for these high flow rates the flow inside the diffuser is well guided and the impeller is not inducing substantial unsteadiness. These results are in good agreement with the flow structure measured in the diffuser at high flow rates and discussed in §2.3.2 where the incidence at the diffuser leading edge is correct and the flow is attached to the vanes.

Approaching the impeller round frequency, the signal amplitude increases with a peak distribution that is symmetric around a smooth peak frequency. This distribution is centered at the impeller frequency at the inlet section and it is shifted to lower frequencies inside the diffuser, in the interval $6 \leq f/\Omega \leq 7$, i.e. in the typical rotating stall frequency of a diffuser. This behavior is related to the broad passages in the impeller, because of the high specific speed, that do not impose constraints over the flow - i.e. vortical and secondary flows occur. The broad peak distribution makes the diffuser stall impossible to be captured by 2DPIV because a strict phase locked phenomenon is needed, and this fluctuation is not enough deterministic to be resolved with a phase locked approach.

At lower flow rates ($\phi/\phi_{\mathrm{BEP}} \leq 0.60$) the pressure signal at the impeller inlet section is more noisy in the $[1, 6]$ reduced frequency band; this behavior suggests that unsteadiness at the impeller entry section - for $\phi/\phi_{\mathrm{BEP}} = 0.60$ - is particularly broad band and it is damped inside the impeller as it is not visible inside the diffuser. Instabilities around $f/\Omega = 1$ globally affect the machine ; for $\phi/\phi_{\mathrm{BEP}} = 0.40$ and $0.4 \leq f/\Omega \leq 0.5$ an inlet pressure peak is clearly noticeable suggesting the presence of a flow structure that rotates with a period that is between two and three times the impeller round and is the product of the complex interactions between a strong pre-swirl vortex and a massive suction recirculation.

The main results obtained by the pressure PSD analysis is the proof that at every flow rate the flow is dominated by the impeller blade passage that is also a very deterministic event; because the 2DPIV investigation is largely focused on the effect of the cyclic unsteadiness induced by the blade passage, the rotor phase average approach is justified.

2.3 Steady State Analysis of 2DPIV Results

The PIV cross correlation routine provides a displacement vector field; by knowing the time between the two pulses - 50 µs - it is possible to generate an instantaneous velocity field. In fact, the time between two pulses in a pair is negligible compared with the time between consecutive pairs. The velocity vector is then computed as the ratio between the displacement and the time between pulses. A set of instantaneous 2DPIV vector fields is a massive amount of data, drawing conclusions about the flow without reducing it is almost impossible, and averaging is a very good way to reduce data. Moreover, averaged 2DPIV data have sufficient spatial resolution for computing gradients in space and various functions of these gradients; this is very useful in the study of local vorticity, strain-rate and turbulence, on the other hand it enlarges the amount of data that can be shown. Moreover, because turbomachines rotor can rotate $\sim 10^2$ or $\sim 10^3$ times every minute for $\sim 10^3$ hours every year, a single, instantaneous, flow feature inside the stage has little importance. In order to affect the flow appreciably, a phenomenon must be continuous, periodic or broad-band turbulent; hence, persistent in time. Very few transient phenomena

can really destabilize a machine, and they must very powerful, i.e. the water hammer, which surely is not induced by small scale perturbations. In order to reduce the data while keeping useful information, one should consider the flow in terms of harmonics, or time scales, and the processing of the data always involves spatial or temporal filtering.

The performance curve of the pump can be though as an extremely low-pass filtered result, being it a steady state result, or zero frequency. The equivalent PIV measurement is the total average of all the PIV measurements performed on the same blade to blade plane

$$\mathbf{U}(\mathbf{x}) = \frac{1}{N}\sum_{n=1}^{N}\mathbf{u}(\mathbf{x}) \tag{2.4}$$

where N is the total number of measurements, $\mathbf{u}(\mathbf{x})$ is the instantaneous distribution of the velocity in the investigated region and $\mathbf{U}(\mathbf{x})$ is the distribution of the averaged velocity. The velocity can be interpolated and integrated along a line to give the flow rate (per unit of span-wise coordinate) at the inlet or outlet section of the diffuser channel. Vorticity is a scalar value for planar velocity data and, because its computations involves spatial derivatives of the velocity while the average is a time filtering, the two commute and the averaged vorticity coincides with the vorticity of the averaged vector field. The out of plane vorticity is computed as indicated in (2.5), i.e. substituting the spatial derivatives with central differences except at boundary nodes in which forward or backward differences are adopted.

$$\omega_z = \frac{V(i+1,j) - V(i-1,j)}{x(i+1,j) - x(i-1,j)} - \frac{U(i,j+1) - U(i,j-1)}{y(i,j+1) - y(j,i-1)} \tag{2.5}$$

2.3.1 Best Efficiency Point

Fig. 2.4 shows the phase averaged velocity distribution in the diffuser at mid-span, in the tongue region. Impeller and diffuser blades are masked, and zones corrupted by reflections or shadows in the images are set to white. The presented velocity map is the average of 12 phases equally distributed in one impeller pitch (60°). Every phase-averaged field is computed with 200 instantaneous maps, thus the total average flow is derived from 2400 instantaneous frames. The velocity is normalized with the impeller peripheral velocity $[||U,V||U_{\mathrm{tng}}^{-1}]$.

The distortion of the flow due to the presence on the diffuser is evident. Iso-velocity contours are not concentric with the impeller and the flow slows down less at the suction side. A separation of the flow at the convex side beyond 50% of the chord is noticeable, with a region of stagnation / recirculation, more intense close to the tongue, the separation is likely due to the incorrect inlet angle of the diffuser, that is better adapted to the impeller discharge flow at higher flow rates.

The flow discharged by the diffuser impinges the tongue with positive incidence, i.e. the flow is more radially-oriented than the tongue leading edge centerline, as illustrated in Fig. 2.6 by the stagnation region at point $(0.84, -1.52)$. Hence, increased influence of the tongue on the performance is expected, as well increased exchange of forces.

The flow enters the diffuser along the concave side, which is designed as a free vortex surface, and it is deviated radially outward because of the blade blockage.

The separation at the convex side is also evident in Fig. 2.7, where the pressure side boundary layer vorticity detaches and is convected in the volute; vorticity is normalized with the impeller vorticity, i.e. twice the angular velocity $[\omega_z(2\Omega)^{-1}]$. The low velocity zone in the rear part of the vane contains vortical structures without preferential shape or spin, the average vorticity is nearly zero. Fig. 2.7 also evidences the vorticity generated

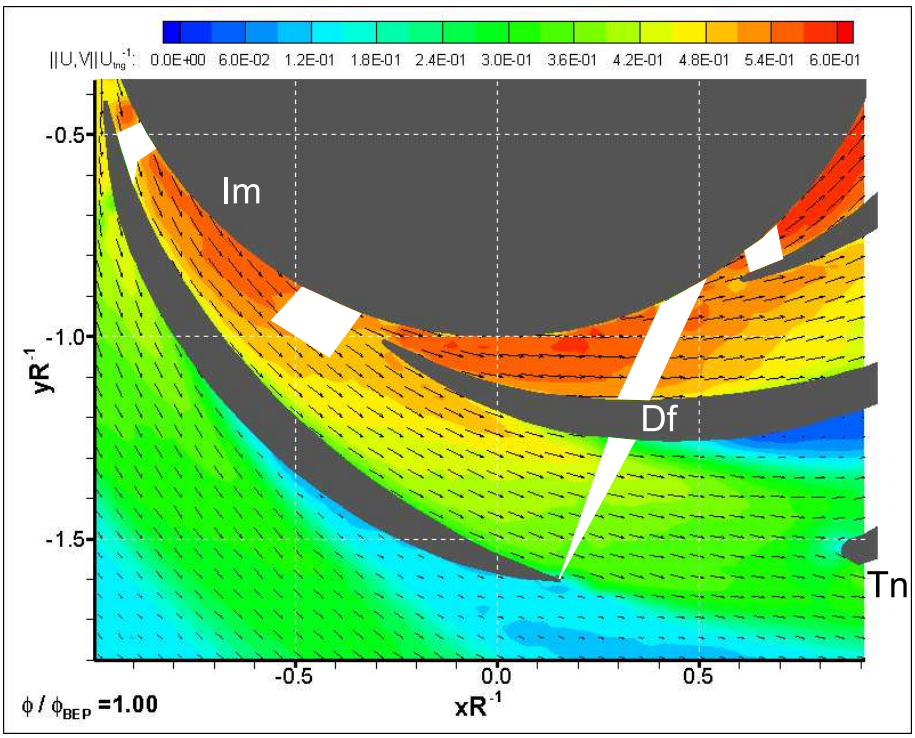

Figure 2.4: **Velocity distribution in the tongue region of the diffuser, $\phi/\phi_{\mathrm{BEP}} = 1.0$, 50% span, vectors are diluted (1:2) horizontally and vertically for clarity, white zones cover corrupted data; the velocity is normalized with the impeller peripheral speed; Im: impeller, Df: diffuser, Tn: tongue**

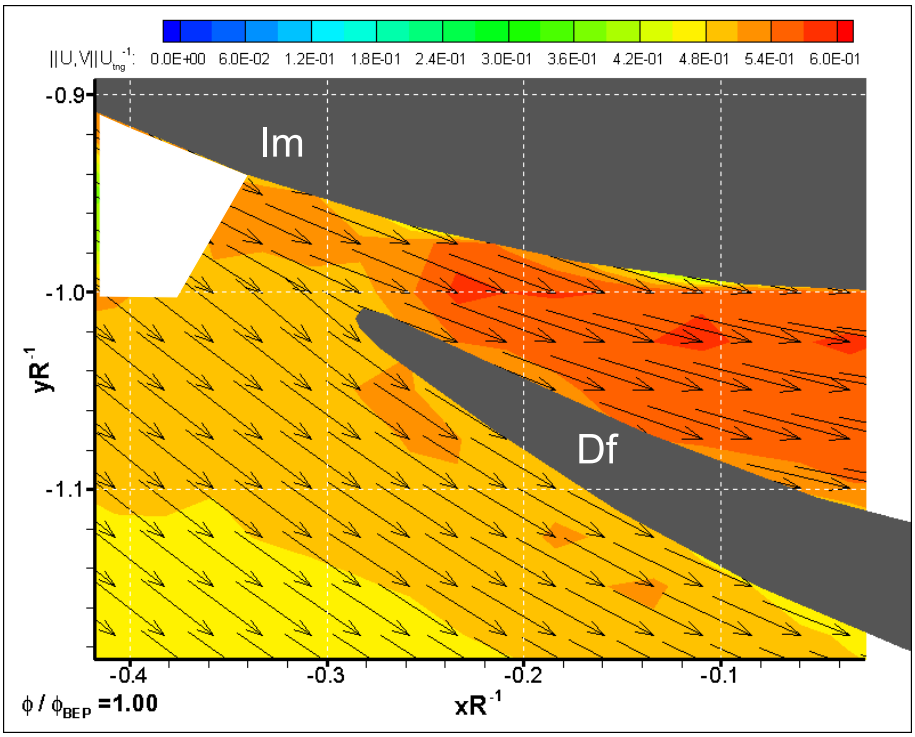

Figure 2.5: **Magnification of the velocity distribution at the diffuser leading edge, $\phi/\phi_{\mathrm{BEP}} = 1.0$, 50% span; ; Im: impeller, Df: diffuser**

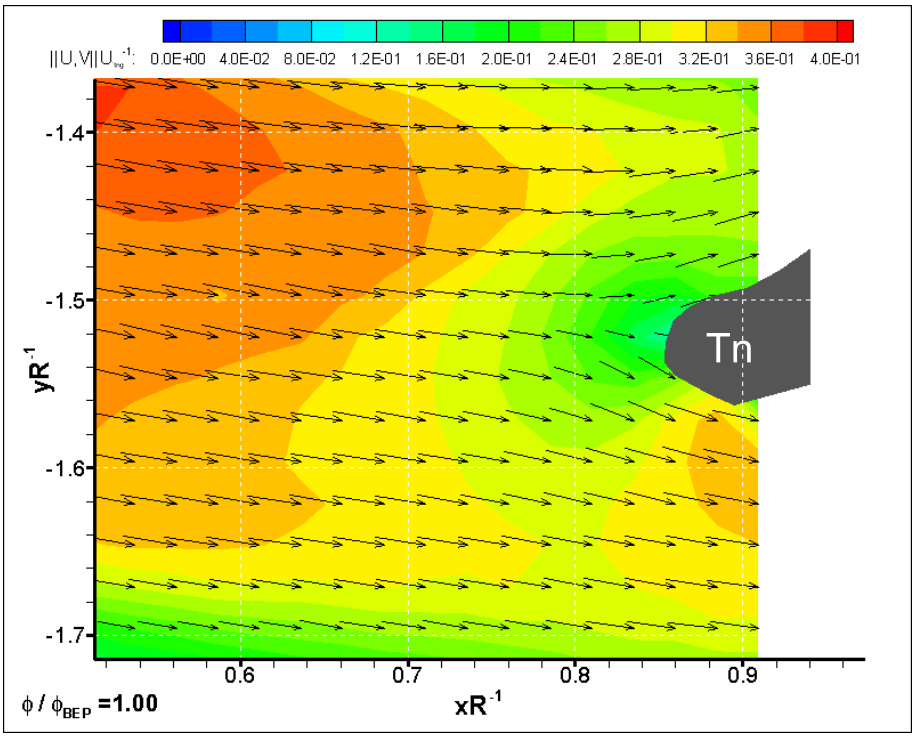

Figure 2.6: **Magnification of the velocity distribution around the tongue, $\phi/\phi_{\mathrm{BEP}} = 1.0$, 50% span; Tn: tongue**

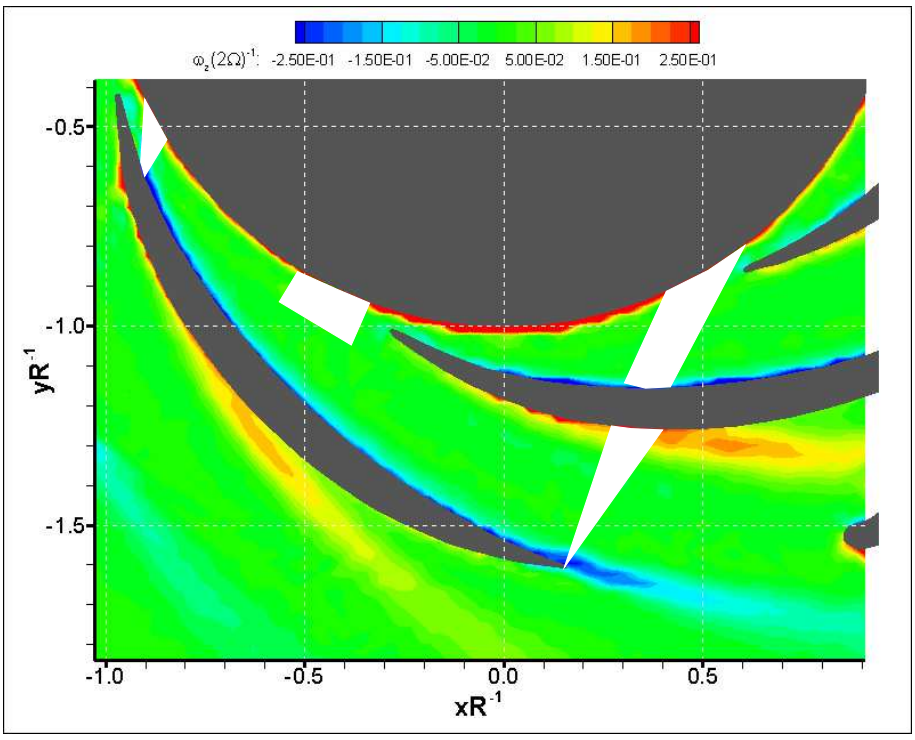

Figure 2.7: **Axial vorticity distribution in the tongue region of the diffuser, $\phi/\phi_{\mathrm{BEP}} = 1.0$, 50% span; the vorticity is normalized with the impeller vorticity 2Ω; Im: impeller, Df: diffuser, Tn: tongue**

on the perimeter of the impeller by the non-slip condition over the trailing edge of the impeller blade.

The boundary layer located on the convex side just beyond the leading edge of the diffuser vane is remains attached, the flow there is accelerated by the throat effect of the diffuser; because the blade has a certain thickness, the convex side at the diffuser inlet section generates a short convergent channel. Fig. 2.4 also show that the velocity is large close to the leading edge at the convex side.

2.3.2 120% BEP Flow Rate

Head / efficiency curves illustrated in Fig. 2.1 show a steep decay of the head coefficient from 100% BEP to 120% BEP flowrate with 5% efficiency loss. The increased flow coefficient induces more radial impeller outflow, and diffuser inflow; a mismatch between the mean inflow velocity and the centerline of the diffuser profile at the leading edge is expected, with positive incidence on the diffuser vanes.

The positive incidence angle causes the leading edge stagnation point to move on the suction side of the diffuser vane, thus the leading edge induces higher blockage than at 100%BEP as noticeable in Fig. 2.8 and better in Fig. 2.9; after this stagnation region the flow fills the passage and slows down gradually until the vane trailing edge is reached, the deceleration of the flow is large there.

Likely the most important result is noticeable along the first fraction of the vane profile; at BEP flow rate the velocity is higher at the suction side, see Fig. 2.4 as expected for nearly zero incidence incoming flow, but at high flow rate the trend is the opposite, i.e. the velocity is higher at the convex side because the incoming flow is too much radial and the incidence on the vane is positive, as illustrated in Fig. 2.9.

At BEP flow rate, the diffuser recovers static pressure by forcing the mean flow streamlines to be more radial than the free vortex spiral, but that happens downstream of the leading edge, which is designed to be neutral. Conversely, at high flow rate the vane is entirely loaded - from the leading edge - with positive incidence, the concave side becomes the pressure side and the vane is subjected to a lift that is likely directed radially outward.

The negative incidence also changes the wake downstream the vanes, comparing Fig. 2.8 and Fig. 2.4 it can be seen that at 100% BEP flow rate the velocity magnitude in the wake is $\sim 0.1\,\mathrm{ms}^{-1}$ and a mean flow convection is noticeable; on the other hand, at 120% BEP, the vane blocks the flow and the momentum in the wake is very low. The wake is not wider, but the induced velocity gradient is much larger than at 100% BEP.

Increased velocity in the diffuser induces larger velocity gradients and larger vorticity levels; Fig. 2.11 shows that the convex side, positive vorticity generated along the blade detaches from the vane as the separated wake forms, and develops downstream in the vorticity shear layer.

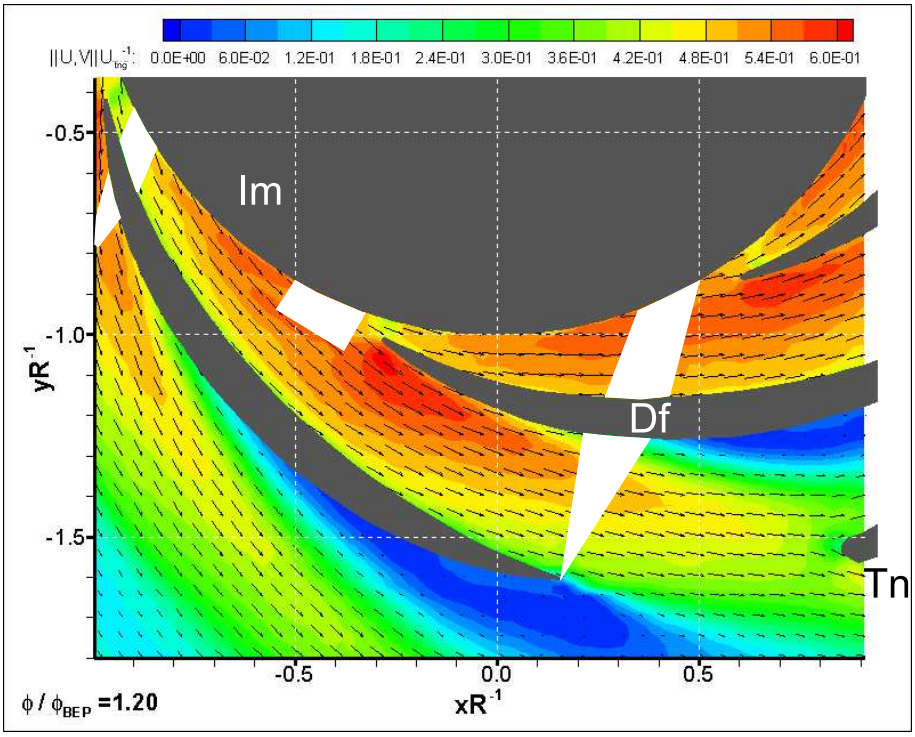

Figure 2.8: **Velocity distribution in the tongue region of the diffuser, $\phi/\phi_{\mathrm{BEP}} = 1.2$, 50% span, vectors are diluted (1:2) horizontally and vertically for clarity. The velocity is normalized with the impeller peripheral speed; the velocity is normalized with the impeller peripheral speed; Im: impeller, Df: diffuser, Tn: tongue**

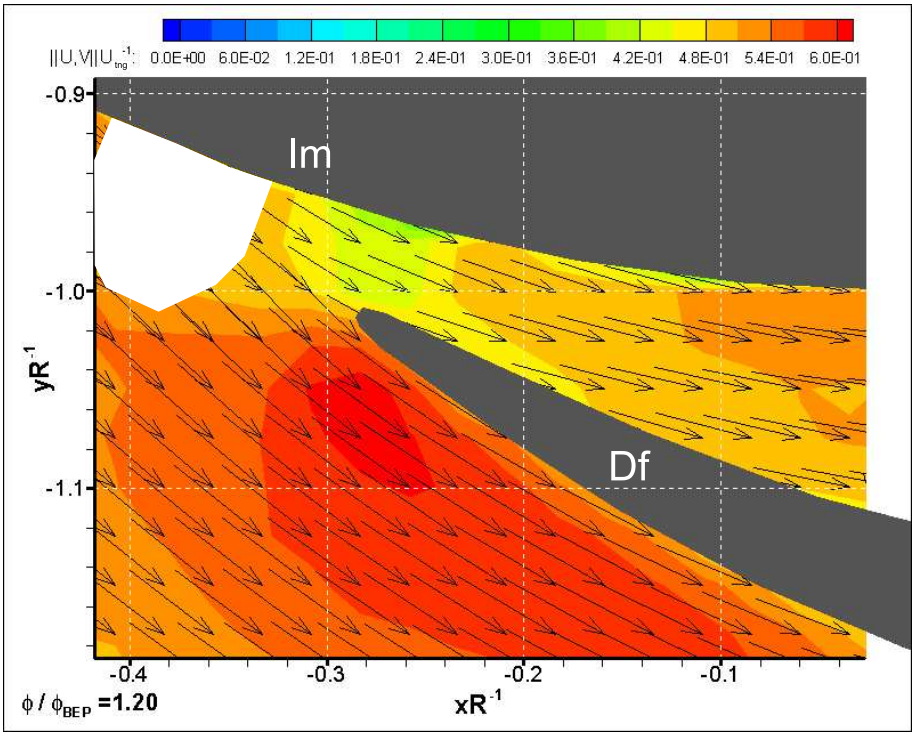

Figure 2.9: **Magnification of the velocity distribution at the diffuser leading edge, $\phi/\phi_{\mathrm{BEP}} = 1.2$, 50% span; Im: impeller, Df: diffuser**

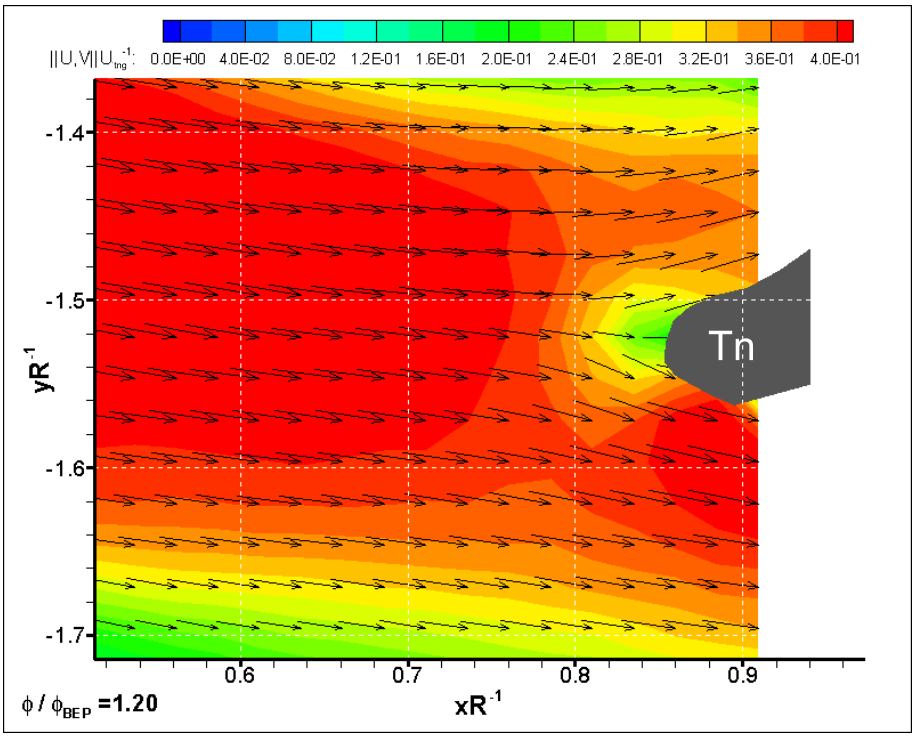

Figure 2.10: **Velocity magnitude distribution around the tongue, $\phi/\phi_{\mathrm{BEP}} = 1.2$, 50% span; Tn: tongue**

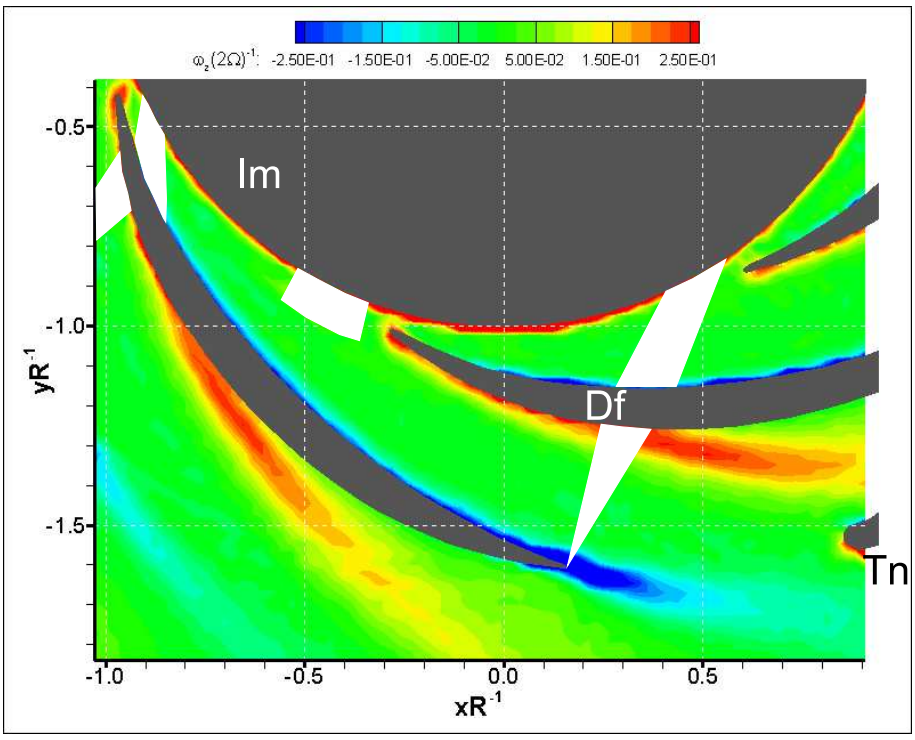

Figure 2.11: **Axial vorticity distribution in the tongue region of the diffuser, $\phi/\phi_{\mathrm{BEP}} = 1.2$, 50% span; the vorticity is normalized with the impeller vorticity 2Ω; Im: impeller, Df: diffuser, Tn: tongue**

2.3.3 80% BEP Flow Rate

When the pump operates at reduced flow rate, the diffuser inlet velocity becomes more tangential than in the BEP case, and the incidence angle on the vanes is negative[2]. The negative incidence enforces the suction effect at the concave side with an accentuated velocity difference between the two sides of the vane.

Fig. 2.12 shows the mean velocity at mid-span, 20% flow rate drop is sufficient for inducing visible changes in the flow. The separation of the flow at the convex side of the vane is accentuated and starts early at approximately 25% of the chord leaving a zone of very low mean velocity behind.

Moreover, the flow slows down abruptly at the vane inlet, losing 50% of the in plane momentum. A comparison between Fig. 2.5 and Fig. 2.13 shows that the flow enters the diffuser tangentially but the geometry is still able to control the angle mismatch even though the leading edge is very thin.

Fig. 2.6 and Fig. 2.14 show that the flow impinging the tongue is divided in two, one half enters the volute and the rest recirculates through the volute starting section at 120% and 100% BEP, but at 80% BEP the flow is entirely discharged in the volute.

At low flow rate, the channel between vanes is filled with positive vorticity generated at the convex side by the separated flow while the vorticity generated at the concave side remains attached to the profile until the trailing edge is reached.

Negative incidence generates localized negative vorticity at the leading edge on the concave side of the diffuser vane likely due to leading edge separation and reattachment. Positive vorticity located at the impeller discharge section is due to the no-slip condition at the impeller trailing edge surface; in fact, the impeller spin is positive and the global average of measurements distributes the impeller near wake along the discharge section. Positive vorticity is convected towards the tongue, and also generated locally there.

[2] here the incidence is defined as the difference between the incoming flow angle and the *geometric* inlet angle of the diffuser vane, i.e. the angle of an attached flow, which does not change with the flow rate

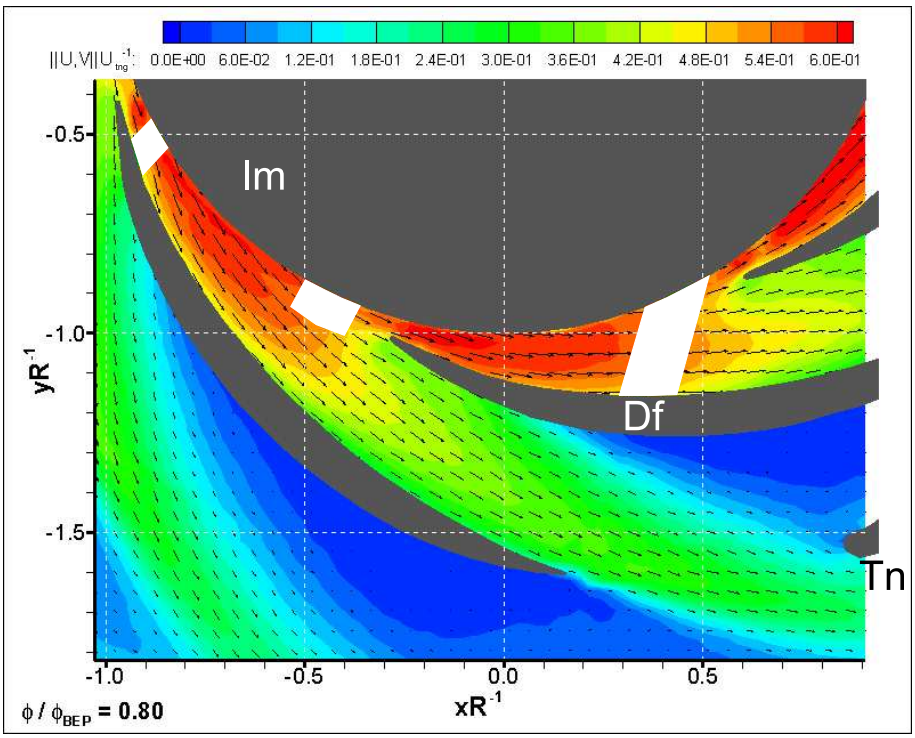

Figure 2.12: **Velocity distribution in the tongue region of the diffuser, $\phi/\phi_{\mathrm{BEP}} = 0.8$, 50% span, vectors are diluted (1:2) horizontally and vertically for clarity. The velocity is normalized with the impeller peripheral speed; Im: impeller, Df: diffuser, Tn: tongue**

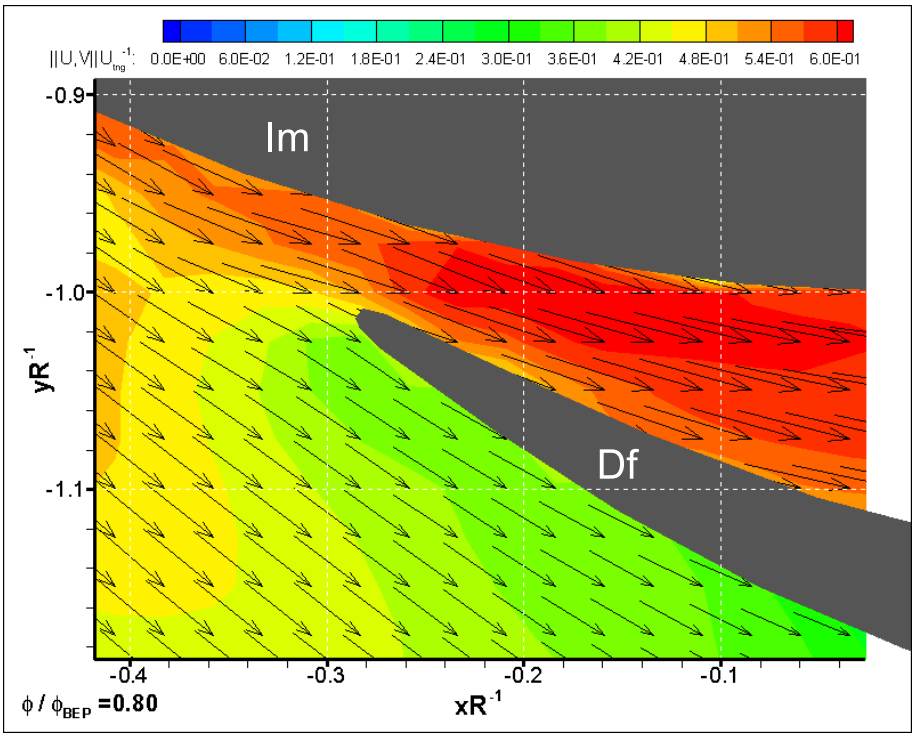

Figure 2.13: **Magnification of the velocity distribution at the diffuser leading edge, $\phi/\phi_{\mathrm{BEP}} = 0.8$, 50% span; Im: impeller, Df: diffuser**

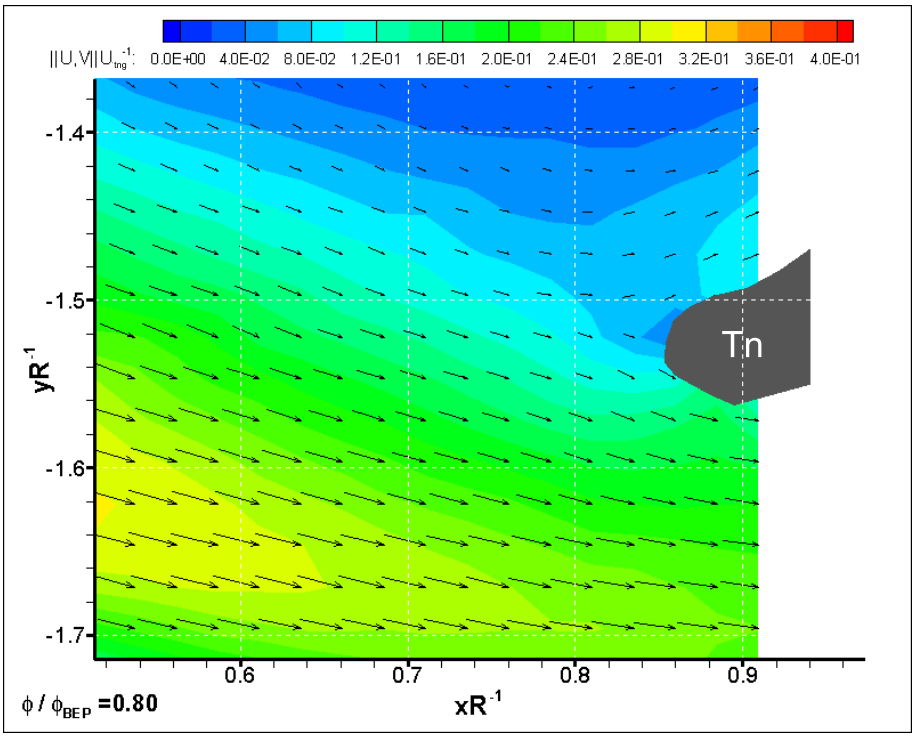

Figure 2.14: **Velocity magnitude distribution around the tongue, $\phi/\phi_{\mathrm{BEP}} = 0.8$, 50% span; Tn: tongue**

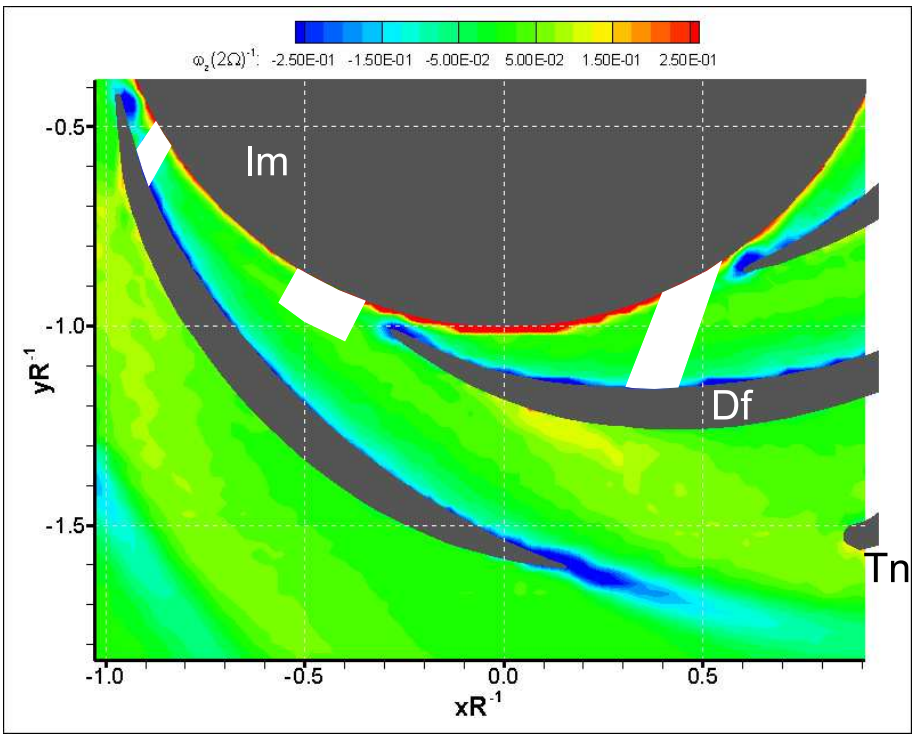

Figure 2.15: **Axial vorticity distribution in the tongue region of the diffuser, $\phi/\phi_{\mathrm{BEP}} = 0.8$, 50% span, the vorticity is normalized with the impeller vorticity 2Ω; Im: impeller, Df: diffuser, Tn: tongue**

2.3.4 40% BEP Flow Rate

At very low flow rates, out of plane (axial) velocity components appear. The velocity drops to 10% of the impeller speed just at the diffuser channel entrance and there is a large separation at the convex side of the diffuser vane.

Downstream, close to the trailing edge, the velocity increases to 18% of the impeller speed as noticeable at points $(0.2, -1.5)$ and $(-1.0, -1.2)$ in Fig. 2.16; this is due to out of plane motion thus, at very low capacities, axial flow components in the diffuser are noticeable.

Fig. 2.17 clearly shows that the flow leaving the impeller is very tangential and hits the diffuser vane with negative incidence, the leading edge induces large blockage effect. Beyond the leading edge, the fluid proceeds along the convex side with very low velocity, and turns around the edge entering the next channel with a reverse radial component, i.e. the radial component of the velocity points back towards the impeller.

Comparing all the velocity fields at the tongue region, it is clear that at very low flow-rates the discharged flow returns to impinge the tongue with nearly zero incidence, but very low velocity; moreover, the stagnation point on the tongue is noticeable.

Fig. 2.19 shows the mean flow vorticity, the diffuser inlet velocity is very tangential and a separation occurs on the leading edge, the separated flow is then convected towards the channel but vorticity decays to almost zero at the entry section of the channel. The convex side separation is not evident.

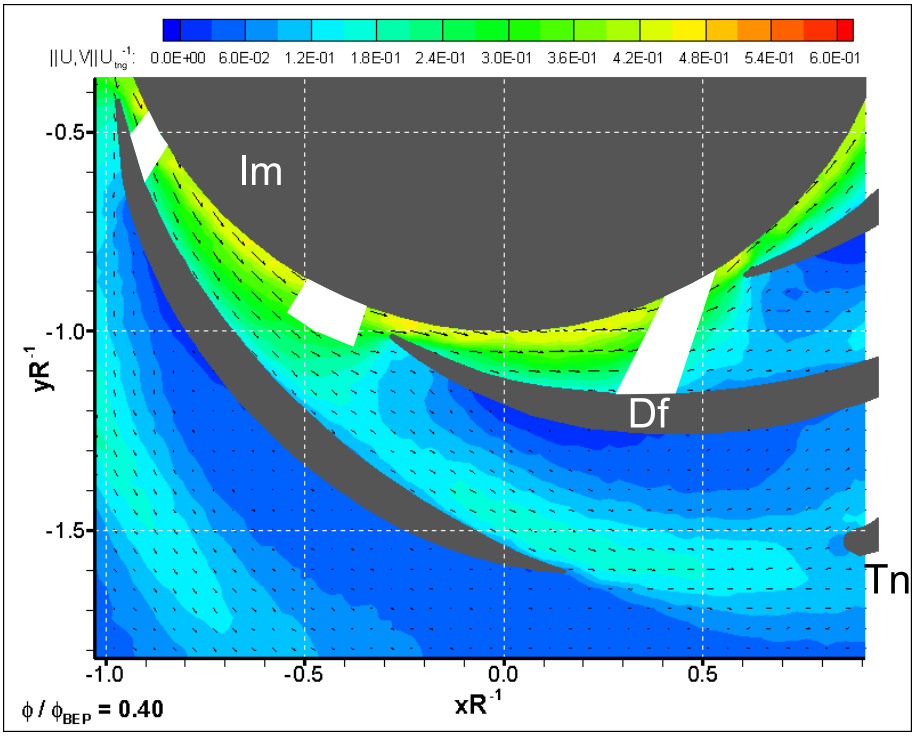

Figure 2.16: **Velocity distribution in the tongue region of the diffuser, $\phi/\phi_{\mathrm{BEP}} = 0.4$, 50% span, vectors are diluted (1:2) horizontally and vertically for clarity; Im: impeller, Df: diffuser, Tn: tongue**

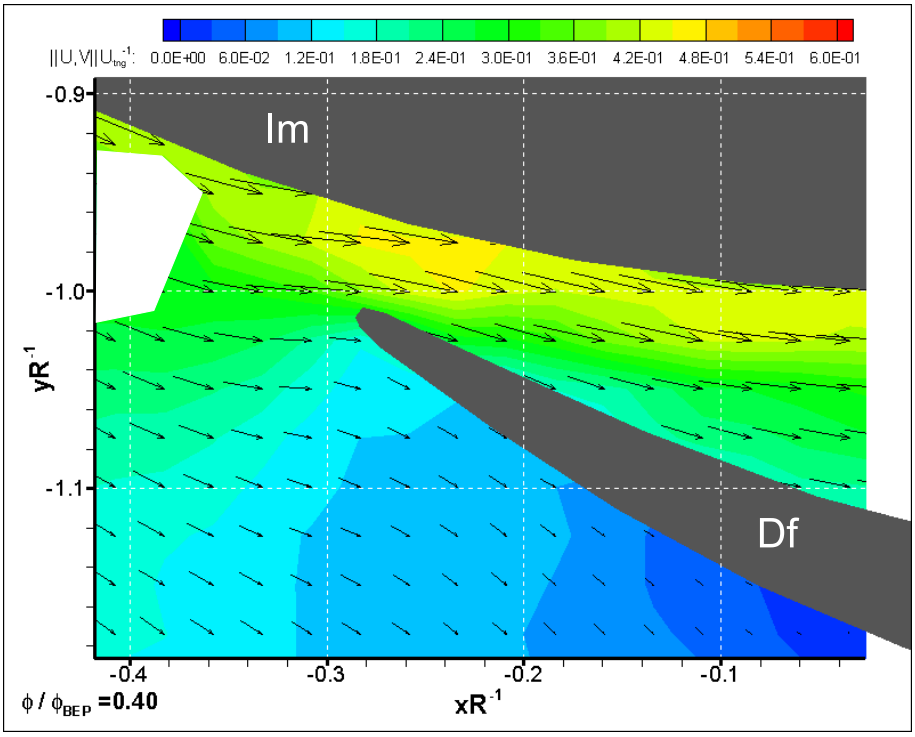

Figure 2.17: **Magnification of the velocity distribution at the diffuser leading edge, $\phi/\phi_{\mathrm{BEP}} = 0.4$, 50% span; Im: impeller, Df: diffuser**

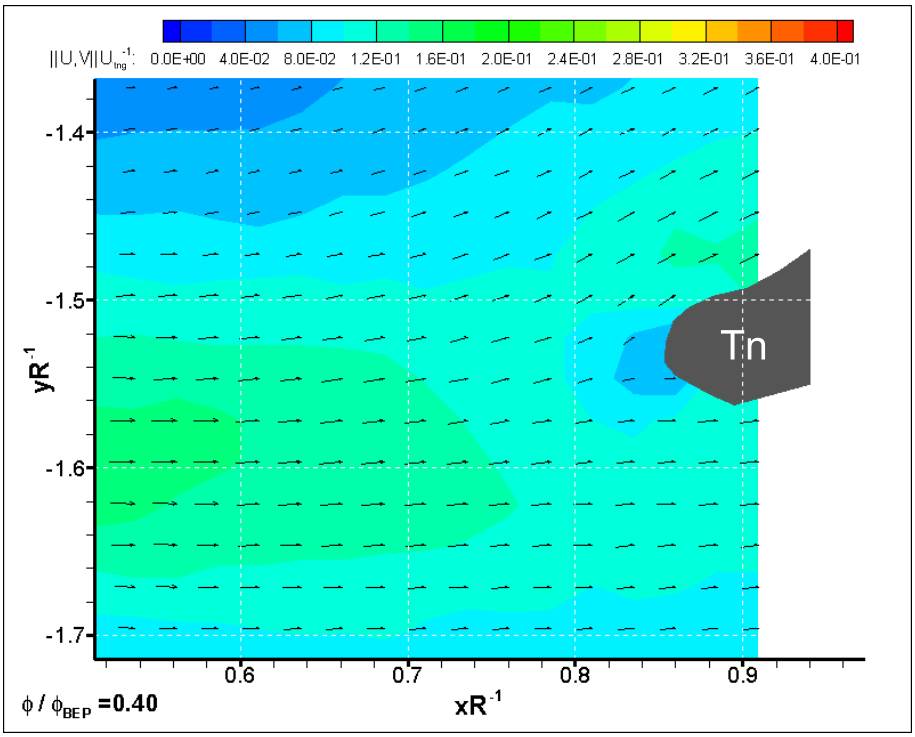

Figure 2.18: **Velocity magnitude distribution around the tongue, $\phi/\phi_{\mathrm{BEP}} = 0.4$, 50% span; Tn: tongue**

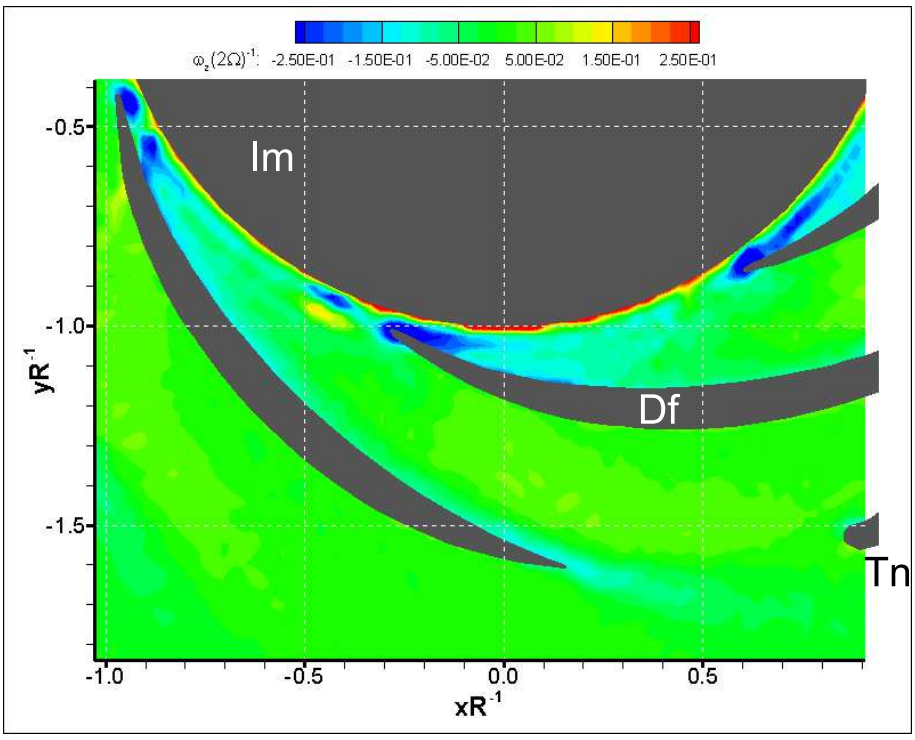

Figure 2.19: **Axial vorticity distribution in the tongue region of the diffuser, $\phi/\phi_{\mathrm{BEP}} = 0.4$, 50% span; the vorticity is normalized with the impeller vorticity 2Ω; Im: impeller, Df: diffuser, Tn: tongue**

2.4 Phase Averaged Analysis

Transport phenomena dominate the propagation of jets and wakes from the discharge section of the impeller through the vaned diffuser, and in the volute. An inflow boundary condition exists at the entry section of the diffuser and, because the impeller rotates at constant frequency, the diffuser entry condition is composed of strong periodic components generated by the impeller blades. Together with these periodic components, small scale eddies passing through the diffuser inlet section are generated by the broad-band turbulence from the impeller[3].

Because of the impeller periodicity and constant shaft frequency, the unsteadiness due to the impeller can be isolated from the complex, multi-scale flow entering the diffuser.

1. If the velocity field in the diffuser is sampled for *sufficiently long time*, i.e. a period containing many rotor rounds, the average of the samplings converges to the steady state flow $\bar{\mathbf{U}}(\mathbf{x})$. The characteristic frequency of this flow is zero. Both characteristic time and scale are not defined. This flow corresponds to the solution of the RANS problem in the diffuser; the solution is steady and effects of the unsteadiness are modelled as turbulent stresses.

2. The instantaneous flow is never equal to the total average. Unsteadiness enters the diffuser and propagates through it, and in the volute. The perturbation characterized by the largest scale is due to the interaction between the pump and the loop. Large tanks provided with a free level partially mitigate low frequency flow rate fluctuations. Very low frequency perturbation are also unstable and fill a band of low frequencies contributing to the low frequency noise in the loop. There exists a peculiar, sub-round unsteadiness in machines, at diminished flow rates, called rotating stall; measurements described in §2.2 demonstrate that there is no sharp rotating stall frequency in the pump under investigation.

3. The impeller round frequency injects unsteadiness in the diffuser, the correspondent scale is the impeller diameter D_2. Because the impeller is mounted on the shaft with some eccentricity and its channels are not equal, a low but sharply detectable frequency unsteadiness can be recognized $\bar{\mathbf{U}}(\mathbf{x}, k/\Omega)$ $k \in \mathbb{N}$.

4. The passage frequency, with the correspondent scale equal to the impeller blade pitch, is due to the periodic passage of the impeller vanes. Unsteadiness injected in the stator because of the rotor vane passage

$$\mathbf{U}^{\mathrm{S}}(\mathbf{x}, \Delta\phi) = \frac{1}{T^{\mathrm{R}}} \int_0^{T^{\mathrm{R}}} \hat{\mathbf{u}}(\mathbf{x}, t)\,\mathrm{d}t = Z^{\mathrm{R}}\Omega \int_0^{1/(Z^{\mathrm{R}}\Omega)} \hat{\mathbf{u}}(\mathbf{x}, t)\,\mathrm{d}t \tag{2.7}$$

   where Z^{R} is the number of blades of the impeller.

5. The inflow boundary conditions in the diffuser is dominated by the approaching of the impeller blade, as it determines the static pressure field, flow direction and velocity there. Because the mutual position of the impeller blade and the diffuser

[3] the flow outside the impeller is turbulent, a rough estimation of the Reynolds number can be done setting a characteristic velocity equal to the steady state, radial component of the velocity at the impeller outlet section $Q_{\mathrm{BEP}}/\pi D_2 b_2$ as follows,

$$Re_{\mathrm{BEP}} = \frac{Q_{\mathrm{BEP}}}{\pi D_2 b_2}\,\frac{D_2}{\nu} = \frac{Q_{\mathrm{BEP}}}{\pi \nu D_2 (b_2/D_2)} \approx 200\,000 \tag{2.6}$$

vane leading edge is the main parameter describing this unsteadiness, a rotor phase locked measurement is the best way to resolve these flow features including jets and wakes. The characteristic scale of the phase-locked flow is the fraction of impeller passage between consecutive delays, i.e. rotor phases at which measurements are performed. The time scale of this flow is the sampling period; in this investigation, the rotor passage (60°) is sampled 12 times, at 5° step. This is the unsteady component investigated in this work.

6. The impeller ejects a very turbulent flow ($Re = 200\,000$) that contains many scales. The small scale non-linearity and broad-band unsteadiness can be collocated in the velocity $\mathbf{u}(\mathbf{x}, t)$ that survives after having isolated and subtracted all the previous harmonics[4]. Scales in this flow go from very large (sub-round period) to the Kolmogorov scale.

Collecting all the components, it is possible to reconstruct the velocity as follows,

$$\hat{\mathbf{u}}(\mathbf{x}, t) = \bar{\bar{\mathbf{U}}}(\mathbf{x}) + \bar{\mathbf{U}}(\mathbf{x}, n/\Omega) + \mathbf{U}^{\mathrm{S}}(\mathbf{x}, m/(Z^{\mathrm{R}}\Omega)) + \mathbf{U}(\mathbf{x}, k\varphi) + \mathbf{u}(\mathbf{x}, t), \;\; n, m, k \in \mathbb{N} \quad (2.8)$$

where f_{c} is the sampling frequency, i.e. corresponding to the rotor phase delay between samplings.

Inserting the previous decomposition in the Navier-Stokes equations, it is possible to obtain a set of laws for the conditionally averaged flow, for instance the phase averaged flow, and a set of stresses that, like the Reynolds stresses, model the energy transfer between scales.

The presented PIV instantaneous velocity maps cannot provide a reliable decomposition and unsteadiness stresses computation because they are affected by relatively low signal to noise ratio; because the noise is a velocity fluctuation, separating turbulence from noise *a priori* is impossible.

The following analysis relies on global average and rotor phase average maps; because the average operator filters out broad-band unsteadiness and noise, clear results are expected even though instantaneous measurements are noisy.

Phase averaged velocity maps are computed in the diffuser at 12 impeller delays inside a rotor passage (60°), i.e. positions of the impeller vane trailing edge respect with the diffuser vane leading edge, the result is an ensemble average of rotor phase locked instantaneous maps,

$$\mathbf{U}(\mathbf{x}; \varphi) = \langle \hat{\mathbf{u}} \rangle (\mathbf{x}; \varphi) = \frac{1}{N} \sum_{n=1}^{N} \hat{\mathbf{u}}(\mathbf{x}; \varphi + 2n\pi), \quad (2.9)$$

where N = 200 is the number of vector field computed at each rotor delay. The passage average velocity is estimated computing the mean map from the entire dataset, i.e. $12 \times 200 = 2400$ vector fields. These averages are affected by improved signal to noise ratio and are used to highlight the pattern of jets and wakes in the diffuser.

The proposed visualization method is based on the transport in the diffuser of the velocity triangle at the impeller discharge. The flow ejected by the impeller enters the diffuser with a certain dynamic pressure and angle, i.e. there exists a distribution of velocity triangles at the inflow boundary of the diffuser channel. Once the flow enters the diffuser, both the dynamic pressure and the angle of the flow evolve; hence it is possible to say that the velocity triangle evolve point-to-point and in time in the diffuser because of convection.

The method is based on the following observation: the phase-averaged velocity triangle at the inflow section of the diffuser follows the impeller channel *sliding* on the diffuser

[4] called *deterministic* in some literature

inflow section, this is the basic idea behind the sliding mesh technique in CFD investigations over turbomachines. Because there exists a global average of the velocity triangle at the exit section of the impeller, whose circumferential trend depends only on the position of the diffuser vanes leading edge, the unsteadiness in the velocity triangle at the impeller discharge section also slides along the diffuser entry section following the impeller blades.

Moreover, the pump under investigation is provided with backward oriented impeller blades, this is a quite standard feature in industry because it promotes effectiveness even though it slightly penalizes the head rise. The potential flow velocity triangle at the discharge section of such impeller is a standard in machine flow analysis; the impeller discharge velocity in the diffuser frame of reference (V_2/U) can be computed from the impeller velocity $U = \pi\Omega D_2$ as shown in (2.10).

$$\left(\frac{V_2}{U}\right)^2 = \left(1 - \frac{W_2}{U}\cos\beta_2\right)^2 + \left(\frac{W_2}{U}\sin\beta_2\right)^2 = 1 + \left(\frac{W_2}{U}\right)^2 - 2\frac{W_2}{U}\cos\beta_2 \tag{2.10}$$

Because either β_2 was corrected for the slip or not, it would always be $0 < \beta_2 < 90°$, then $\cos\beta_2 > 0$ and:

$$\lim_{W_2\to 0}\left\{\left(\frac{V_2}{U}\right)^2\right\} = 1^- \tag{2.11}$$

monotonically because:

$$\lim_{W_2\to 0}\left\{\frac{\partial V_2}{\partial W_2}\right\} = \lim_{W_2\to 0}\left\{\frac{2W_2 - 2U\cos\beta_2}{(U^2 + W_2^2 - 2UW_2\cos\beta_2)^{1/2}}\right\} = -2\cos\beta_2\,, \quad 0 < \beta_2 < 90° \tag{2.12}$$

hence the kinetic energy per unit mass entering the diffuser reaches its maximum where W_2/U is null due to the blockage effect at the impeller wake. Moreover, where W_2/U reaches its maximum, the flow coefficient at the impeller discharge section $\Phi_2 = W_2U^{-1}\sin\beta_2$ also reaches its maximum and the diffuser inlet kinetic energy reaches its minimum. This simplified flow analysis refers to the velocity triangle of Fig. 2.20.

The diffuser inlet kinetic energy fluctuation due to the impeller blade passage is thus recognizable from the distribution of the phase averaged velocity $U_i(\mathbf{x},\varphi)$ inside the diffuser; nevertheless, the distribution of the phase locked fluctuation $u_i^S(\mathbf{x},\varphi)$ provides better information because the phase averaged flow is subtracted. Plotting the difference between the globally averaged flow kinetic energy and the passage average kinetic energy it can be possible to identify jets and wakes clearly.

Denoting the kinetic energy per unit mass of the phase averaged flow as $E_\mathrm{k}(\mathbf{x},\varphi)$ and $E_\mathrm{k}^S(\mathbf{x})$ for the global averaged flow - in the stator frame of reference - it is possible to compute and display both the quantities:

$$E_\mathrm{k}(\mathbf{x},\varphi) = \frac{1}{2}U_iU_i = \frac{1}{2}\langle\hat{u}_i\rangle\langle\hat{u}_i\rangle = \frac{1}{2}\langle\hat{u}_i\rangle^2 \tag{2.13}$$

$$E_\mathrm{k}^S(\mathbf{x}) = \frac{1}{2}U_i^SU_i^S = \frac{1}{2}\langle\langle\hat{u}_i\rangle\rangle^S\langle\langle\hat{u}_i\rangle\rangle^S = \frac{1}{2}(\langle\langle\hat{u}_i\rangle\rangle^S)^2 \tag{2.14}$$

where $\langle\hat{u}_i\rangle$ is the phase averaged velocity in the diffuser and $\langle\langle\hat{u}_i\rangle\rangle^S$ is the globally averaged velocity field in the diffuser (stator) due to the sliding inflow boundary condition imposed by the impeller. Finally, it is possible to define a scalar quantity that describes the position and shape of the rotor wakes while they are convected through the diffuser, with (2.15).

$$\Delta(\mathbf{x},\varphi) = \frac{1}{2}\left[\langle\hat{u}_i\rangle^2 - (\langle\langle\hat{u}_i\rangle\rangle^S)^2\right] \tag{2.15}$$

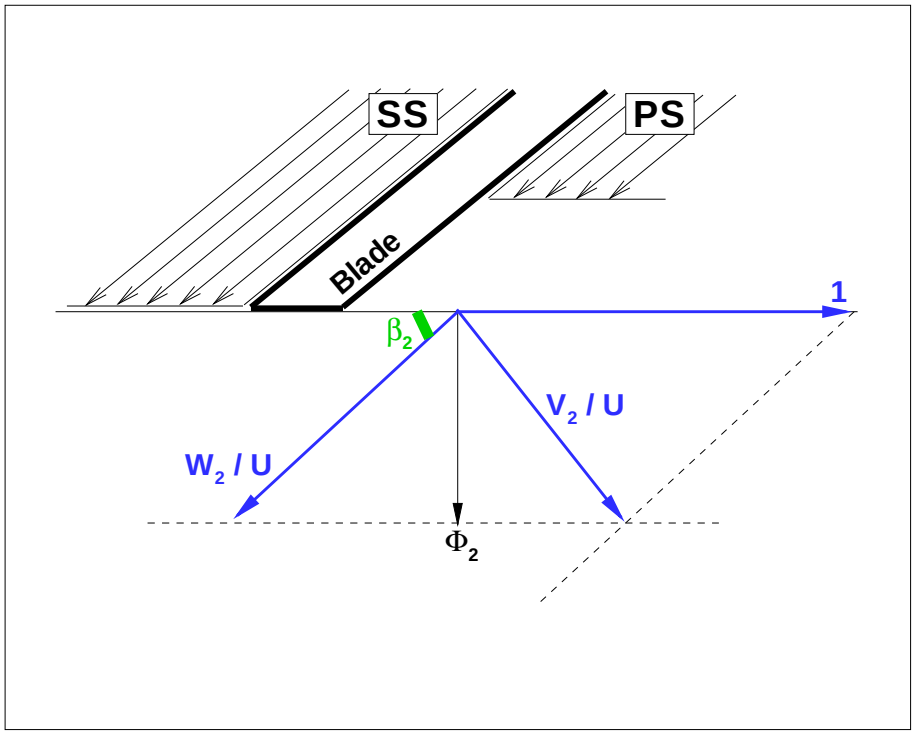

Figure 2.20: **Simplified velocity triangle at the discharge section of the impeller**

The scalar quantity $\Delta(\mathbf{x}, \varphi)$ can be called *cyclic unsteadiness*, as it provides information strictly over the periodic effect of the rotor vane over the flow inside the diffuser. The cyclic unsteadiness is not a kinetic energy (it can be negative), it is a parameter of comparison between the kinetic energy of two different flows in the same diffuser, obtained with different averages over the same dataset.

Jet and Wake at 120% BEP

In the following, the phase averaged velocity and the cyclic unsteadiness are plotted for three off-design configuration in order to elucidate how variations in the flow rate affect the Jet and Wake distribution in the diffuser.

Fig. 2.21 shows the phase averaged velocity distribution in the diffuser at $\phi = 0°$, i.e. the reference position of the impeller. Wakes from the impeller trailing edges are not clearly visible but the velocity diminishes at the impeller channel discharge section, as described in §2.4. The flow is separated at the vane convex side leaving a low velocity zone downstream the vane, the velocity in the channel diminishes substantially at the discharge section of the diffuser and the tongue is impinged by the stream dividing it into two parts, one is delivered at the volute discharge section - with a localized acceleration at the tip of the tongue - and the rest is re-collected in the volute.

The cyclic unsteadiness illustrated in Fig. 2.22 allows the jet and wake to be fully described, see §2.4. The alternate velocity distribution is convected through the channel, it is damped by the low-pass filter effect of the stator, but it survives beyond the discharge section. The tongue, in particular, is impinged by a periodic flow likely resulting in an alternate mechanical stress.

The evolution of phase averaged wakes is illustrated at four rotor phases from Fig. 2.22 to Fig. 2.24 but data have been taken for an entire rotor blade passage, i.e. 60°. Not only the leading edge of the diffuser divides the wakes, it also cause a shift of one wake section respect to the other. In fact, the jet and wake pattern is convected in the diffuser channel

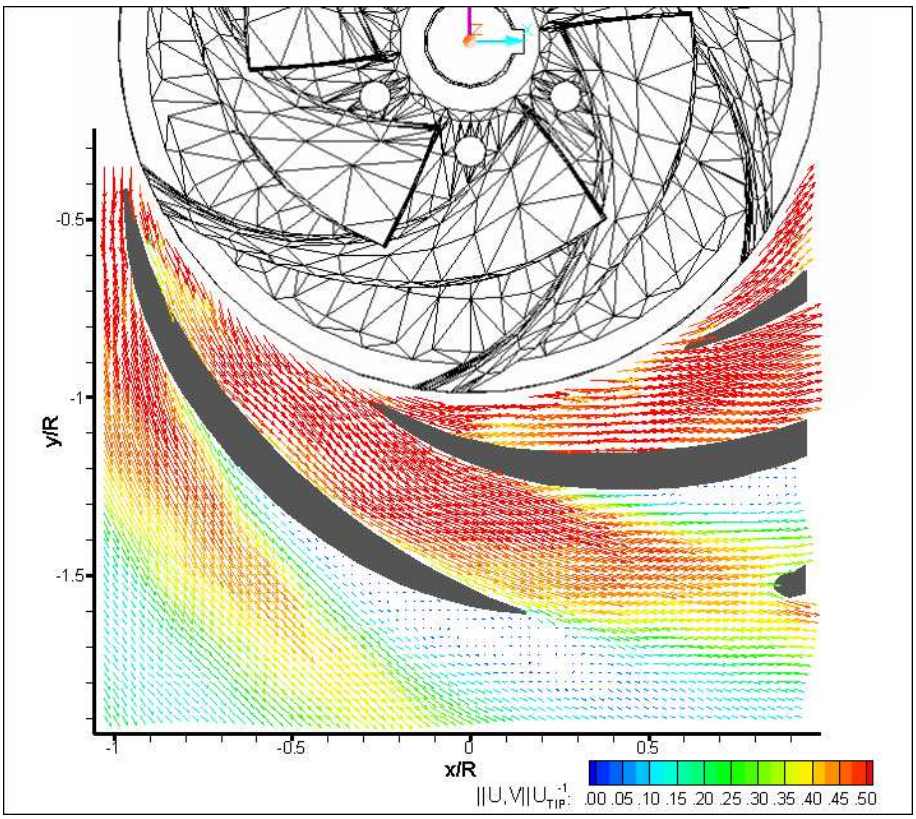

Figure 2.21: **Phase averaged velocity distribution in the tongue region of the diffuser, $\phi/\phi_{\mathrm{BEP}} = 1.2$, 50% span, $\varphi = 0°$ rotor angular position; the velocity is normalized with the impeller peripheral speed**

and the transport velocity at the pressure side of the vane is different from the transport velocity at the suction side as described in §2.3.2. As the wake enters the channel, it is subjected to higher downstream convection at the convex side and a mismatch in the position of the wake occurs across the vane. Thus, the wake is first distorted and then transported in the channel, where the diffuser damps the velocity peaks creating smoother alternate pattern.

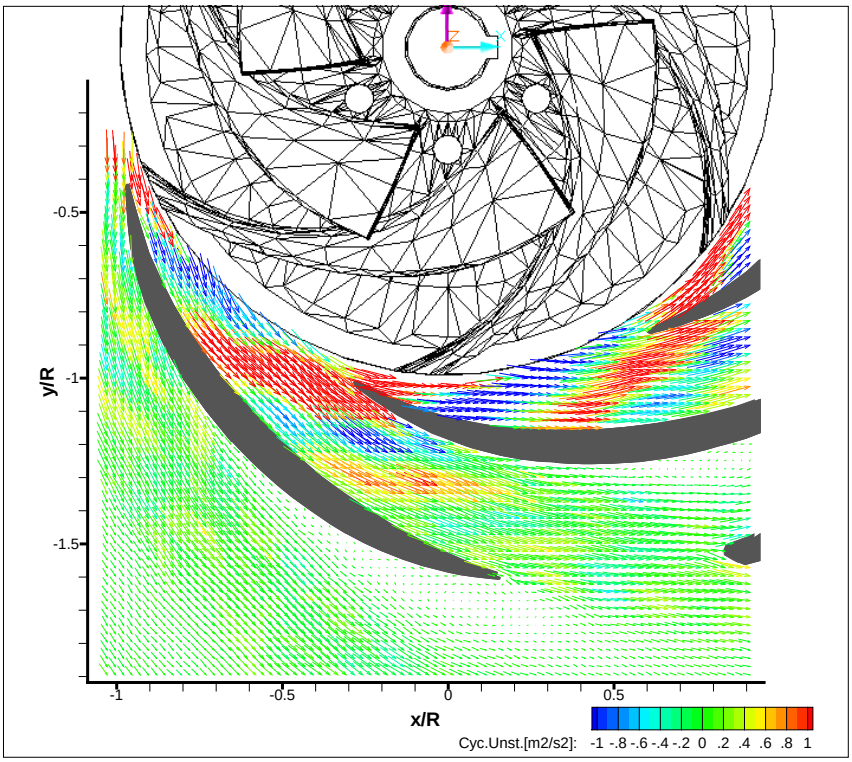

Figure 2.22: **Phase averaged velocity (vectors) and cyclic unsteadiness (colors) distribution in the tongue region of the diffuser, $\phi/\phi_{\mathrm{BEP}} = 1.2$, 50% span, $\varphi = 0°$ rotor angular position**

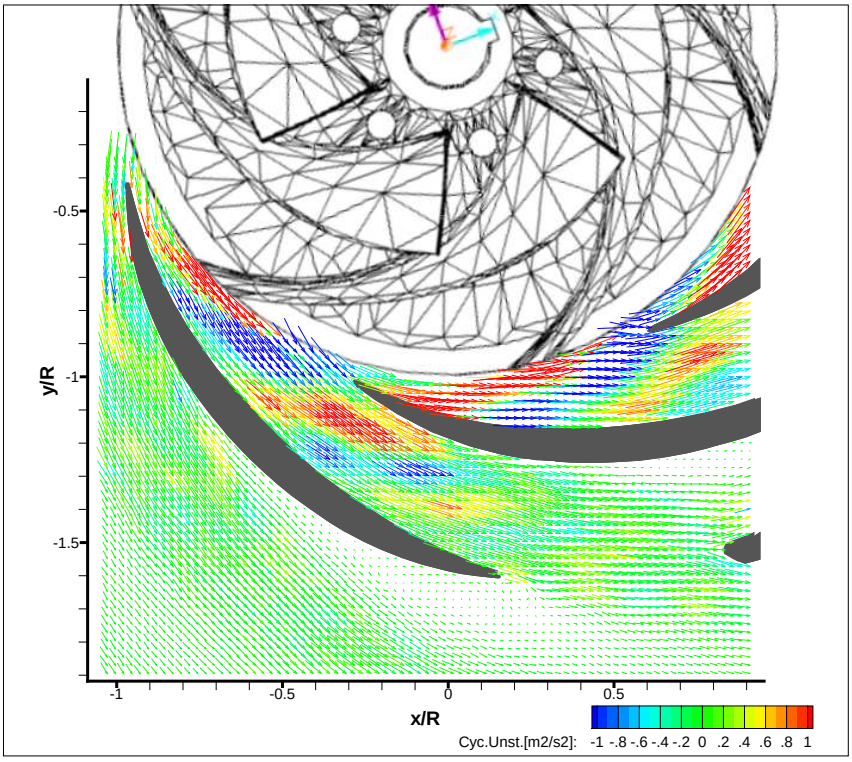

Figure 2.23: **Phase averaged velocity (vectors) and cyclic unsteadiness (colors) distribution in the tongue region of the diffuser, $\phi/\phi_{\mathrm{BEP}} = 1.2$, 50% span, $\varphi = 20°$ rotor angular position**

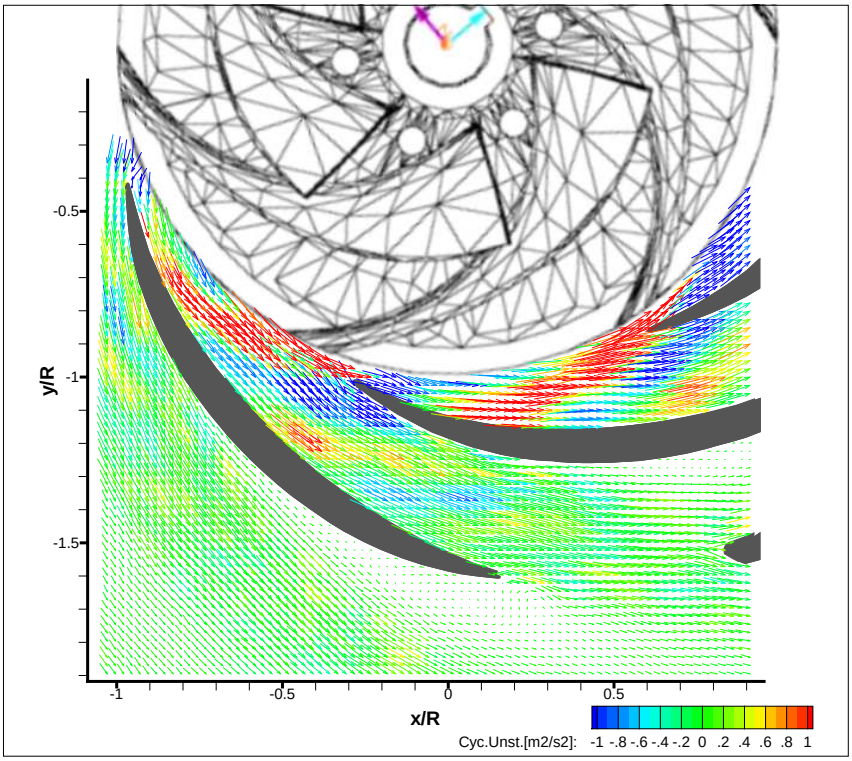

Figure 2.24: **Phase averaged velocity (vectors) and cyclic unsteadiness (colors) distribution in the tongue region of the diffuser,** $\phi/\phi_{\mathrm{BEP}} = 1.2$**,** 50% **span,** $\varphi = 40°$ **rotor angular position**

Jet and Wake at 80% BEP

At diminished flow rate, the pressure side is likely on the convex side of the vane, thus the impeller wake is divided and deformed accordingly. The section of the wake that is located along the suction side is faster than the section on the pressure side and a mismatch occurs across the vane; in Fig. 2.27, for example, the wake on the suction side (red) almost align with the jet (blue) on the pressure side.

An alternate jet and wake pattern is noticeable in the channel but it survives less than at 120% BEP; moreover, the discharged flow does not imping the tongue and the unsteady flows is delivered directly at the pump exit section.

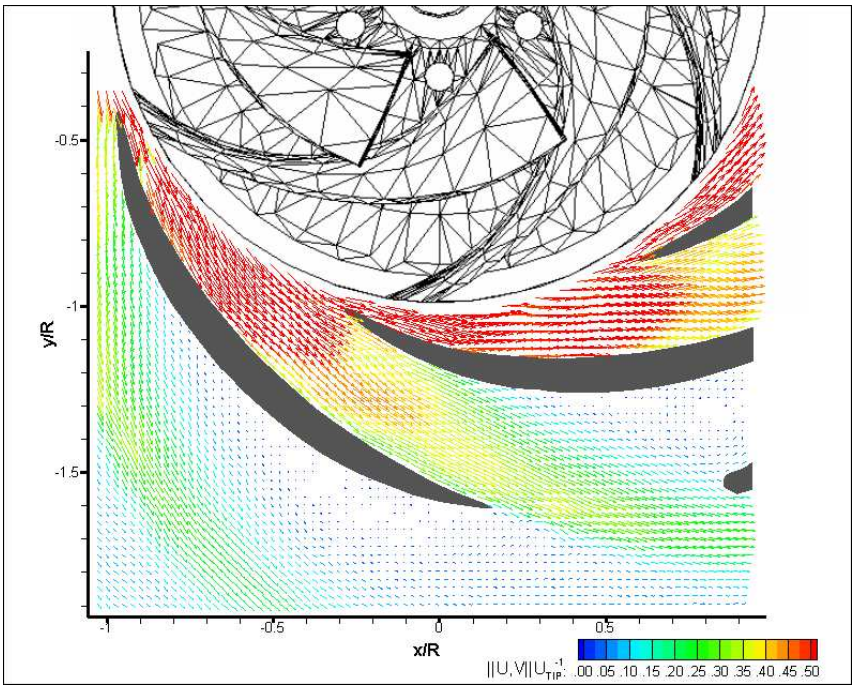

Figure 2.25: **Phase averaged velocity distribution in the tongue region of the diffuser, $\phi/\phi_{\mathrm{BEP}} = 0.8$, 50% span, $\varphi = 0°$ rotor angular position; the velocity is normalized with the impeller peripheral speed**

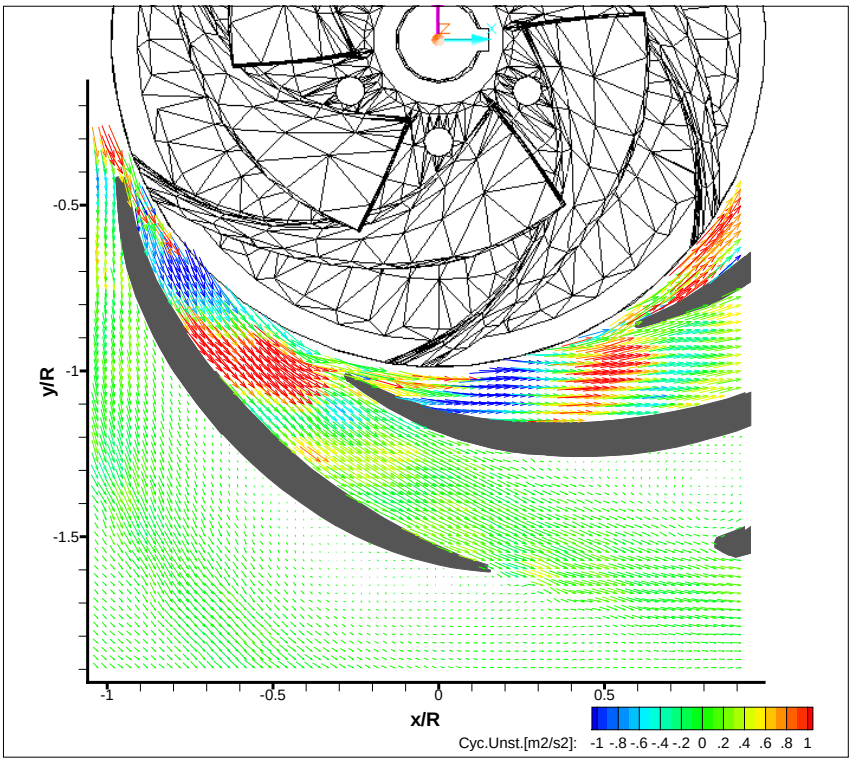

Figure 2.26: **Phase averaged velocity (vectors) and cyclic unsteadiness (colors) distribution in the tongue region of the diffuser, $\phi/\phi_{\mathrm{BEP}} = 0.8$, 50% span, $\varphi = 0°$ rotor angular position**

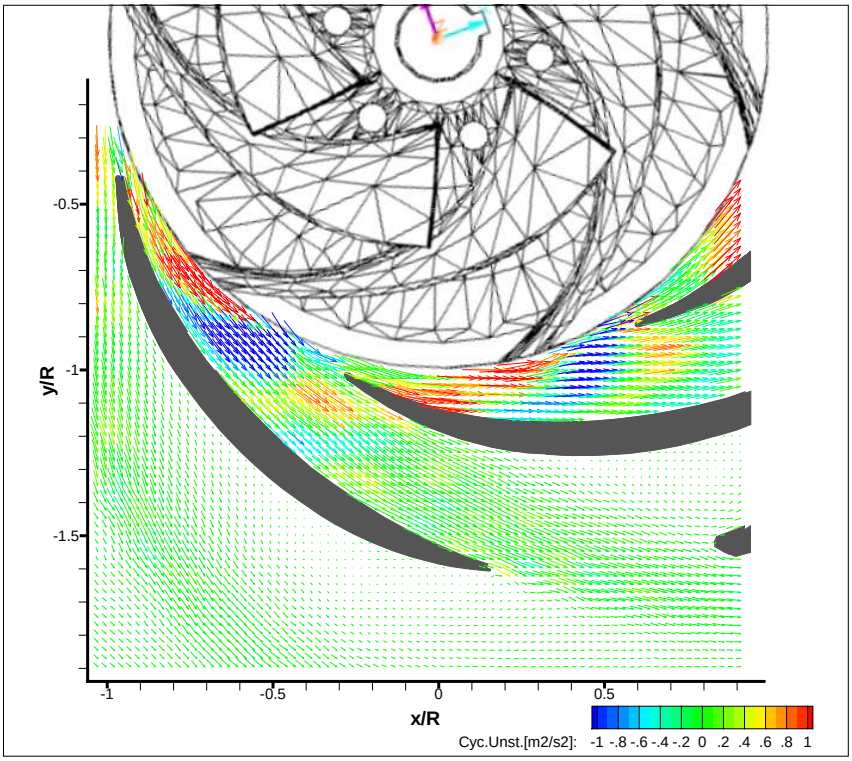

Figure 2.27: **Phase averaged velocity (vectors) and cyclic unsteadiness (colors) distribution in the tongue region of the diffuser,** $\phi/\phi_{\mathrm{BEP}} = 0.8$**,** 50% **span,** $\varphi = 20°$ **rotor angular position**

Jet and Wake at 60% BEP

At very low flow rate the velocity at the exit section of the impeller is directed tangentially; Fig. 2.29 shows that indeed the flow impinges the leading edge of the diffuser blade. The pressure side of the vane blocks the flow, part of it turns around the edge and enters the next channel with a radial reversed component, the rest proceeds along the suction side towards the volute.

Fig. 2.29 - Fig. 2.32 show that the wake is substantially blocked at the diffuser inlet, the alternate jet and wake pattern in the channel is hardly noticeable; in fact, while the wake (or jet) is facing the vane leading edge, part of it is convected downstream by the suction side flow. As a result, the channel is filled with the wake (or jet) and the alternate pattern vanishes.

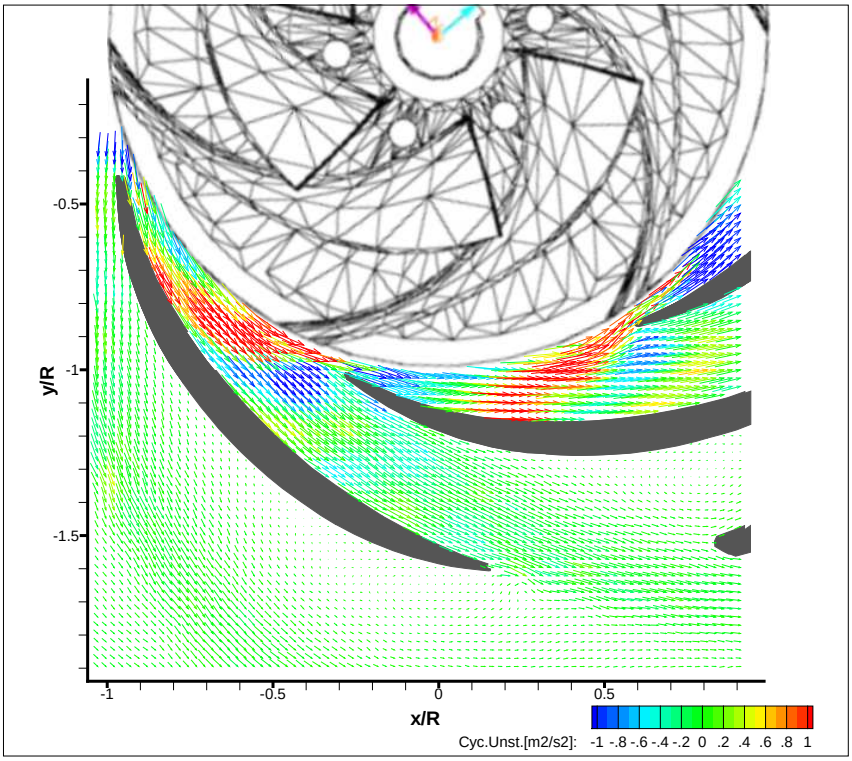

Figure 2.28: **Phase averaged velocity (vectors) and cyclic unsteadiness (colors) distribution in the tongue region of the diffuser,** $\phi/\phi_{\mathrm{BEP}} = 0.8$, 50% **span,** $\varphi = 40°$ **rotor angular position**

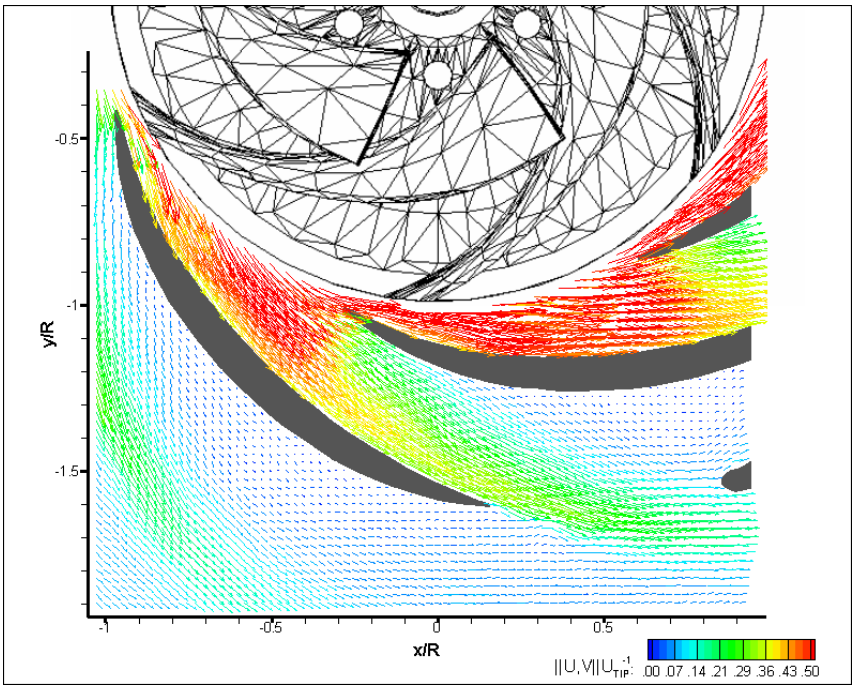

Figure 2.29: **Phase averaged velocity distribution in the tongue region of the diffuser,** $\phi/\phi_{\mathrm{BEP}} = 0.6$, 50% **span,** $\varphi = 0°$ **rotor angular position; the velocity is normalized with the impeller peripheral speed**

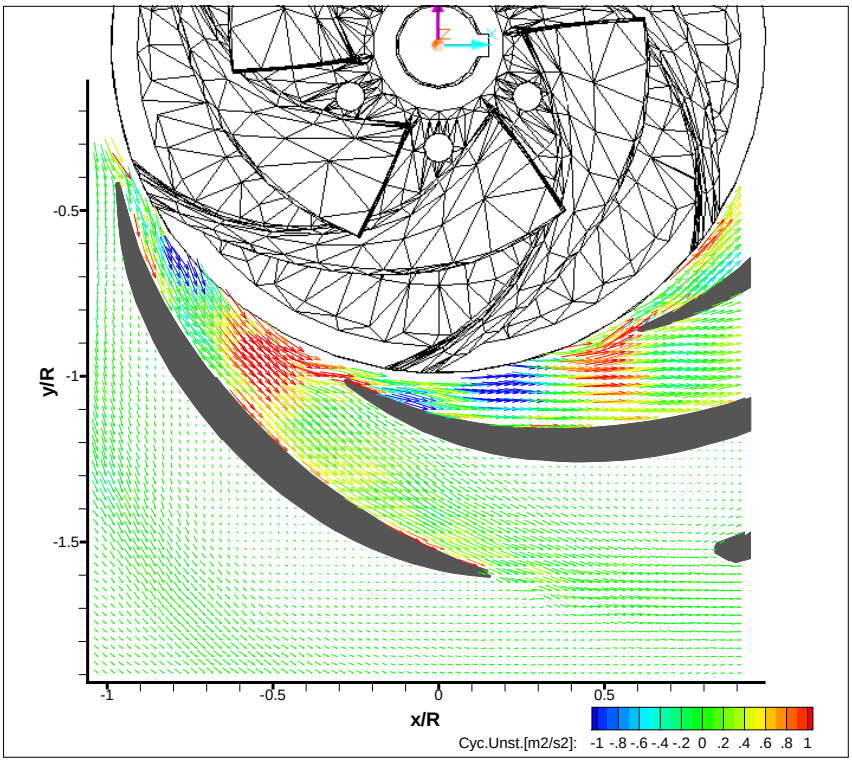

Figure 2.30: **Phase averaged velocity (vectors) and cyclic unsteadiness (colors) distribution in the tongue region of the diffuser, $\phi/\phi_{\mathrm{BEP}} = 0.6$, 50% span, $\varphi = 0°$ rotor angular position**

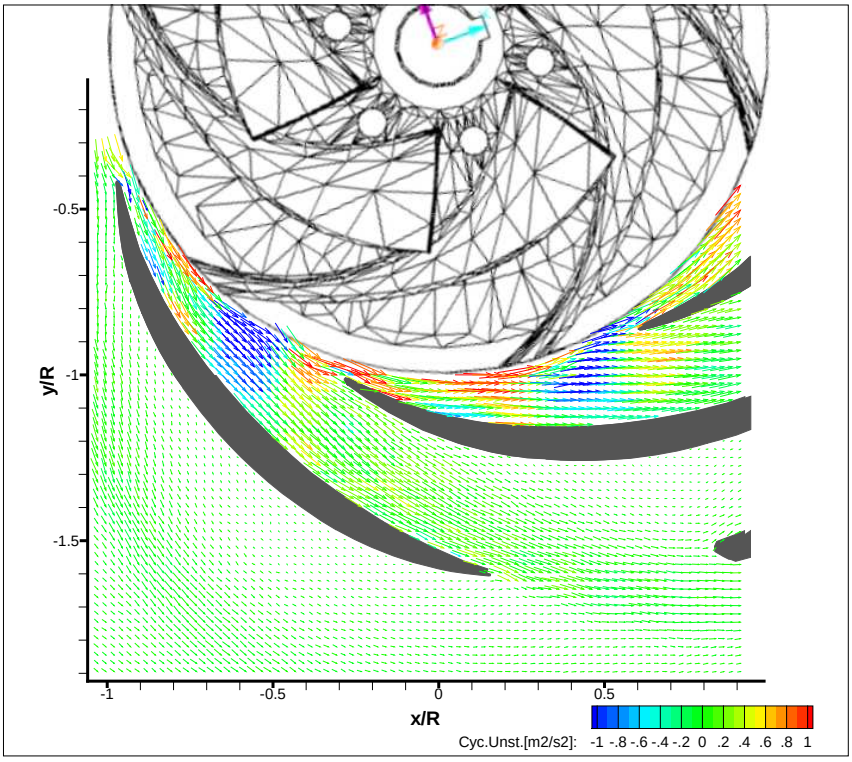

Figure 2.31: **Phase averaged velocity (vectors) and cyclic unsteadiness (colors) distribution in the tongue region of the diffuser, $\phi/\phi_{\mathrm{BEP}} = 0.6$, 50% span, $\varphi = 20°$ rotor angular position**

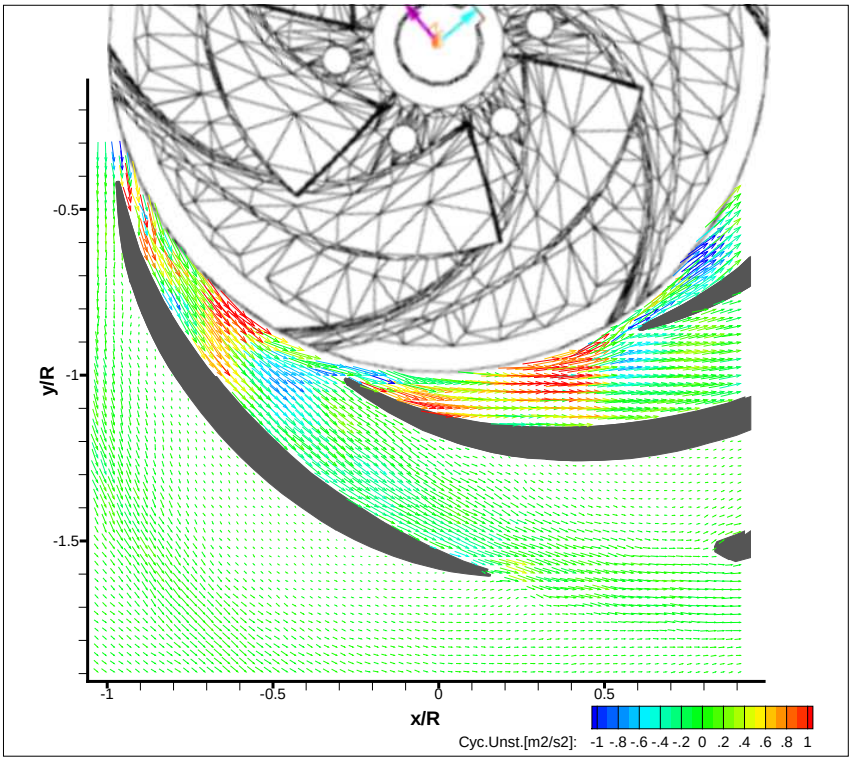

Figure 2.32: **Phase averaged velocity (vectors) and cyclic unsteadiness (colors) distribution in the tongue region of the diffuser,** $\phi/\phi_{\mathrm{BEP}} = 0.6$**,** 50% **span,** $\varphi = 40°$ **rotor angular position**

2.5 Summary and Conclusions

The flow inside the tongue region of a vaned diffuser centrifugal pump has been investigated by means of 2DPIV over the midspan blade to blade plane, at various flow rates.

The machine is built fitting a commercial, high specific speed impeller into a transparent vaned diffuser and volute, which are made of acrylic (PMMA). The pumped fluid is water seeded with spherical glass particles.

The pump is operated at constant speed and variable flow rate; first the head/efficiency curve is derived form a steady state power test processing static pressure and shaft torque measurements. The flex point of the head curve, which is common in high specific speed pumps, shows an increased dispersion of data points, revealing the presence of flow instabilities.

Unsteady Pressure Measurements

In order to investigate the presence of a rotating stall, the static pressure is measured at the diffuser wall with a time-resolved technique: a couple of fast response pressure transducers flush-mounted on the pipe wall at the inlet section and on the hub of the diffuser. The power spectrum density of the pressure fluctuations at the wall reveals two narrow peaks at the impeller round, because it is not axis-symmetric, and at the bade passage frequency. As the flow rate diminishes, the signal becomes noisy with increased energy just below the round frequency; no clear peak can be linked to a rotating stall except at 40% of the best efficiency point flow rate, where a peak is detected at the inlet section at $\sim 50\%$ the impeller frequency. This harmonic is likely due to a recirculation cell at the inlet of the impeller with an unsteady suction pre-swirl.

Mean Flow Analysis

The flow is investigated at the nominal shaft speed and best efficiency point flow rate, plus one case at augmented capacity (120% BEP) and several cases at diminished capacity. PIV velocity maps are sampled at fixed rotor phases covering 60°, i.e. one impeller passage, with 5° angular steps.

The data is globally averaged in order to obtain the mean flow in the diffuser. At the BEP flow rate the flow discharged by the impeller enters the diffuser with nearly zero incidence, the vane suction side is a free vortex line in the first chord section, and proceeds in the channel where the velocity decreases because of the forced diffusion effect. The flow remains attached to the blade until the thickness reduces to approach the trailing edge. At the section of thickness reduction, the flow separates at the convex side of the vane while it remains attached at the concave side until the trailing edge is encountered; then, the blade generates a low velocity wake.

As the flow rate is increased (120%BEP) the incidence on the diffuser vane is not neutral, the flow is more radial than at BEP and the vane is loaded positively, i.e. the convex side is the suction side and the mean velocity of the fluid is higher there.

Conversely, at diminished flow rates, e.g. at 80% BEP, the incidence is negative and the convex side is the pressure side. The flow discharged by the diffuser channel is attached to the suction side (concave) and it does not imping the tongue but it is delivered almost entirely towards the pump discharge section.

At very low flow rate (40% BEP), the velocity at the impeller outlet section is very tangential, there is a separation of the flow at the leading edge of the diffuser vane, with strong vorticity generated at the tip. High velocity flow coming from the impeller is stopped at the channel entry section, and some of it proceeds along the suction side. At this very low capacity, the flow discharged by the investigated channel impinges the tongue as it did at high flow rates, but indeed not at BEP and moderate capacities.

Cyclic Unsteadiness Analysis

The phase averaged flow allows the direction of the diffuser inlet velocity to be studied for twelve rotor angular positions, from the reference angle to+60°, covering one impeller blade passage.

The wake of the impeller blade has high momentum, in the diffuser frame of reference, because the rotor has backward-oriented blades. The radial component of the velocity, due to the capacity discharged by the impeller channel, lowers the velocity magnitude. Moreover, because of the blockage effect of the impeller trailing edge and the no-slip condition, the flow in the wake enters the diffuser with very tangential direction. As a result, the incidence over the leading edge of the diffuser vane is unsteady and contains at least the impeller blade passage frequency, i.e. incidence becomes strongly negative periodically . The flow in the channel and the pressure side separation is not affected by the incidence periodic variation, or at least it is not affected appreciably.

In order to analyze the evolution of the jet and wake pattern in the diffuser, the phase averaged velocity has to be processed because the velocity variation between the wake and the jet is smooth and the wake pattern is not clear. Because the velocity of the fluid in the wake is higher than the one in the jet and the difference has to be highlighted, the “cyclic unsteadiness" is computed as the difference between the kinetic energy of the phase averaged flow and the kinetic energy of the mean flow, at a given capacity.

This quantity is not a kinetic energy because it can be negative, it is the result of a comparison between the phase averaged flow and the total average, highlighting the variation of a local signal - the phase averaged kinetic energy - computing its square and

subtracting point to point the square of the total average. Once the cyclic unsteadiness has highlighted the jet and wake pattern, its evolution in the diffuser channel is presented for three off-design conditions.

First, at high capacity the alternate pattern of jets an wakes is smoothed in the channel; nevertheless, it survives far beyond the outlet section. As a result, the tongue is impinged by a periodic flow. Then, at diminished capacities, the diffusion effect in the channel damps the wake before it exits the diffuser. At very low capacity, the leading edge of the diffuser vane blocks the flow and part of it is convected in the blade to blade plane downstream the suction side. The wake, or eventually the jet, slows down and almost stops at the leading edge; as a result, no alternate pattern is recognizable inside it.

At each flow rate, the wake is divided into several sections by the leading edge of the diffuser vane, one of the section faces the convex side of the vane and the other faces the concave side. The wake is transported and diffused by the velocity field but the characteristic time of diffusion, which is a turbulent diffusion, is too large to modify it substantially in the first section of the channel; thus, the wake is transported.

At high flow rate, the mean flow is fast on the convex side and slow on the concave side, this velocity jump across the vane transports the sections of the wake (or jet) differently with two consequences: first, the phase difference between the jet and the wake changes along the vane; second, the wake (or jet) in the channel starts as a spiral section and then is progressively distorted, likely promoting a three dimensional motion and turbulent mixing.

At lower capacities the distortion of the wake still occurs but it is opposite because the tangential entry velocity in the diffuser imposes a fast stream on the concave side and a slow stream on the convex side of the vane. Thus, the wake is transported faster on the convex side and the wake (or jet) is distorted accordingly.

2.6 Suggested future developments

The PIV technique has demonstrated to be very powerful in the description of the flow in the diffuser because the information is spatially distributed with high resolution, and the resolution can be easily improved. No information about the pressure distribution is given, but the velocity field can be described in detail.

The presented investigation has limitations: only the in plane velocity, and out of plane vorticity are shown, and there are many other kinematic quantities that could be derived such as the in plane strain-rate, the in plane Reynolds stresses, the 2D rate of production of in plane turbulent kinetic energy etc. None of these are presented here because the primary quantity (in plane velocity), let us call it the signal, is noisy. The noise level is acceptable if only primary quantities are investigated, like velocity, spatial integrals of the velocity or first derivatives like vorticity. Presented maps are also affected by corrupted zones, masked out during post-processing. The more the velocity is processed, e.g. differentiated in space, subtracted the average etc, the more the signal to noise ratio diminishes and the more unrealistic features appear in the maps.

The PIV output is corrupted because images are corrupted; specifically, the diffuser and volute are transparent but the impeller is not, reflection of laser light generates halos and bright zones where the image is saturated and no particle displacement can be recognized. Moreover, the machine is pumping water whose refractive index differs from the one of the acrylic; as a result, the image is distorted and shadows are cast inside the diffuser generating blind zones. The distortion of the image can be corrected building a dummy diffuser in which a dotted target provides the transfer function for correction. The process of generating a dummy diffuser and correcting the images is difficult and justifiable

only if the corrections were affine (linear) transformations such as rotation and dilations, or non-linear low-grade polynomial transformations like perspective correction. Because of the refractive index mismatch, the correction is a non-straightforward deconvolution, i.e. extremely difficult and sensitive to errors.

In conclusion, this investigation can develop in the future on two separate ways: studying how variations in the geometry or working point of the pump affect the inner flow, or studying peculiar fluid dynamic phenomenon that occur in the diffuser.

The first approach is more "industry oriented", and can be a validation for CFD codes. There is no need to improve the facility because velocity and vorticity are sufficient for describing the flow at industrial level. It can be said that a good programmed CFD code can predict the flow induced by a given geometry, and this numerical experiment is really less expensive than a laboratory experiment, from this point of view the proposed evolution of the work may seem useless. On the other hand, generally speaking, the industrial approach on CFD is not really refined, especially in the pump business. Most of the arbitrary values are set in the codes by experience, i.e. codes are "tuned" to the problem, and only very large scale results, like the performance curve or large scale passage flows, are fully trustable. Because the CFD provides the curves and the inner flow, being able to map the real flow and compare it with numerical result may help to generate a database of industrial cases, or even validate CFD computations.

The second approach is more "academia oriented". The flow in the diffuser is largely dominated by potential flow effects, easily computable with solvers. Nevertheless, locally, the flow may be very complex, and this is a constant feature of turbomachines, codes fail in these locations; for example because they are based on the turbulence diffusion model, thus they cannot model turbulence kinetic energy back-scatter and turbulence overproduction occurring in isolated zones.

PIV can be a powerful tool for investigating these local non-equilibrium conditions in order to refine turbulence models. Turbomachines are excellent environments for studying complex and non-equilibrium flows, but these phenomena are confined in boundary layers, local impinging wakes, mixing planes etc. As a result, high magnification imaging systems should be used and quantities to be computed would require strictly noiseless primary signal, i.e. sharp and clear images.

For example, in the centrifugal pump studied in this work, the impeller-diffuser gap is unusually narrow to enhance unsteady rotor-stator effects. A very turbulent flow is discharged by the impeller and impinges the diffuser vane leading edge, because of the reduced gap, the strain-rate level there is large. Moreover, leading edges of the diffuse vanes are impinged by a pattern of wakes, i.e. high kinetic energy flows, and jets, i.e. lower kinetic energy flows. As the turbulent wakes interact with the mean flow strain field in the vicinity of the vane leading edge, the production rate of turbulent kinetic energy is activated ([59]) and the flow is really in non-equilibrium. In order to study such a flow, a high magnification PIV system must be set up and pointed towards the vane leading edge and the machine must pump a fluid whose refractive index is the same of the acrylic casing, in order to have perfect images.

Part II

The Evolution of the Tip Leakage Vortex in an Axial Water Jet Pump

Introduction

The Water-jet Pump

Water-jet pumps can be adopted as propulsive systems for shallow and deep water operations: jet skis, jet-boats, torpedoes and submarines[5].

The first water-jet system was invented following the evolution of the shrouded marine propeller. It is known that the tip speed of standard propellers is limited by the onset of cavitation; attached cavitation on the suction side and cloud cavitation in the passage change the suction side static pressure distribution as well as the cavitated tip vortex dissipates circulation and produces noise, making submarines easily localizable by acoustic systems.

The cavitation margin of shrouded propellers is larger than of unshrouded ones because the end wall effect raises the dynamic pressure just upstream the leading edge of the rotor, that turns into augmented static pressure at the stagnation zones like the leading edge, which prevents the onset of cavitation.

The rotor of a water jet pump is completely enclosed in a casing, and downstream of it a stator aligns the stream to the machine longitudinal axis, converting the discharged angular momentum, which is not effective for the thrust, into additional linear momentum. Because the momentum of the jet is opposite to that of the craft, a forward thrust occurs.

Jet thrust systems are very effective in shallow water operations as the pump does not need be submersed, if the intake is below the water level and the pump is correctly primed, the propulsive unit can be located above the sea level.

The total wet surface of water-jet units is larger than of propellers, thus a reduction in the effectiveness is expected; nevertheless, the energy density of these machines is remarkable, due to their compactness and high rotational speeds, as well as low-noise behavior at almost all regimes. Moreover, a steerable nozzle can be mounted on the craft, largely improving the maneuverability.

The Tip Leakage Vortex

There are various sources of efficiency loss in a water-jet pump. Upstream the discharge nozzle, which produces the jet, a water-jet pump is essentially a high speed axial pump, and all the common energy losses of axial pumps can be found. Among all the phenomena involved, one of the most important is undoubtedly the tip leakage flow an tip leakage vortex (TLV).

Although the TLV has been studied extensively, both experimentally and numerically, details about its inner structure are unknown. The leakage flow in the gap between the tip of a rotor blade and the casing end-wall is a complex fluid-dynamics phenomenon involving unsteady separation of the tip boundary layer, shedding of vortex filaments from the suction side edge, and subsequent roll-up of vorticity. Associated adverse effects include: localized efficiency losses ([21] [22], [23]), which scale with the loading of the blade ([24]), noise due to inherent pressure fluctuations ([25]), wear of the blade and casing surfaces, and cavitation in hydraulic machines ([26] , [27]). Adamczyk *et al.* [28] state, on the basis of numerical simulations, that the dynamics of the TLV also contributes to the onset of stall in compressors.

Several devices have been designed and tested numerically and experimentally in order to decrease the size of the TLV, i.e. the blockage effect on the through-flow ([29], [30]), as well as its strength, which is directly correlated with the inception of cavitation ([31], [32],

[5]for example the the Royal Navy Trafalgar-class, the US Navy Seawolf-class, and the French Navy Le Triomphant class

[33]). In all applications, detailed information about the TLV are essential for validating computations, and for designing competitive machines.

Observations and experiments have allowed the formulation of rudimentary theoretical models of the TLV, for instance, the Rains Jet Model ([43]), the Compound Vortex Model ([44]), and the similarity analysis proposed by CHEN *et al.* [45]. These models do not resolve the inner structure of the vortex, and consequently cannot fully predict many of related adverse effects.

Probing the tip leakage flow experimentally is a major challenge, whereas computational techniques inherently involve assumptions and models that may not be appropriate for this complex flow. For example, models based on turbulent viscosity theory overestimate the production-rate of turbulent kinetic energy because they cannot predict the inverse cascade, i.e. the energy transfer from small scale of turbulence to larger scales. As turbomachinery flows are never in equilibrium this limitation of the models has large effect over CFD computations, especially when one tries to compute the local flow rather than the performance of the entire machine. To avoid the computation of unrealistic turbulence levels, especially at stagnation points like the leading edge of a blade, some CFD codes allow the operator to locally *turn off* the production terms in the turbulence budget equation.

Another limitation in the CFD approach to the TLV is the multi-scale nature of the phenomenon, because the Reynolds number of the tip leakage flow in an axial pump is $\sim 10^3$ the turbulence spectrum is relatively broad, leading to large computational efforts in resolving the scales. Moreover, turbomachinery geometries are complex and that is particularly true at the tip of the moving blade, very close to the end-wall. There must be a trade-off between the size of the mesh and the CPU performance, and that rarely allows the tip clearance and end-wall to be correctly meshed.

Few characteristic examples of CFD approaches to the TLV are described in the following. For instance, FAN *et al.* [47] simulated the tip gap flow both in thermal and hydraulic machines adopting the RANS approach and k-ε closure model. Although this method is widely used in CFD of turbomachines, the closure model has fundamental flaws, e.g. it cannot resolve the unsteadiness of vortical structures properly, and in many cases overproduces turbulence. Consequently, code developers have looked for improved models, e.g. the computations of compressor rotors by GEROLYMOS and VALLET [48], which follow the turbulent energy dissipation model developed byLAUNDER and SHARMA [49], and JONES and LAUNDER [50]. This improved approach still has difficulties, e.g. in estimating boundary-layer separations. High-resolution RANS simulations carried out by FURUKAWA *et al.* [51], using the Baldwin and Lomax algebraic turbulence model, have resolved many features of TLV roll-up and growth, including vortex bursting. However, scarcity of relevant experimental data inherently prevents comparison of these simulations, in which the turbulence is modeled out, to actual flow and turbulence phenomena inside a TLV.

Measuring the tip gap flow in turbomachines is a difficult issue, althoughSTORER and CUMPSTY [52] succeeded in the evaluation of the intense, highly dissipative shear flow that originates between the clearance jet and the through-flow, probe methods such as flattened pitot tubes located at the end wall have been found to be extremely intrusive, and used mainly to investigate the clearance flow field as it emerges from the discharge section of rotors ([53], [53], [55], [56]). Probes are difficult to move and rotate in the rotor passage and they can sample a single point at each instant; thus, computing averages on the flow is unavoidable. Laser Doppler Velocimetry (LDV) can sample each component of the instantaneous velocity in a point without perturbing the flow ([57], [58]), but a complete flow map over a region cannot be evaluated instantaneously and spatial gradients of the velocity field can be computed only on averaged data and over coarse grids, as the LDV

signal comes from the scattering of light in an interference region that can only be moved sliding the laser beams.

Recent advances in flow measurement techniques, such as PIV, have greatly enhanced the ability of investigating internal flows, especially when the facilities are refractive index-matched. Optical index matching enables unobstructed measurements inside complex passages, such as rotors, including the flow and turbulence very close to boundaries. For instance, using the optical setup and facility described in UZOL *et al.* [42], SORANNA *et al.* ([59],[60],[61]) have investigated wake-blade and wake-wake interactions in a refractive index-matched axial pump.

PIV provides detailed velocity distributions, and has been adopted for turbomachinery research. For instance, SANDERS *et al.* [34] have investigated the flow in the stator of an axial transonic compressor using 2D-PIV over the blade-to-blade plane. LIU *et al.* [35] have studied the cross-flow plane of an axial compressor using Stereo-PIV, both the cited studies could not describe the flow near surfaces. In fact, samples recorded within machines are generally affected by low signal-noise ratio due to reflections from the casing and blades, limited optical access, and imperfect seeding with tracer particles. The latter is associated with inherent large differences between the specific gravity of the fluid and that of the particle. Hydro-turbomachine flows can be seeded with larger, almost neutrally buoyant particles, which are easier to distribute homogeneously. Moreover, because of the lower shaft speed, water-flow machines can be built partially or entirely of transparent materials, such as acrylic ([36], [37], [38], [39], [40], [41]). Because the refractive index of the water differs from that of acrylic, refraction phenomena distort the field of view and the laser sheet. Consequently, experiments in the Johns Hopkins University laboratory have been performed using a fluid whose refractive index is matched with that of the blades and casing ([42]), which greatly reduces the refraction/reflection disturbances. In this part of the paper, issues related to the implementation of PIV in an index-matched water jet pump are discussed, as well as tools developed to improve the data analysis are illustrated. Results are then used for examining the development of a TLV and associated secondary flows in a rotor passage.

Aim of the Research

The investigation examines the formation and development of a tip leakage vortex (TLV) within the rotor passage of an axial water-jet pump.

In order to investigate the TLV cross section, 2D particle image velocimetry (2D-PIV) measurements are performed in the meridional plane of the rotor. The pump is transparent and the refractive index of the working fluid matches that of the blade and casing, providing unobstructed views of the pump inner volume.

First, instantaneous vorticity and strain-rate maps give insights into the interaction between vortex filaments shed by the rotor blade tip and the casing end-wall boundary layer. Tip vortices shed from the blade are entrained into the inner part of the vortex, whereas the counter-rotating boundary layer vorticity first detaches from the end-wall and then wraps around the core. The point of detachment is unsteady. Both regions contain multiple vortices that do not merge in the blade passage. Vortex breakup occurs in the last part of the passage as the TLV migrates to the pressure side of a neighboring blade.

Secondly, the mean flow and turbulence in the rotor passage of the axial water-jet pump are investigated. Instantaneous particle image velocimetry (PIV) measurements of the flow in the meridional plane are phase-averaged with the rotor. Because of the high stagger angle of the rotor blade ($\approx 65°$ from the tangential direction) the TLV develops in the rotor passage as a very low pitch helicoid arc; hence, the distribution of the circumferential (out of plane) vorticity well describes the shape and size of the TLV section, which dominates

the passage flow. Secondly, the circulation of the meridional velocity allows a quantitative description of the strength of the TLV as well as of vortical flows/structures induced at the casing end wall, detached and entrained during the migration towards the pressure side of the following blade. The coherence of the averaged TLV decreases but the strength remains almost constant during the meandering and subsequent bursting.

The vorticity layer that connects the TLV with the tip of the blade, the center of the TLV, and the "stagnation" region generated at the end wall by the collision between the tip gap back-flow and the passage flow are unsteady. At early stages of the TLV evolution, the entraining of vortices in its outer branches is also unsteady and turbulent shear production rate is large there, like in the vorticity layer. The mean flow negative strain rate (compression) has a peak at the (unsteady) point of end wall vorticity detachment, and hence the in plane production of turbulent kinetic energy (TKE) is very high and positive there. The peak of unsteadiness inside the TLV is located in the vicinity of the center; interestingly, the level of 2D production is very low there.

In-plane data are insufficient for the understanding of the phenomenon, and that leads to conjectures; future, three-dimensional measurements are planned to shed light over these open issues.

2.7 Experimental Setup and Procedures

2.7.1 Test Loop

The water-jet pump is located inside a hydrodynamic loop that hosts more than one research project at the same time. In addition to being the subject for the turbomachinery research, the pump is used to drive the flow into three channels: the first is designed to study the accelerated boundary layer in a smooth wall contraction, the second is designed to measure the boundary layer over a rough wall and the third is the canopy flow test section. The pump branch is shown in Fig. 2.33. There is also a tank with a level, the tank can be pressurized inflating Nitrogen, or put under vacuum by sucking the Nitrogen with a vacuum pump. The loop can operate between $-30\,\mathrm{mm}_{Hg}$ and $+30\,\mathrm{psi}$ relative to the atmosphere, i.e. between 97 kPa and 308 kPa absolute pressure.

The flow rate can be set adjusting a valve composed of two perforated plates, by rotating one plate while keeping the other in place it is possible to set the flow rate precisely. The flow rate is measured by a transit time ultrasonic flow-meter that provides the mean velocity in the cross section of the pipe, whose diameter is 305 mm.

The facility is provided with a filtration unit to remove the tracer particles, the fluid can be filtered while recirculating in the loop or during the transfer of the solution in a separate storage tank and back. The injection of seeding is done by mixing the particles with a sample of fluid and sucking the mixture through a static pressure tap located at the pump casing wall.

Downstream the pump, a cooling section keeps the fluid at a temperature between 20°C and 25°C, a stable temperature is needed because the acrylic inside the pump is weakened by the contact with warm fluid and because the refractive index of the medium is a function of its temperature.

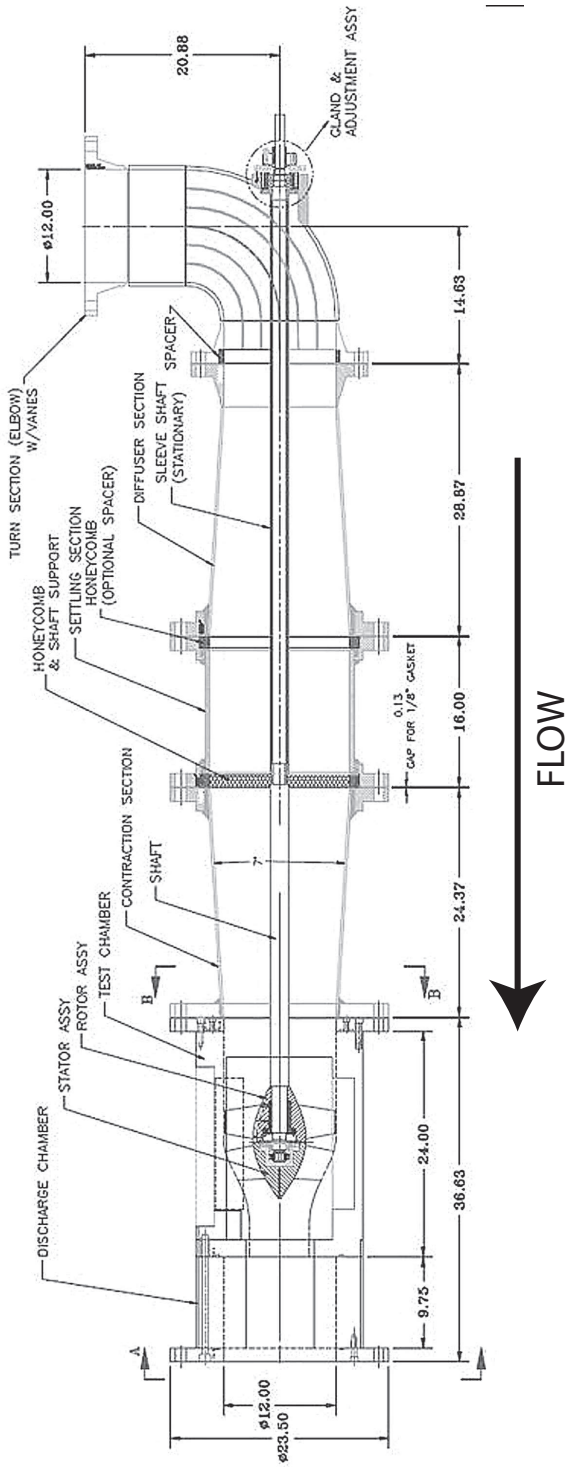

Figure 2.33: **Section of the pump test branch. Dimensions are in inches [JHU]**

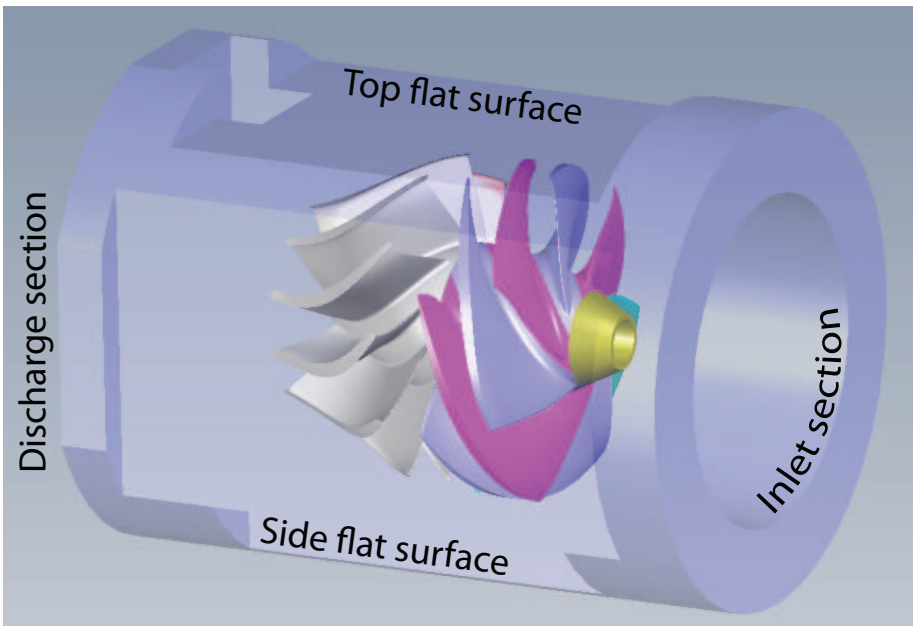

Figure 2.34: **Perspective view of the pump [JHU]**

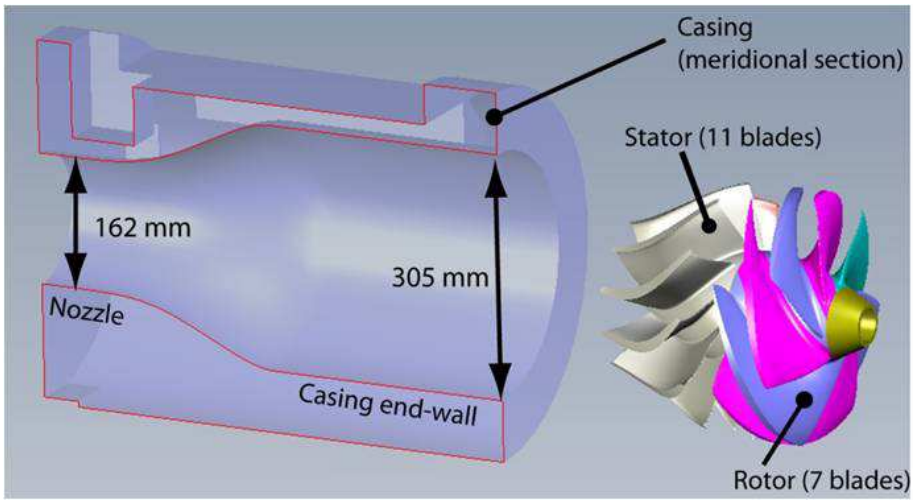

Figure 2.35: **Expanded view of the pump [JHU]**

2.7.2 Pump

The casing and blades are made of transparent acrylic (PMMA), the casing has been machined with a complex milling and polishing process in order to have large and flat external surfaces. Thus, the inner space is visible from multiple points of view, as illustrated in Fig. 2.34.

The present work focuses on the flow in a meridional section through the rotor, whose geometrical parameters are provided in Table 2.1.Fig. 2.34 and Fig. 2.35 show the shape of the casing, rotor and stator. Seven rotor blades are mounted on an ellipsoidal hub with maximum diameter 144.3 mm, because of the hub, see Fig. 2.38, the span of the blade varies from 101.6 mm at the leading edge to 80.3 mm at the trailing edge; the leading edge is bowed. The blade pitch at the tip is 136.8 mm while the tip profile chord-length is 258.5 mm, thus the solidity of the rotor is 1.89 at the tip. The casing cross section contracts from the inlet to the outlet sections of the stator with a discharge (nozzle) diameter of 161.5mm. The contraction hosts the eleven-blade stator, which generates an axial discharge flow.

The machine is driven by an AC motor whose speed is feedback-controlled to be within

Number of blades $[Z^{\mathrm{R}}]$	7
Tip chord length ($c\,[\mathrm{mm}]$)	258.5
Rotor diameter ($D_{\mathrm{R}}\,[\mathrm{mm}]$)	303.4
Casing diameter ($D\,[\mathrm{mm}]$)	304.8
Tip clearance (nominal) [mm]	0.7
Tip clearance (actual) ($h\,[\mathrm{mm}]$)	1
Clearance ratio (actual) ($2hD^{-1}$)	$7 \cdot 10^{-3}$
Blade pitch at tip ($\zeta\,[\mathrm{mm}]$)	136.8
Tip solidity $[c\zeta^{-1}]$	1.89
Rotor angular velocity ($\Omega\,[\mathrm{rad\,s^{-1}}]$)	94.2 (900 rpm)
Tip velocity ($U_{\mathrm{TIP}}\,[\mathrm{ms^{-1}}]$)	14.36
Flow rate ($Q\,[\mathrm{m^3s^{-1}}]$)	0.157
Flow coefficient ($\varphi = 2\pi Q\Omega^{-1}D^{-3}$)	0.37
Head coefficient ($\psi = (2\pi)^2\, gH\,(\Omega D)^{-2}$)	1.7
Torque coefficient ($k_{\mathrm{M}} = (2\pi)^{\ 2}\, M_{\mathrm{e}}\,\rho^{-1}\Omega^{-2}D^{-5}$)	0.14
Chord Reynolds number ($Re = c\bar{U}_{\mathrm{GAP}}\nu^{-1}$)	$5.15 \cdot 10^5$

Table 2.1: **Rotor geometry and reference data**

0.5% error. The motor is located outside the loop, and it is connected to the rotor on its front side by a 44.5 mm diameter shaft, which is supported by submersed ball bearings. Due to a 0.3 mm shaft misalignment, as measured from the flow images, the actual average tip clearance at the investigated meridional plane is 1 mm, rather than the nominal value, 0.7 mm.

Two honeycombs located in a settling chamber upstream the pump provide a uniform inlet flow. Information about machine performance, velocities, and Reynolds number is also given in Table 2.1. To match the refractive index, the working medium is a solution of sodium iodide in water, 62%-64% concentration by weight. The specific gravity of the liquid is 1.8 and the kinematic viscosity is $1.1 \cdot 10^{-6}\,\mathrm{m}^2 s^{-1}$, close to that of water ([42]). Refractive index matching is sensitive to small variations in salt concentration, and must be carefully adjusted. During PIV measurement, the test loop is pressurized to 15 *psi* in order to avoid cavitation.

Fig. 2.36 shows the actual test condition over the head / efficiency graph; measurements at a flow rate slightly larger than the best efficiency condition, at 900 rpm.

2.7.3 PIV Setup

The laser sheet illuminates the vertical meridional plane of the pump through the top flat surface; the meridional section of the rotor is shown in Fig. 2.38. Preliminary flow visualization experiments relying on cavitation ([62]) have indicated that the TLV develops inside the rotor along a $\sim 9^\circ$ pitch angle helicoid. Thus the meridional plane provides a good perspective on the cross section of the vortex. The interrogation area is wide enough to cover the passage between two blades, so at least one blade is present in every flow map upstream of the blade trailing edge. For the purpose of analyzing the vortex behavior the upper half of the sampled area is processed, i.e. a $40 \times 20\,\mathrm{mm}^2$ section, that includes the blade tip and tip gap. The light source is a 532 nm wavelength, 50 mJ/pulse, Nd:YAG laser, and the time interval between exposures is 30 µs. Images are recorded by a 2048×2048 pixels, interline transfer CCD camera equipped with a 105 mm lens. Consequently, the characteristic particle displacement between exposures is about 25% of the side length of the PIV cross correlation interrogation window.

The rotor phase is detected by an encoder installed on the shaft. The desired delay between the reference signal and image acquisition is set by a pulse generator, which also synchronizes the laser with the camera. The flow has been investigated in a total of 25 meridional planes, evenly spaced by $0.06c$, where c is the tip profile chord-length, including two sections preceding the leading edge and four located after the trailing edge of the blade. At least 1000 instantaneous realizations have been obtained in each plane.

2.7.4 Image processing and cross correlation

Because of a slight mismatch in the refractive index between the medium and the acrylic material, the blade and end-wall surfaces are visible in the images as thin lines, but no shadows or image distortions are noticeable. Along these thin lines, luminance can be misinterpreted by the cross correlation code; hence, blades and the end-wall line are carefully masked during post-processing by filtering the images with a top-hat filter, i.e. setting the intensity in the corrupted regions to zero.

The signal-to-noise ratio of the images is improved by removing dim background non-uniformities using a median-subtraction filter, followed by a Modified Histogram Equalization (MHE) algorithm ([63]). Before the cross correlation, image pairs are processed with a Gaussian filter in order to smooth luminance transitions at the boundary of particles, a useful technique when the cross correlation algorithm is based on Fast Fourier Transforms. Then, image pairs are sent to a multi-pass, FFT-based cross correlation routine (Davis© LaVision Inc.), with a final interrogation area of 32×32 pixel and 50% overlap, which generate a 128×128 vector map. For the present study, only the upper-half of the images are analyzed, giving 128×64 vectors, with vector spacing of 0.34 mm, i.e. $1.3 \cdot 10^{-3}c$. Several criteria are used for evaluating the data quality including relative magnitude of correlation peaks. About 97% of the vectors satisfy these criteria, and the rest are linearly interpolated based on values in neighboring correlation windows.

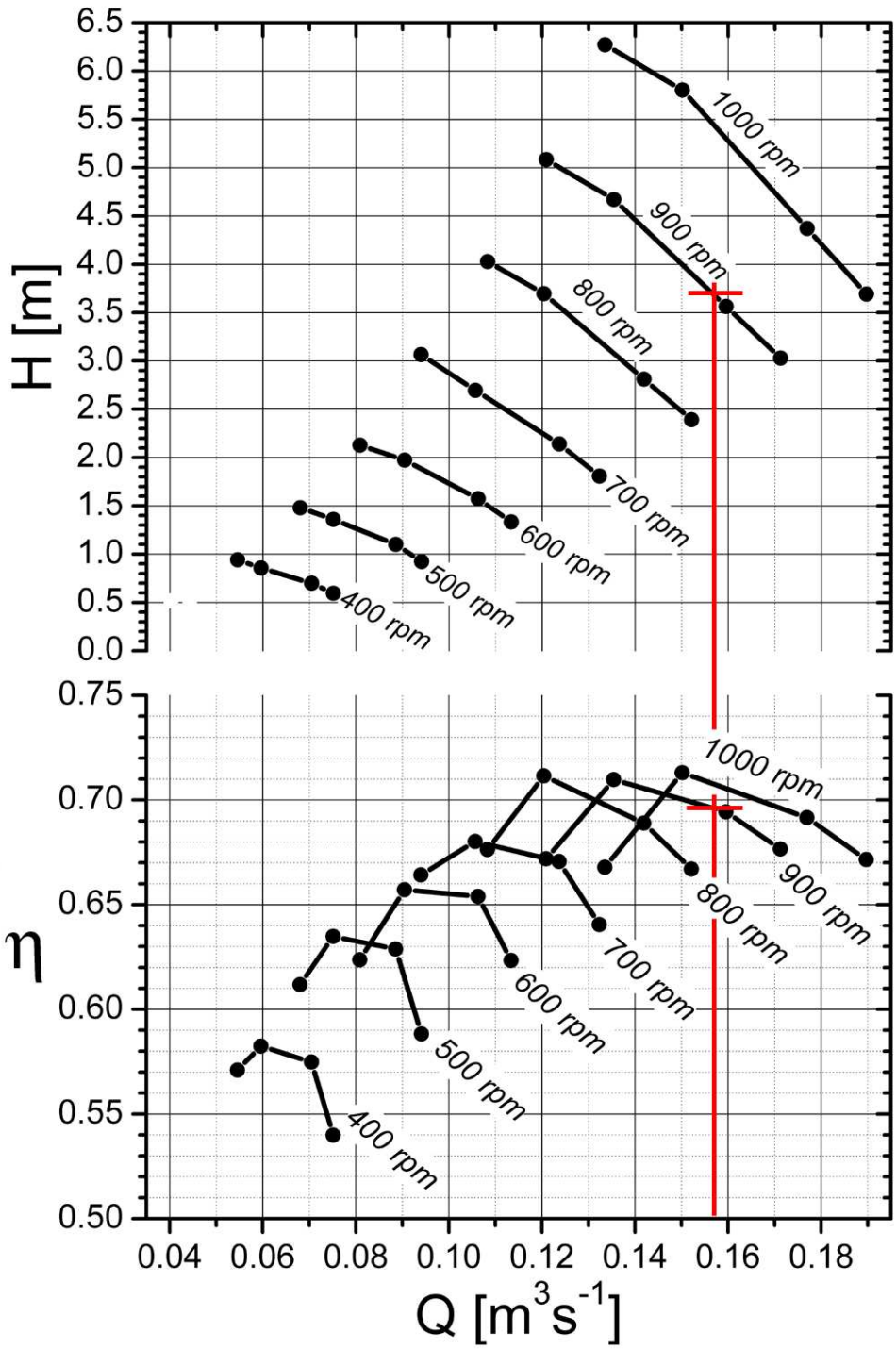

Figure 2.36: **Performance curves for the tested pump, the actual test condition is marked with a solid red line [JHU]**

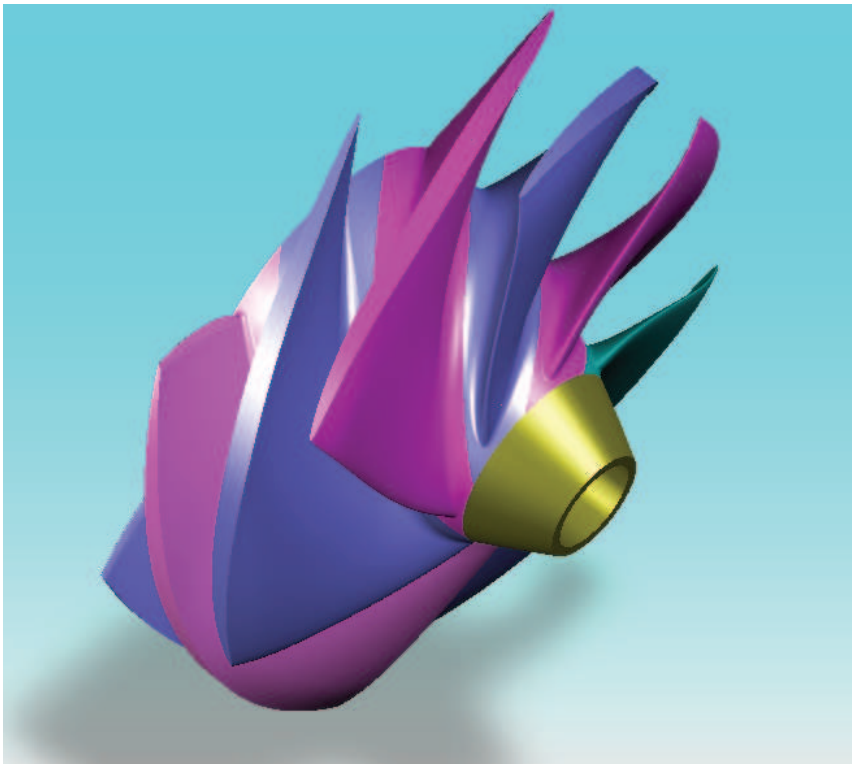

Figure 2.37: **Perspective view of the rotor [JHU]**

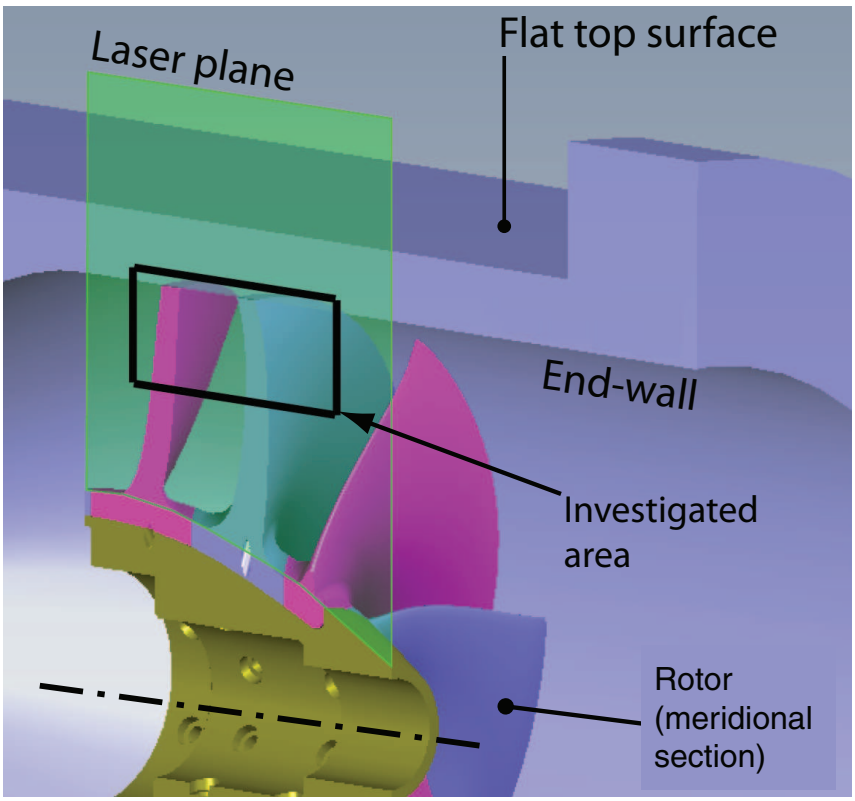

Figure 2.38: **Meridional plane of the pump and area investigated by 2DPIV [JHU]**

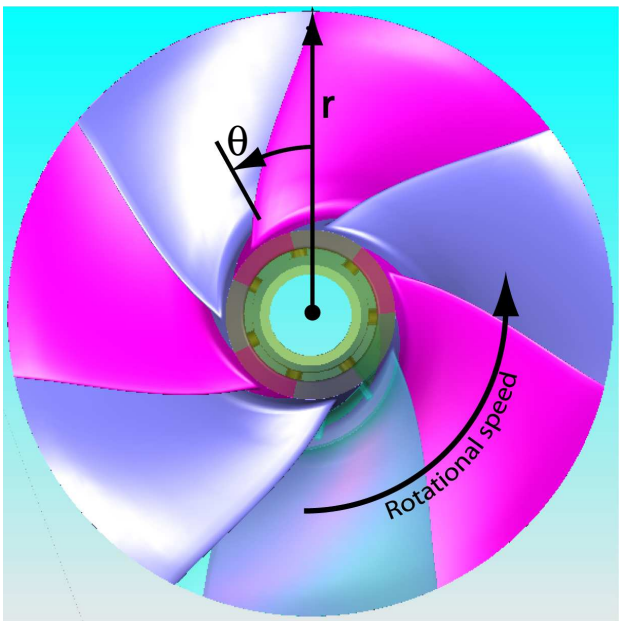

Figure 2.39: **Front view of the water-jet rotor [JHU]**

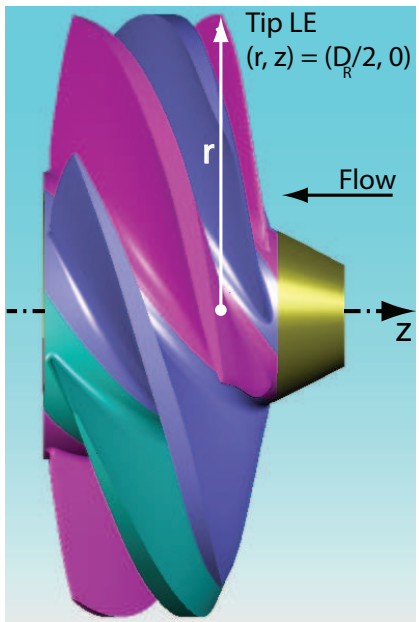

Figure 2.40: **Side view of the water-jet rotor [JHU]**

2.8 Data Processing

2.8.1 Frames of Reference

The flow is described using two frames of reference, the first is 3D-cylindrical and it is used to describe the overall geometry of the rotor, the second is localized at the tip of the blade. Fig. 2.39 and Fig. 2.40 show the overall frame of reference, the radius if normalized with the casing radius, the phase is set positive counter-clockwise like the rotational speed of the shaft and the z-axis points opposite the flow; as a result, the axial inflow component is negative. The origin of the frame is located on the rotational axis ($r = 0$), at the projection of the tip leading edge ($z = 0$), see Fig. 2.40.

The second frame of reference is intrinsic with the centerline of the tip profile,$sc^{-}1 = 0$ is the leading edge of the profile, $sc^{-1} = 1$ is the trailing edge. Because the blade rotates in the casing while the laser plane is fixed, the meridional velocity is sampled at different chord fractions sc^{-1}, see Fig. 2.38.

2.8.2 Scaling

The first investigations on the TLV were performed on linear cascades, with fixed end-wall, where the pressure difference across the tip profile was measured with pressure taps. The measurement of the pressure difference, which is a result of the overall lift of the blade, allows a generale similitude analysis to be set, for instance, by Tan ([64]).

In Tan's model, the characteristic velocity is derived from the pressure difference$\sim (\Delta p)^{0.5}$ with an inviscid theory. Moreover, Tan's model was developed on compressor blades where *i)* the ratio between the tip gap width and the maximum blade thickness is relatively low and mixing phenomena due to the gap back flow occur outside the gap, i.e. in the passage, hence the inviscid model is justified; *ii)* the ratio between the chord length of the tip profile and the casing diameter at the stage section is very low, and the curvature in the gap can be neglected describing it with Cartesian coordinate.

There are three reasons why the classic similitude model *cannot be adopted* in the

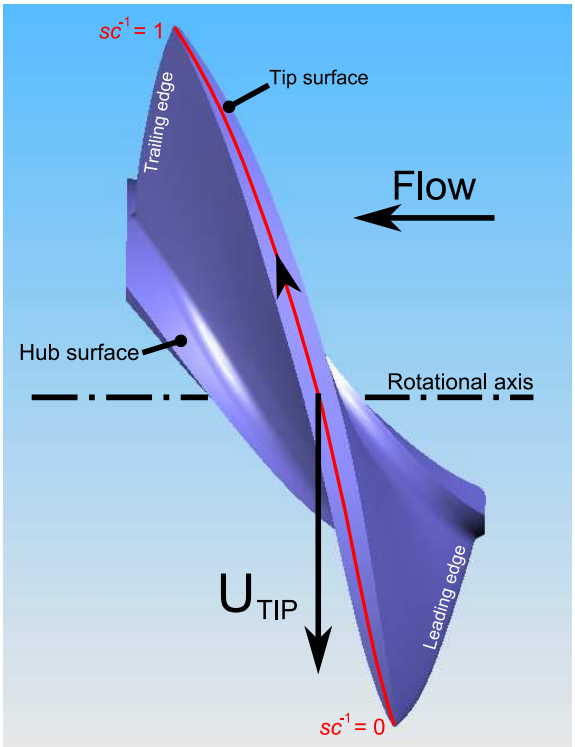

Figure 2.41: **Blade tip intrinsic frame of reference [JHU]**

pump under investigation:

1. because of the elevated stagger angle ($\approx 25°$ from the tangential direction) the tip surface is directed almost circumferentially, and the curvature of the tip clearance cannot be neglected;

2. because of the large ratio between the tip chord length and the casing circumference (≈ 0.25), Euler equations for the incompressible flow ($\rho = 1$) in the clearance must be written in cylindrical coordinates (r, θ, z); as the ratio between gap width and the rotor radius is very low ($\approx 1 : 151$) the curvature term $c(r) = 1/r$ can be replaced with the (constant) clearance curvature $C = 2/D \approx 6.56\,\mathrm{m}^{-1}$, Euler equation are:

$$u_\mathrm{r}\frac{\partial u_\mathrm{r}}{\partial r} + Cu_\theta\frac{\partial u_\mathrm{r}}{\partial \theta} + u_\mathrm{z}\frac{\partial u_\mathrm{r}}{\partial z} - Cu_\theta^2 = -\frac{\partial p}{\partial r} \tag{2.16}$$

$$u_\mathrm{r}\frac{\partial u_\theta}{\partial r} + Cu_\theta\frac{\partial u_\theta}{\partial \theta} + u_\mathrm{z}\frac{\partial u_\theta}{\partial z} + Cu_\mathrm{r}u_\theta = -C\frac{\partial p}{\partial \theta} \tag{2.17}$$

$$u_\mathrm{r}\frac{\partial u_\mathrm{z}}{\partial r} + Cu_\theta\frac{\partial u_\mathrm{z}}{\partial \theta} + u_\mathrm{z}\frac{\partial u_\mathrm{z}}{\partial z} = \frac{\partial p}{\partial \theta} \tag{2.18}$$

   the term $u_\mathrm{r}\frac{\partial u_\mathrm{r}}{\partial r} \approx 0$, but others cannot be neglected *a priori*;

3. in particular, terms containing the clearance curvature $C = 2/D$ cannot be neglected, the term $Cu_\theta\partial_\theta u_\mathrm{z}$ indicates that the circumferential velocity u_θ dominated by the condition $u_\theta = U_\mathrm{TIP}$ at the tip surface has influence on the axial pressure gradient also because of the large curvature, i.e. the scaling parameters adopted in Tan's model also depends on a velocity component that the 2DPIV in the meridional plane cannot measure.

In conclusion, the relationship between the pressure gradient across the tip profile and the flow in the clearance is not straightforward, and involves velocity components that are

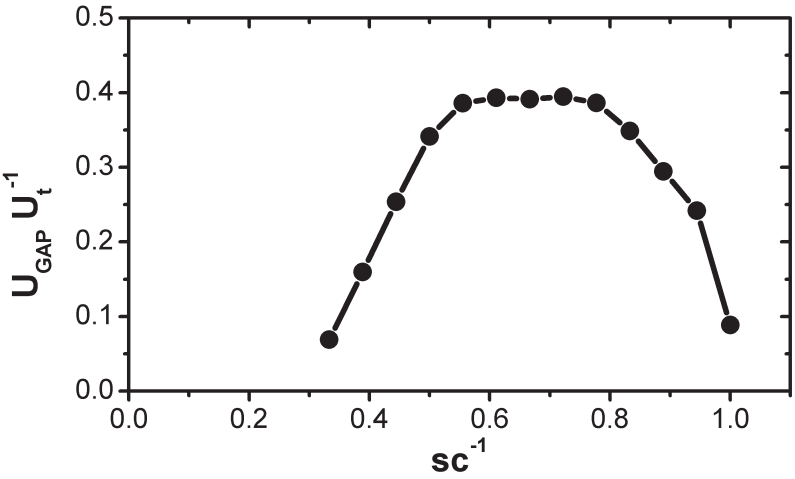

Figure 2.42: **Chord-wise distribution of the tip leakage flow velocity, normalized with the tip speed; the chord-wise average is** $0.3\,U_{\mathrm{TIP}} \approx 4.5\,\mathrm{ms}^{-1}$ **[JHU]**

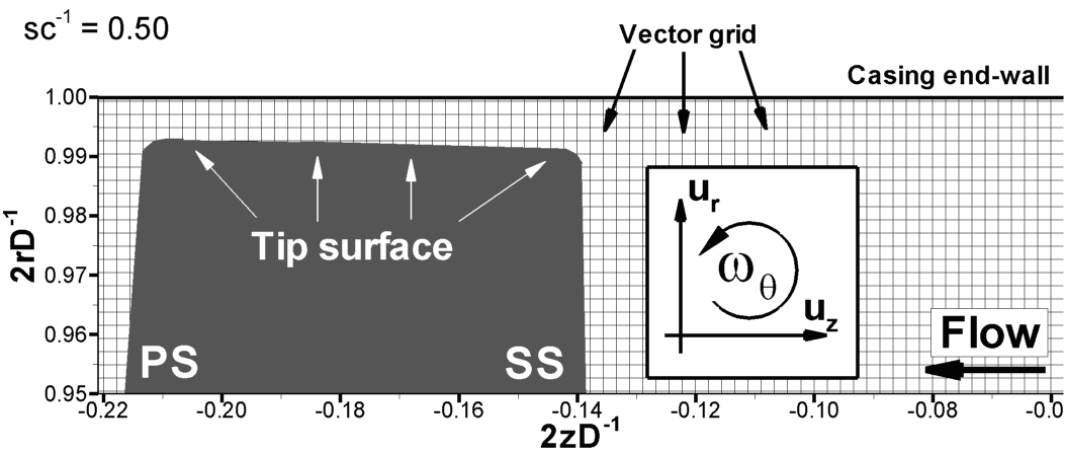

Figure 2.43: **Vector grid and conventional directions for the description of geometry, velocity and vorticity [JHU]**

unknown. In order to normalize results, the gap flow is decomposed into a circumferential component, dominated by the tip speed, and an axial component, that can be measured with 2DPIV in the meridional plane. Processing the 2DPIV data in the meridional plane, computations not shown, it is possible to state that a characteristic axial velocity in the clearance is $U_{\mathrm{GAP}} \approx 4.5\,\mathrm{ms}^{-1}$, i.e. $U_{\mathrm{GAP}} \approx 0.3\,U_{\mathrm{TIP}}$, see Fig. 2.42; hence the dominant velocity in the clearance is the tip speed $U_{\mathrm{TIP}} = 14.3\,\mathrm{ms}^{-1}$ and the characteristic scale is the gap width $h = 0.001\,\mathrm{m}$; the reference velocity gradient is $U_{\mathrm{TIP}}\,h^{-1} = 14300\,s^{-1}$.

Fig. 2.43 shows the frame adopted for presenting the results; in the meridional plane, the blade section is visible and shifts right to left[6]. In the background, the vector grid is spaced 0.3 mm and the reference for the velocity and vorticity components are shown. Axes are normalized with the casing diameter at the rotor, velocity components are normalized with U_{TIP} and the out of plane (circumferential) vorticity component is normalized with the reference velocity gradient $U_{\mathrm{TIP}}\,h^{-1}$. The axial component of the flow is positive

[6]it is an apparent displacement and the rotor velocity is always circumferential, i.e. out of plane

opposite the flow, i.e. the axial component of the passage flow velocity is negative and the axial component of the tip clearance backflow is positive.

2.9 Instantaneous Flow

Fig. 2.44 shows an instantaneous snapshot of the TLV meridional section, at mid-chord. The refractive index matching of the blade, casing and fluid allowed the image to be very high quality; moreover, additional image processing and a careful setup of the cross-correlation parameter have allowed the computation of reliable instantaneous vector fields.Obtaining such detailed results with a point-to-point device such as a probe or LDV is impossible.

Although the vector field is quite *noisy*, structures around the TLV are visible. In order to improve the visualization of these structures, the data in Fig. 2.44 have been box-filtered (3×3). The box filter is the most basic large eddy filter, it is a low-pass filter in space with a characteristic size of 3δ.

The filtered vector field is computed applying the general formula

$$\alpha(i,j) = \sum_k \frac{\tilde{\alpha}(i+k, j+k)\delta^2}{(3\delta)^2}, \qquad k = -1,\, 0,\, 1 \tag{2.19}$$

where α is the generic filtered quantity, α can be each of the velocity component or the vorticity, and (i, j) define location on the grid. Because the box filter causes a loss of signal even at low wave numbers, smoothing is only applied for the purpose of identifying flow structures at the final stage of analysis, and is not used prior to computing turbulent variables.

The original PIV velocity field is already a spatially low-pass filtered information. Recalling that the sampling function is a space-distributed, discrete pattern of rectangular impulses $rect(i\delta, j\delta)$ of wave number $\lambda = \delta^{-1}$, it can be stated that the cut wave number of such a sampling function *is not* λ. In fact, the 2D-PIV map can be though as a convolution of the velocity of the fluid with the optics transfer function and the sampling function, i.e. the rectangular impulses. The correspondent function of the rectangular impulse in the frequency domain is the function $sinc(\lambda, \lambda)$, which cuts the signal abruptly because its first lobe decays quickly, e.g. $sinc(0.75) = 0.3$. As a result, the cut wave number is much lower than the sampling wave number.

This feature and the bounded PIV domain lead to large difficulties in computing reasonable spatial spectra of the PIV data[7]. The box filter a further low pass filter and, following the previous reasoning, it can be stated that the cutting wave number of the box filtered data is less than $(3\delta)^{-1}$.

The analysis of the instantaneous, filtered data of Fig. 2.45 allows the TLV to be recognized, with some secondary structures that will be described later in the text. Specifically, the TLV is not the sole vortical structure present, also a counter-rotating vortex (*scraping vortex*) is located between the casing and the upstream front of the TLV, indicated by point B in Fig. 2.45.

Structures are revealed by the analysis of the instantaneous out of plane vorticity. Because the velocity field is not frame invariant, recognizing vortices with streamlines or directly from the vector field is not correct. Vorticity contours and velocity distributions are in agreement but,in fact, not perfectly coincident. Indeed, the transport velocity of both the TLV and the secondary vortices are much lower than the induced velocity in their outer branches and this leads to a visible correlation between vorticity and velocity structures; nevertheless, the peak of vorticity and the center of the vortical vectors displacement are slightly offset, as shown in Fig. 2.46 (d). The vortex centerline passes through the peak of vorticity.

[7]in fact, for example, the so-called sub-grid stresses (large eddy approximation) can be computed experimentally from PIV only post-processing the data with the box filter or the Gaussian filter, not with the spectral filter

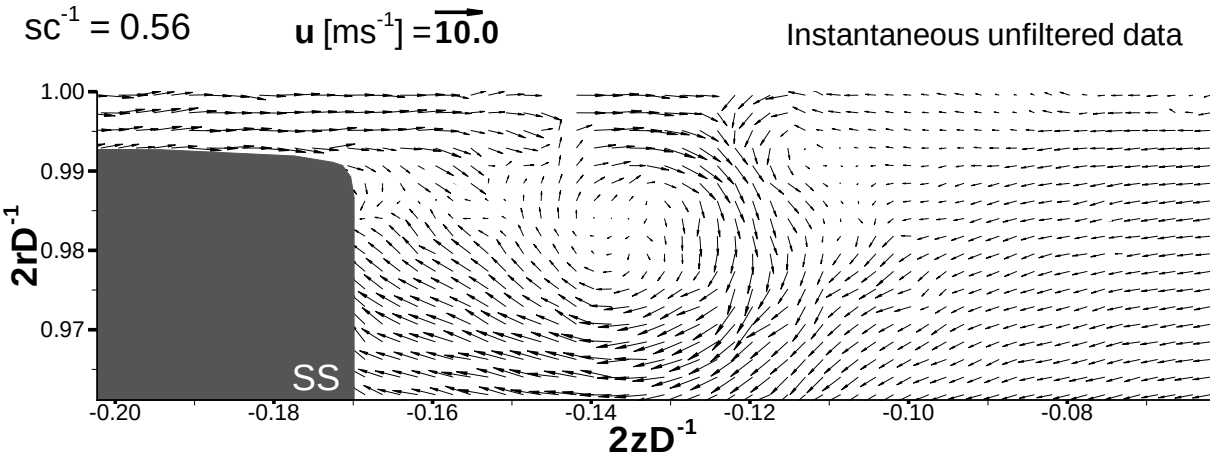

Figure 2.44: **Instantaneous snapshot of the TLV**

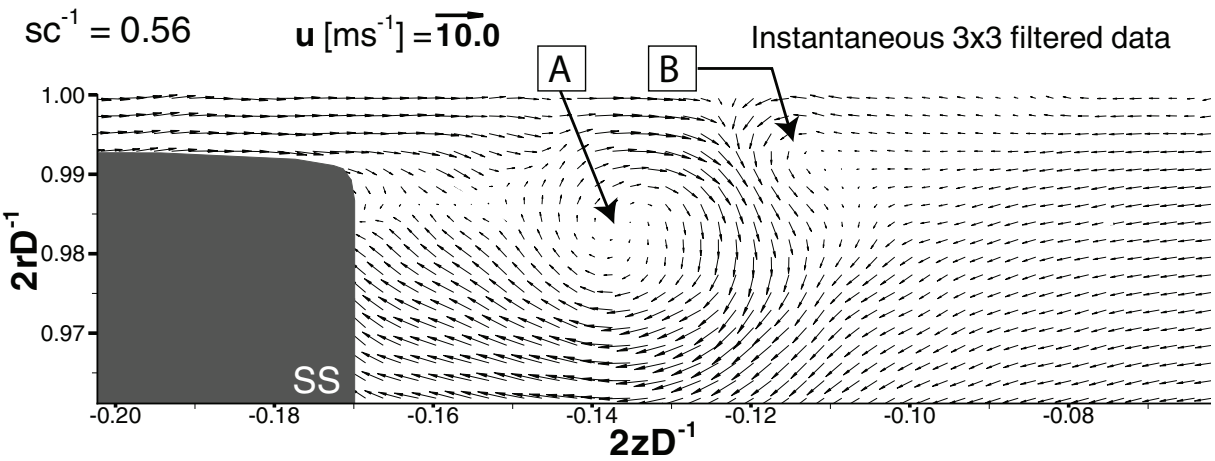

Figure 2.45: **The instantaneous snapshot of Fig. 2.44, after the 3x3 box filter, [A] the tip leakage vortex, [B] the counter rotating secondary vortex (*scraping vortex*)**

Fig. 2.46 shows the box filtered vorticity computed from the unfiltered velocity at various chord fractions; the sequence of plots describes the evolution of the TLV cross section as the vortex passes through the meridional plane. It is important to recall that data is phase locked but it is not time resolved; hence the vorticity distributions belong to different TLV's and indicate the typical evolution of the phenomenon, not the actual evolution of one vortex.

Fig. 2.46 (a) shows the TLV inception, the remnants of the burst TLV in the previous rotor passage are noticeable on the left of the blade section, as a cloud of scattered vorticity, i.e. the phenomenon is cyclic; the TLV rolls up ingesting the vorticity that sheds from the suction edge.

In Fig. 2.46 (b) the TLV develops as a set of coherent structures; the analysis of 1000 instantaneous realizations at $sc^{-1} = 0.56$, leads to the conclusion that the TLV is the result of the wrapping around of vortex filaments, whose sections are noticeable, and these structure never merge because the time scale of the transport of the TLV towards the following blade is much lower than the time scale of the vortices interaction due to turbulent mixing or merging. The gap flow interacts with the casing surface $2rD^{-1} = 1.00$ inducing visible boundary layer vorticity. The resolution of the measurements is insufficient to resolve this boundary layer, which is thin due to the steep acceleration of

the flow in the gap; nevertheless, there is a row of nodes in the vector grid that is very close to the casing, see Fig. 2.41, thus the radial gradient of the velocity is appreciable at least in that zone. As the tip clearance back-flow jet stops due to the collision with the passage flow, a "stagnation" region induces the detachment of the casing vorticity that arranges into vortices. No boundary layer vorticity is noticeable over the tip surface. The absence of out of plane vorticity is not due to spatial under-sampling, circumferential vorticity is actually absent there, i.e. the tip surface vorticity vector is entirely in-plane and invisible. Later in the text, the mechanism of formation of the TLV will be described in detail by means of phase averaged vorticity maps.

The TLV described at $0.83c$, is large enough to show inner details, see Fig. 2.46. The flow overturns clock-wisely from the pressure side to the tip clearance entry section inducing a localized vorticity peak. The tip surface vorticity accumulates and sheds from the suction surface as a rake of vortex ropes, the figure shows the sections of these ropes. Vortical structures are convected by the tip clearance back-flow but, as the clearance jet slows down and stops, they are wrapped into the TLV without merging.

As vortices shed by the suction edge move inside the passage, they induce counter-rotating vorticity at the casing, the casing vorticity proceeds along the solid wall, it detaches from the wall and it is convected around the TLV. Eventually, it starts interacting with the negative vorticity already present in the TLV but, again, there is no time for the interaction and the structure remain divided until the vortex bursts.

Fig. 2.46 (d) illustrates the structure of the TLV at the chord section in which preliminary tip vortex cavitation visualizations, not shown in this work, showed the TLV bursting. Casing end wall vorticity is distributed inside the TLV where vortices of both sign can be found. The rake of parallel vortices shed by the blade are clearly visible, as well as the counter-rotating vorticity that peaks at the "stagnation" region before being convected away.

After the bursting, see Fig. 2.46 (e), there is no organized structure and the outer part of the passage, in the vicinity of the pressure side of the following blade, is filled with scattered vorticity of both signs. The rake of vortex ropes shed by the suction edge of the blade must end at the trailing edge, where the abrupt variation in the geometry induces a concentration of vorticity sources that lock on the edge. As a result, the very last vortex ropes roll up into a second vortex, at the end of the vortex sheet. This last vortex does not interact with the following blade and it is likely discharged towards the stator.

It is important to highlight the data in Fig. 2.47, i.e. the vorticity map of Fig. 2.46 (e) with the superimposition of velocity vectors, diluted for clarity. Even though there is no blade, and no pressure difference feeds the tip leakage flow, a recirculating flow is noticeable at the casing.

Fig. 2.48 (a) to (e) show the normalized in-plane strain-rate magnitude. At a $0.44c$, Fig. 2.48 (a), a scattered strain-rate field on the left of the blade section is noticeable. Peaks located on the left of the figure belong to the previous TLV remnants except one, located just underneath the pressure edge of the blade section; that is the instantaneous stagnation point that divides the flow migrating upwards to enter the gap from the flow pushed downward by the displacement action of the blade and the interaction with the burst TLV.

Strain-rate peaks in Fig. 2.48 (b) and (c) can be related to vortex-vortex interactions, of the shear type, in the vortex sheet connecting the TLV with the blade (point A) and to the instantaneous "stagnation" region is which the back-flow clearance jet collides with the passage flow.

Fig. 2.48 (d) and (e) illustrate the strain-rate distribution of the burst vortex, peaks are noticeable in the vortex-vortex interaction zones, the flow gains substantial isotropy due to the bursting and is delivered to the stator.

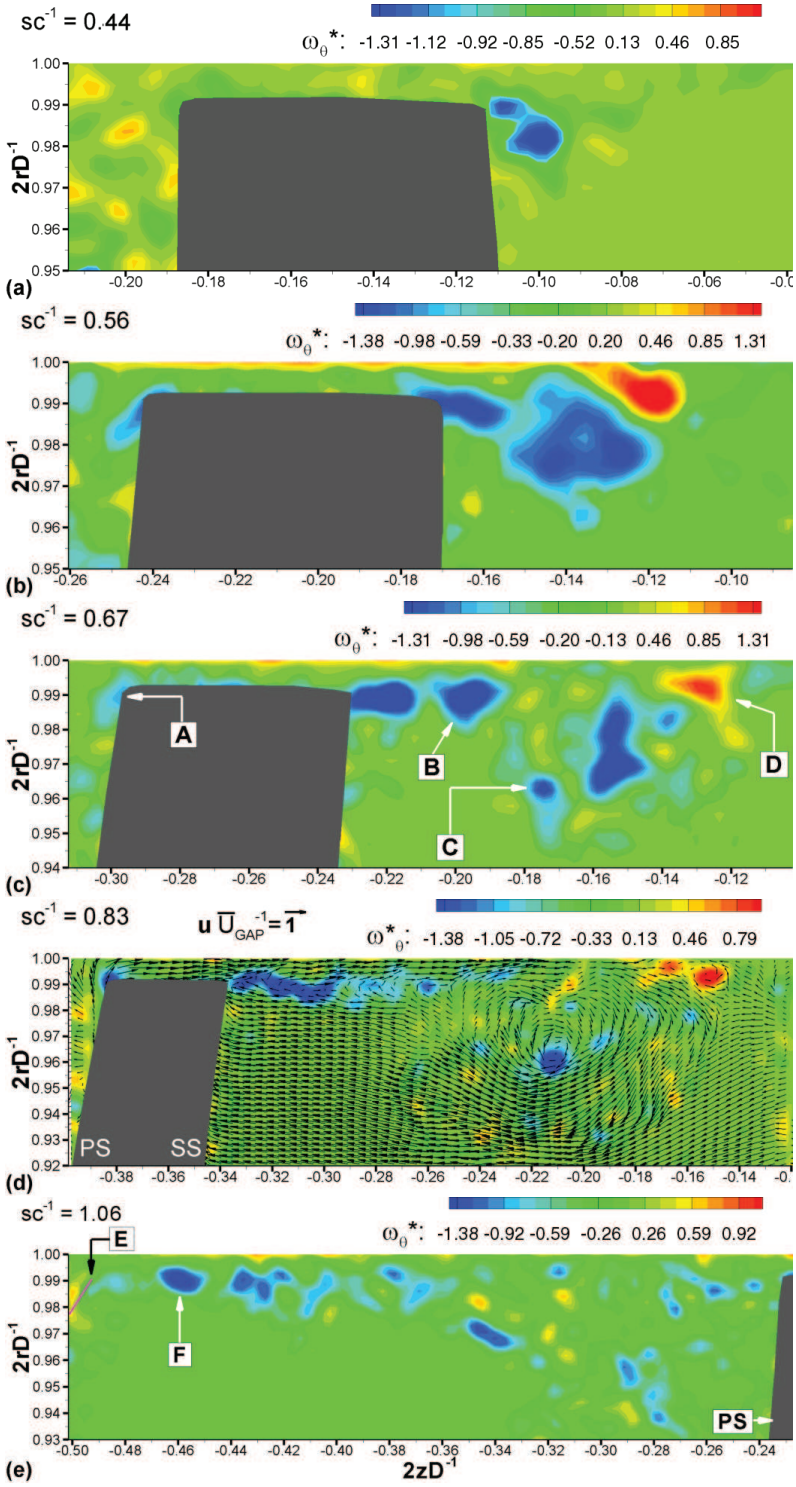

Figure 2.46: **Instantaneous box filtered vorticity at different, increasing chord-fractions; A: overturning at the gap inflow, B: vortex ropes shed by the blade, C: vortex ropes wrapped into the TLV, D: secondary vortices shed by the casing and entrained into the TLV perimeter, E: centerline of the meridional section of the wake, F: roll up of vorticity shed by the tip trailing edge; velocity vectors are diluted for clarity and plotted in arbitrary scale to visualize the flow**

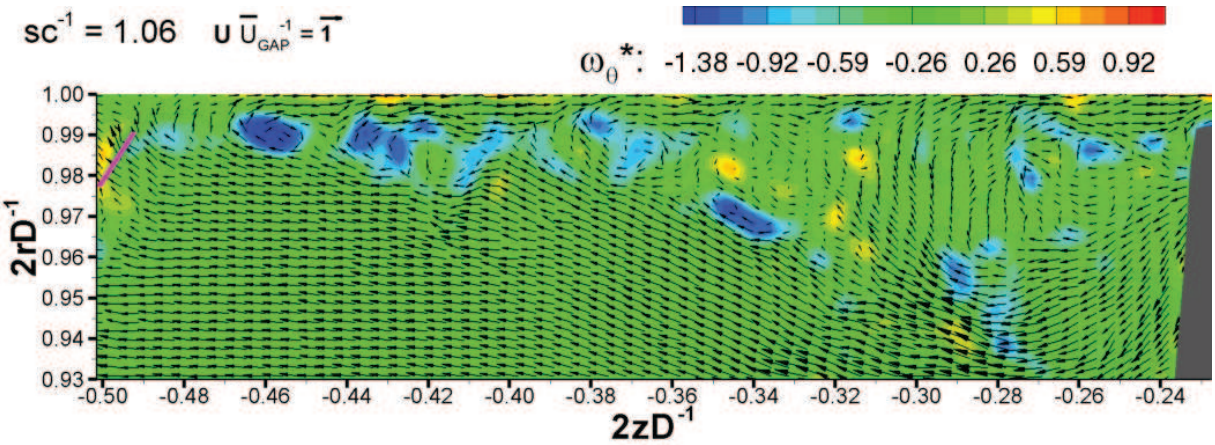

Figure 2.47: **The instantaneous snapshot of Fig. 2.46 (e), with the superimposition of the velocity; velocity vectors are diluted for clarity and plotted in arbitrary scale to visualize the flow**

2.10 Phase Averaged Flow

The back-flow in the tip clearance starts at chord-fractions $sc^{-1} \simeq 0.33$ as shown in Fig. 2.42 because the static pressure distribution at the leading edge of the tip profile is likely inverted and the gap flow is actually a forward flow at $sc^{-1} < 0.33$, not shown[8].

The inception of the TLV is shown in Fig. 2.50 (a) where the phase averaged vorticity ($sc^{-1} = 0.33$) is superimposed to the phase averaged velocity. The velocity in the gap is almost null because at this chord fraction the static pressure at the sides is nearly zero. Nevertheless the flow at the pressure edge turns cockwisely to enter the gap inducing a vorticity peak, at point A.

A proposed mechanism for the out of plane vorticity generation at the pressure side edge is illustrated in Fig. 2.49. The PS boundary layer contains vorticity that is approximately radial; because of the tip clearance suction effect, streamlines are bent radially convecting the boundary layer also radially, the turning of the streamlines is a very sudden effect, very localized at the tip and it induces a circumferential orientation of the vorticity.

Point B in Fig. 2.50 (a) indicates the initial roll up of the TLV. The boundary layer developed on the blade tip surface is not visible because it is in plane; in fact, the boundary condition at the tip surface is $\mathbf{u} = (D_{\mathrm{R}}/2)\,\Omega\,\mathbf{e}_\theta$ where $\mathbf{e}_\theta$ is the circumferential unit vector. Such a boundary condition generates a boundary layer that develops in the pump cross-section plane, and hence an axial vorticity that is not visible in the meridional plane.

The jet emerging from the tip clearance penetrates the passage flow generating a layer of strong velocity gradient, the circumferential vorticity ω_θ rolls up there and detaches from the blade forming a vortex filament. Vortex filaments roll up into the TLV that is bent by the passage flow that pushes the interlaced filaments downstream while the next blade moves towards the vortex[9]. As a result, the TLV develops in the passage with a pitch angle of $\approx 9°$ respect with the circumferential direction.

A closer look to Fig. 2.50 (a), point B, also reveals that the TLV has a "drop" shape, that feature can be explained as an interaction between a very high spin vortex and the suction side wall. The intense clock-wise rotating TLV develops very close the blade, a

[8]this is the first prototype for this pump, the pressure distribution has been corrected in the second prototype

[9]as seen in preliminary vortex visualizations, not shown

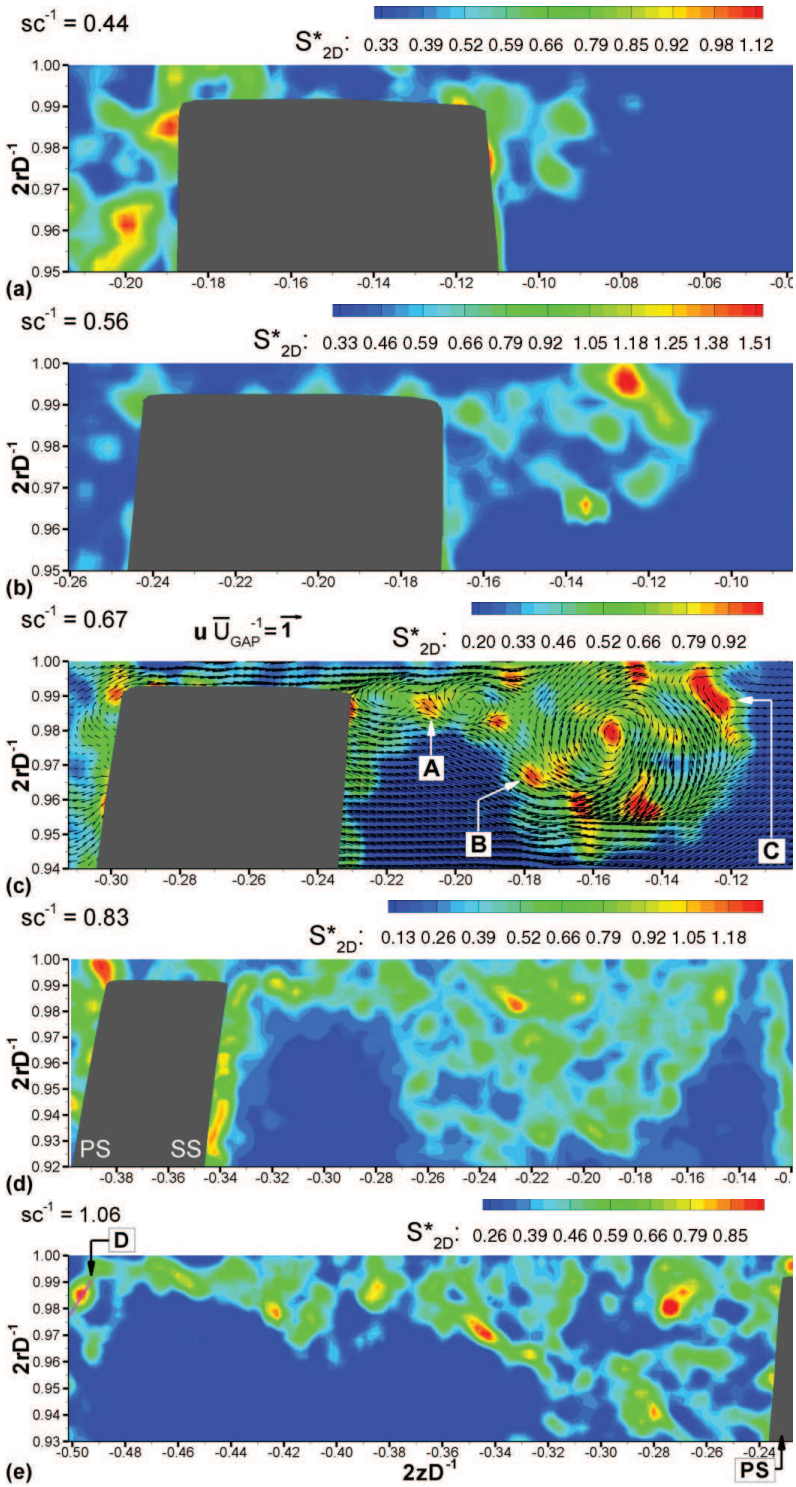

Figure 2.48: **Instantaneous box filtered strain-rate magnitude at different, increasing chord-fractions; A: shear interaction between co-rotating vortices, B: interaction between vortex ropes wrapped into the TLV, C: strained flow due to the leakage jet interaction, D: strained flow in the wake; velocity vectors are diluted for clarity and plotted in arbitrary scale to visualize the flow**

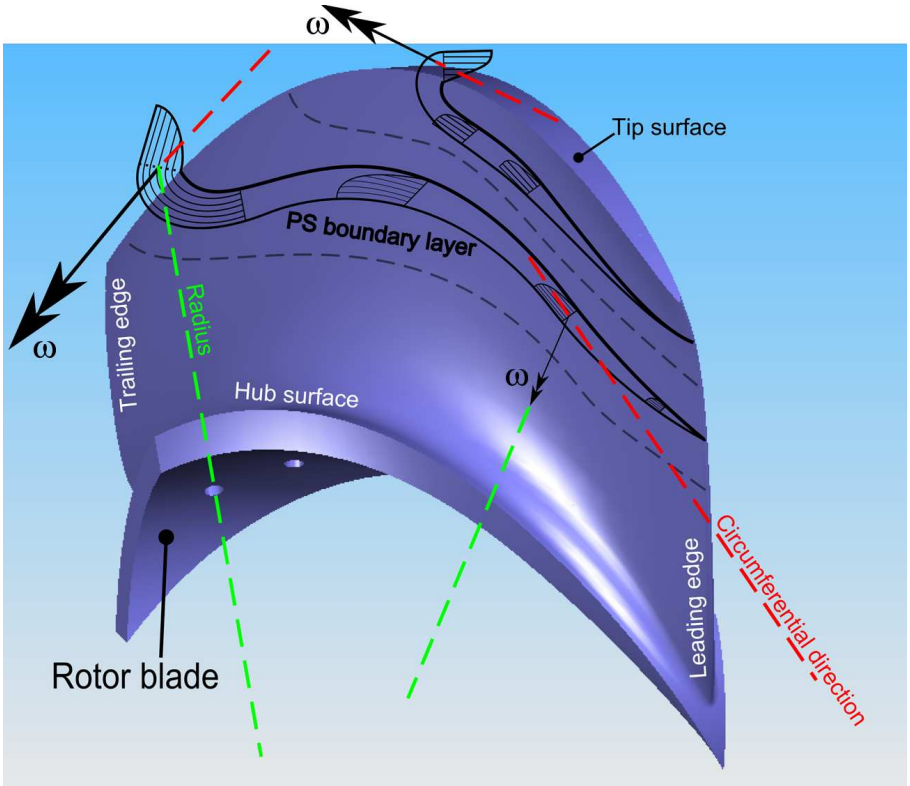

Figure 2.49: **Illustration of the out of plane vorticity generation at the pressure side edge of the blade**

wall effect is expected, which can be described by means of the image vortex theory. The image vortex of the TLV is located inside the blade section, along the line perpendicular to the surface and passing through the TLV center, at the same distance from the surface. The image vortex is rotating counter-clock wise with the same circulation magnitude. As a result, the induced motion is radial towards the tip of the blade but inhibited by the tip leakage jet and the TLV is locked in that position. It is known from the image vortex theory that the induced velocity, in this case the locking effect, is proportional to the vortex circulation and inversely proportional to the distance from the wall. The image vortex concept will be drawn on later in §2.11 to describe the motion of the TLV in the passage.

A comparison between Fig. 2.50 (a) and (b) shows that within a short interval, less than 20% of the chord, i.e. $\simeq 3.6\,\mathrm{ms}$, the casing vorticity upstream the blade section changes from $\omega_\theta^* \simeq -0.4$ to $\omega_\theta^* \simeq +0.4$ with a total inversion of the strength. The TLV is detached from the blade and connected to it by a vorticity layer. The same layer is clearly noticeable in Fig. 2.50 (c), where the TLV is far from the blade and the core is travelling in the passage.

Taking a look back to Fig. 2.46 it is possible to justify the presence of a vortex layer there. In fact, the phase averaged data contain flow structures that must be analyzed carefully. Given the rotor phase, the position of the blade section is set in the frame; the phase averaged TLV originates at the same inception point at every round of the rotor and develops with the same averaged characteristic time because the averaged clearance flow has the same chord-wise distribution for the same blade at each round, see Fig. 2.42.

As a result, the position of the TLV and the scraping vortex are unsteady and oscillate around an average point. This average between 1000 instantaneous samplings converges, at least at the first stages of the TLV evolution; for this reason, the phase averaged vorticity shows one clear TLV and one clear point of detachment of the casing vorticity.

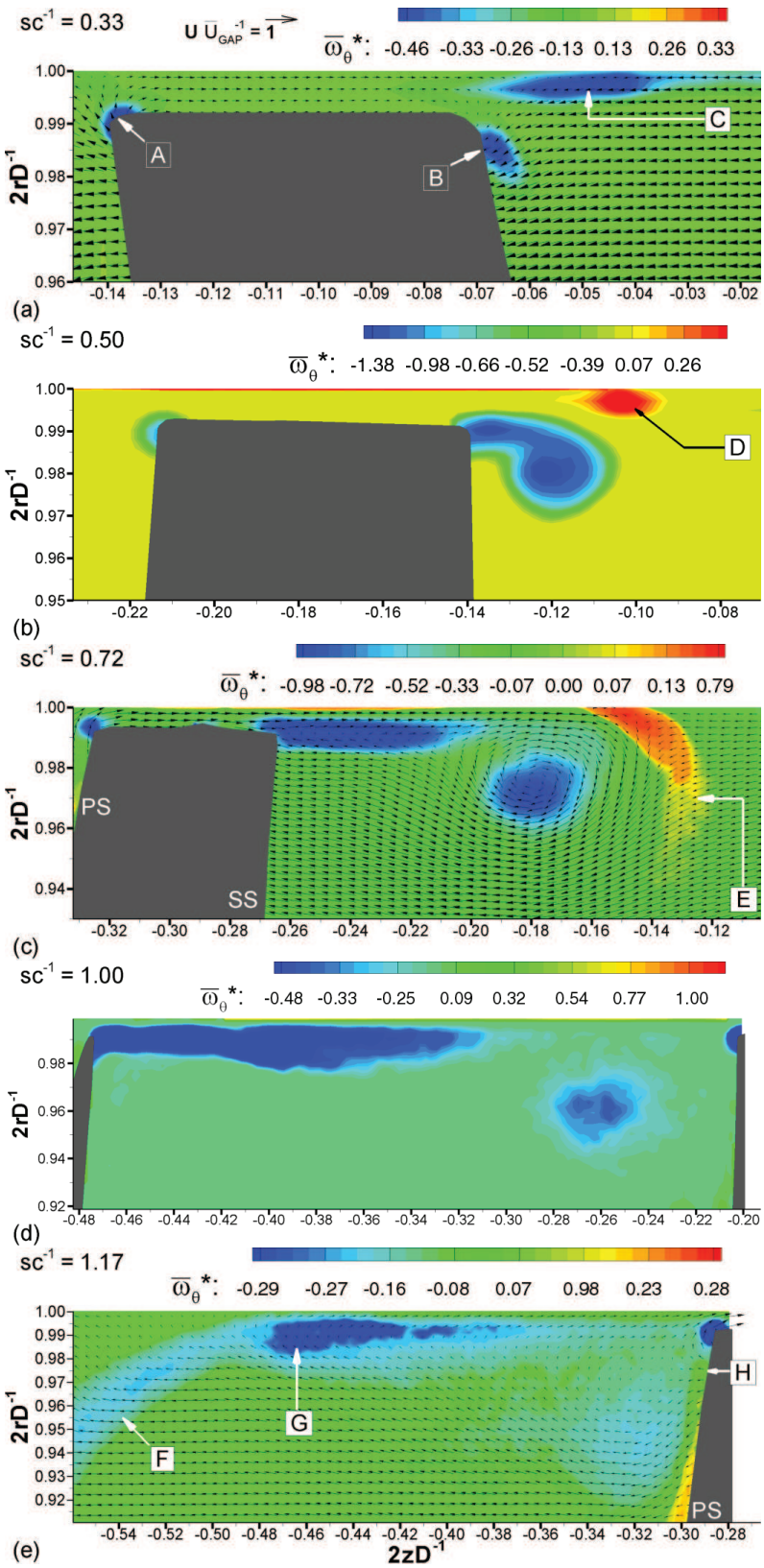

Figure 2.50: Phase averaged out of plane vorticity at different, increasing chord-fractions; A: overturn of the flow, B: TLV inception, C: blockage of the casing boundary layer, D: reversed vorticity at the casing, E: secondary vorticity entrained into the TLV front, F: wake circumferential vorticity, G: roll up of vorticity shed by the tip trailing edge, H: diverging streamline flow; velocity vectors are diluted for clarity and plotted in arbitrary scale to visualize the flow

The situation is very different in the vorticity layer and in the front of interaction between the TLV and the passage flow, this phenomenon will be also drawn on later in the text as it is determinant for the evaluation of turbulence in the TLV. In fact, the vorticity layer and the front of interaction zones are the result of travelling single vortices, visible in Fig. 2.46, whose dynamic depends on the rotor phase, but not exclusively. Hence, vortices are shed from the suction edge and from the blade, but their transport has little correlation with the rotor phase, i.e. they are not synchronous with the blade. The phase averaged of asynchronous vorticity created a straight vortex sheet at the suction edge, and a semicircular vortex sheet in the TLV front.

Fig. 2.50 (d) illustrates the phase averaged TLV in the meridional plane that passes through the trailing edge of the blade. In the following, the circulation of the phase averaged velocity will be shown to be approximately constant in this range of chord-fractions, even though the averaged TLV is very dimmer. This behavior is due to the spreading of vorticity in every direction. Before bursting, the TLV convective instability causes the vortex centerline to bend approximately as a helicoid, i.e. keeping a coherent structure; after the bursting, the structure of the vortex becomes disordered and the phase averaged vorticity does not converge to a smooth distribution.[10].

The TLV shown in Fig. 2.50 (e) is very dim because its average do not converge and because the bursting process generates isotropy in the flow. Before the bursting, the TLV flow is obviously anisotropic as the structure has a clear cylindrical structure; the major part of the TLV vorticity is oriented circumferentially, out of plane, and the strength of the vortex can be tracked in the meridian plane, see §2.12. The bursting process destroys the coherence of the TLV and the alignment of its vorticity, the chaotic cloud of vortices redistributes vorticity on every possible direction; statistically speaking, this process alone diminishes the out of plane vorticity component by approximately 2/3. Although weak, the burst TLV is still able to generate vorticity of opposite sign by wall effect on the pressure side of the incoming blade, see the point "PS" in Fig. 2.50 (e). The vorticity region F is the result of the shedding of vortices along the trailing edge at lower spans, the schematics is shown in Fig. 2.51, where one blade of the rotor is removed for clarity. The rolling up of vorticity shed by the tip trailing edge, point G, induces a suction effect on the wake and clearly bends it. As a final remark, it is worth to observe that the flow at the casing is still reversed, as shown also in the instantaneous snapshot of Fig. 2.47.

2.11 Identification of the TLV

In order to track the path of the TLV center in the rotor passage, its center must be located in the phase averaged maps. The method adopted is called λ_2 and it involves the analysis of a function of the spatial derivatives of the velocity; as a result the ensemble average of λ_2 instantaneous distributions is equal to the λ_2 distribution in the averaged velocity map.

The λ_2 theory can be found in [65] and it will be briefly described in the following. Isolating vortex filaments in DNS data can be very difficult, especially in shear layers where vortices share the space with ribs and other non vortical coherent structures. The vorticity distribution can be too smooth to reveal vortex filaments and a sharper signal is

[10]the helicoidal shape of the unstable vortex has been observed in previous tip vortex cavitation visualizations. The helicoidal shape can be justified in terms of modal analysis, literature is vast in this field, because the generally the first unstable modes that a vortex encounters are the so-called "sausage" modes, i.e. an alternated inflating of the vortex cross section, and the "sinusoidal" mode in which the vortex centerline bends in a wavy fashion. Two sinusoidal modes of equal amplitude on perpendicular planes generate a helicoidal trajectory.

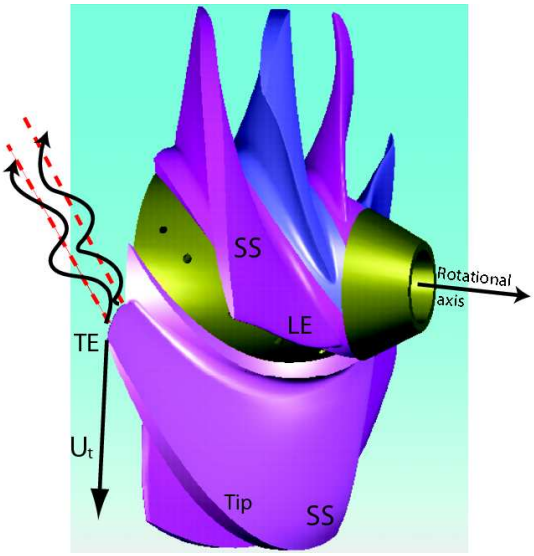

Figure 2.51: **Vorticity visible in Fig. 2.50 (e) at point F is shed spanwisely by the trailing edge of the blade**

often to be found. The attempt of locating the centerline of a vortex is obviously related to the issue of defining a vortex, unfortunately that issue is far from being closed at the time of this writing.

The identification of a vortex seem not be a problem of sole kinematics, it involves dynamics, hence the evaluation of the static pressure field; generally speaking, the centerline of a vortex is a locus of relative minimum for the static pressure. On the other hand, PIV does not provide the static pressure field, thus the tracking method must involve solely kinematics.

Assuming the flow incompressible with $\rho = 1$ the momentum equation is

$$\frac{\mathrm{D}u_i}{\mathrm{D}t} = -\frac{\partial p}{\partial x_i} + \nu \frac{\partial^2 u_i}{\partial x_k^2} \tag{2.20}$$

using the index notation for clarity, and denoting the material acceleration with a_i it is possible to write

$$a_i = -p_{,i} + \nu u_{i,kk} \tag{2.21}$$

where indices after comma denote spatial derivatives; the gradient of the equation is

$$a_{i,j} = -p_{,ji} + \nu u_{i,jkk} \ . \tag{2.22}$$

Because the static pressure is continuous, its spatial derivatives commute

$$a_{i,j} = -p_{,ij} + \nu u_{i,jkk} \tag{2.23}$$

the equation can divided into its symmetric and antisymmetric parts

$$\left(\frac{\mathrm{D}S_{ij}}{\mathrm{D}t} + S_{ik}S_{kj} + \Omega_{ik}\Omega_{kj}\right) + \left(\frac{\mathrm{D}\Omega_{ij}}{\mathrm{D}t} + \Omega_{ik}S_{kj} + S_{ik}\Omega_{kj}\right) = -p_{,ij} + \nu u_{i,j\,kk} \ . \tag{2.24}$$

The antisymmetric part of the equation is the vorticity transport equation, which does not contain any pressure term; thus, the symmetric part of the equation can be isolated.

$$\frac{\mathrm{D}S_{ij}}{\mathrm{D}t} - \nu S_{ij,\,kk} + S_{ik}S_{kj} + \Omega_{ik}\Omega_{kj} = -p_{,ij} \ . \tag{2.25}$$

The first two quantities on the LHS of (2.25) represent the limitation of defining the vortex as a locus of static pressure minimum: a region of unsteady strain rate can generate local depressurization in the absence of swirl, and viscous dissipation of deformation work can nullify the pressure drop inside a swirling region[11]; neglecting these terms it is possible to write

$$S_{ik}S_{kj} + \Omega_{ik}\Omega_{kj} = -\,p_{,ij}\ . \tag{2.26}$$

that holds for phase-averaged results too; the average operator commutes with the spatial derivatives:

$$\bar{S}_{ik}\bar{S}_{kj} + \bar{\Omega}_{ik}\bar{\Omega}_{kj} = -\,\bar{p}_{,ij}\ . \tag{2.27}$$

The λ_2 model defines the vortex core as a connected region in which the tensor $S_{ik}S_{kj} + \Omega_{ik}\Omega_{kj}$ has 2 negative eigenvalues; the eigenvalues can be sorted $\lambda_1 \geq \lambda_2 \geq \lambda_3$, and COURANT and HILBERT [66] prove that:

$$\lambda_3 = -\frac{1}{4}\,||\omega||^2 \tag{2.28}$$

hence, the λ_2 method reduces to the condition

$$\lambda_2 < 0 \tag{2.29}$$

in a connected region.

The center of the TLV is located at the loci of relative minimum for λ_2 [12].

A 2D velocity field admits two eigenvalues $\lambda_2 \geq \lambda_3$, for such a flow, the condition $\lambda_2 < 0$ still holds.

The distance between the suction side tip edge and the TLV center is measured and normalized with the clearance width h. Results are presented in Fig. 2.52. The rate of vortex detachment from the suction side has two distinctly different linear trends, as illustrated by solid lines a) and b). The first extends up to $sc^{-1} = 0.5$, and the second faster vortex migration range extends up to $sc^{-1} = 0.83$. Fig. 2.52 illustrates the trend of the distance between the TLV and the SS edge both axially and radially; there exist three image vortices, but only the one located in the blade and the one located in the casing, just above the TLV induce a relevant motion on the TLV. Up to sc^{-1} 0.5, the dominant image vortex is located within the blade, i.e. the induced flow is mostly radial. Further downstream, the dominant image vortex is in the end wall casing, and the induced motion is axial. Consequently, the axial displacement rate changes drastically.

2.12 Circulation

In order to follow the evolution of the TLV strength, the circulation of the velocity is computed in the TLV section for each phase averaged velocity map, i.e. at each chord section. Fig. 2.53 show the trend of the TLV circulation as well as the strength of other vortical structure such as the vorticity sheet that connects the TLV to the suction edge of the blade, the trailing edge vortex - shed by the blade only for $sc^{-1} > 1$, and casing end-wall vorticity generated at the wall and entrained in the TLV perimeter.

[11] viscous phenomena are active at scales that are not resolved in the present investigation as the vector spacing is approximately 30 time larger than the inertial scale

[12] the distribution of vorticity in the core of the phase averaged TLV is Gaussian due to spatial average of a scattered distribution of instantaneous cores, the strain-rate at the center is negligible compared with the vorticity and the pressure Hessian reduces to $\Omega_{ik}\Omega_{kj}$; hence the problem reduces to the study of the square of vorticity, that evidences peaks better than vorticity

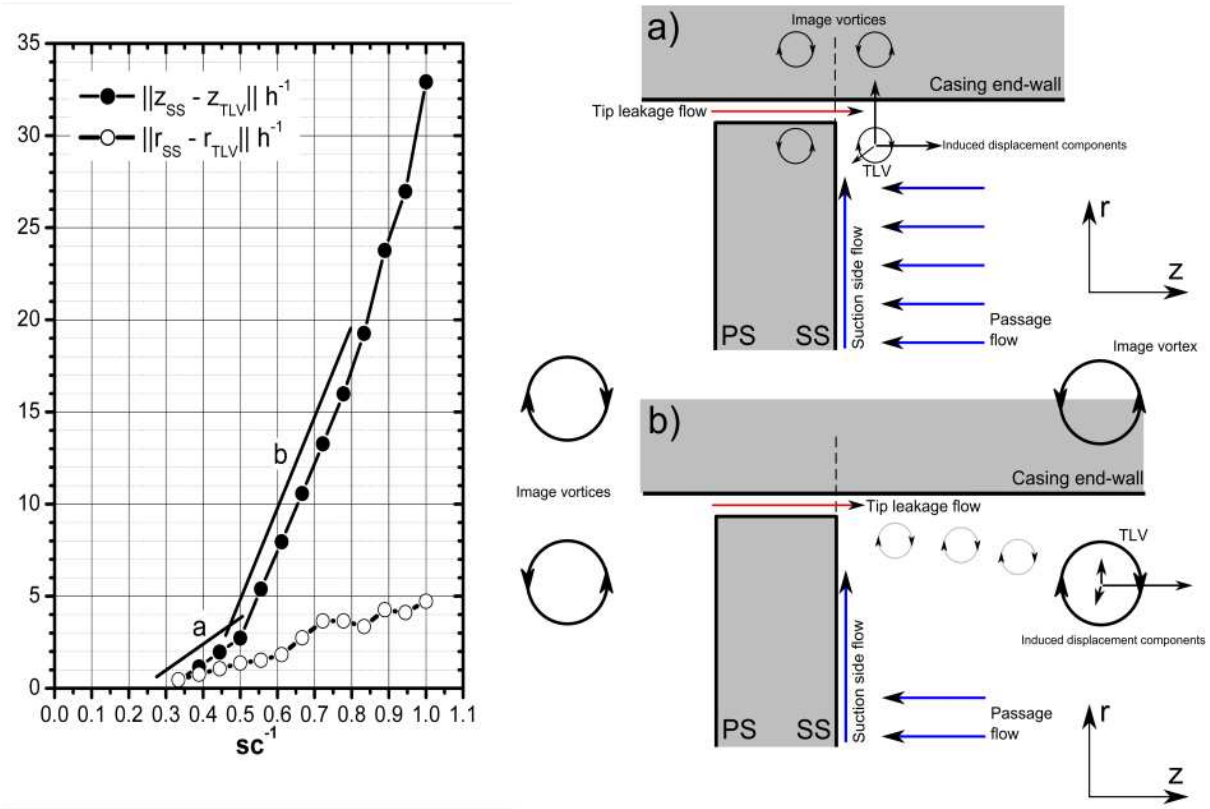

Figure 2.52: **Radial (a) and axial (b) migration rates for the TLV core respect with the suction side edge of the blade**

Circulation shown in the graph is the integration of the averaged velocity along the curves $\omega_\theta = -0.022$ for the zones with negative vorticity - TLV and vortex sheet - and $\omega_\theta = +0.022$ for the zones with positive vorticity such as the end-wall boundary layer and entrained vorticity. The threshold value is set analyzing the vorticity distribution in the rotor passage at progressively high threshold levels. If $-0.022 < \omega_\theta < +0.022$, no organized vortical structure can be recognized in the passage because of the noise due to the discrete differentiation of the velocity field, which is known to decrease the signal to noise ratio of measurements. The curves $\omega_\theta = \pm 0.022$ are reliable, simply connected path for the velocity integration[13].

The TLV circulation increases in the first part of the vortex evolution because the TLV is locked to the blade the formation of the vorticity layer is inhibited, thus the total vorticity coming from the blade tip is ingested by the vortex that grows quickly. At $sc^{-1} < 0.6$ the TLV center moves away from the surface of the blade with the same rate of its growth.

Once the distance is sufficiently large, the blade wall effect weakens and the TLV locks on the casing surface. As the image vortex moves from the blade section, the TLV starts moving downstream under the influence of the wall effect; because the blade section apparent motion is faster than the induced motion of the TLV, the distance between the vortex and the blade increases and there is enough space for the vorticity sheet to enlarge.

[13] because the vorticity is more noisy than the velocity, computing the circulation via integration of the velocity gives less uncertainty than integrating the vorticity over an area

A constantly elongating vortex sheet can accumulate vorticity without substantially transferring it to the TLV, hence the TLV strength reaches a plateau, while the strength of the layer increases almost linearly, exactly as the distance between the blade and the TLV; beyond the trailing edge, the circulation of the vortex sheet decays quickly because there is no blade feeding the process. At the same chord fraction, also the TLV circulation drops to zero quickly because the TLV bursts and two, in plane vorticity components subtract angular momentum to the out of plane vorticity previously contained in the TLV. The casing end-wall circulation increases with the strength of the TLV because the stronger the TLV, the higher the induced vorticity; but soon at $0.6 < sc^{-1} < 0.7$ it decays because the TLV keeps growing in a region bounded by the end-wall on the top. The distance between the TLV and the casing end-wall grows with the same rate of its radius growth and the wall effect diminishes, as well as the magnitude of the induced vorticity diminishes even though the TLV strength is stable. Beyond the trailing edge, the strength of the vortex sheet and TLV decays quickly.

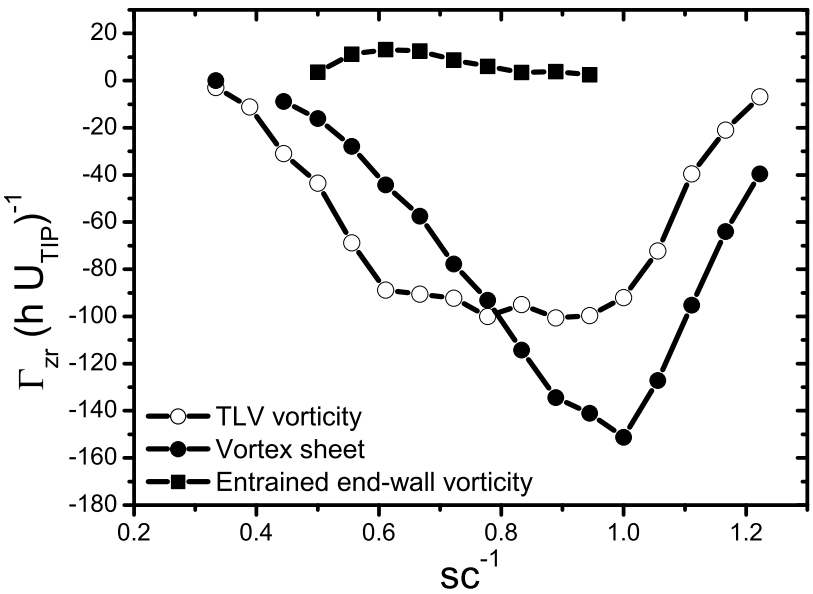

Figure 2.53: **Circulation of the main vortical structures in the passage at increasing chord fraction**

2.13 Turbulence in the TLV

Each of the N = 1000 instantaneous vector maps for each rotor phase phase give a fluctuating velocity map by subtracting the correspondent phase averaged velocity. The fluctuating velocity is defined with (2.30).

$$\mathbf{u}' = \mathbf{u} - \frac{1}{N}\sum_{i=1}^{N}\mathbf{u}_i \tag{2.30}$$

A surrogate for the normalized turbulent kinetic energy (TKE), based on the available in-plane velocity components, is k^*_{2D}, whose definition is illustrated in (2.31).

$$k^*_{2D} = \frac{1}{\bar{U}^2_{TIP}}\frac{1}{2}(\overline{u'_z u'_z} + \overline{u'_r u'_r}) \tag{2.31}$$

where the term $\overline{u'_r u'_r}$ is expected to be lower than $\overline{u'_z u'_z}$ and $\overline{u'_\varphi u'_\varphi}$, not measured in the present investigation.

Distributions of k^*_{2D} in selected planes are presented in Fig. 2.54. Note that the scales vary in order to highlight trends. At $sc^{-1} = 0.5$ (Fig. 2.54 (a)), the high turbulence on the pressure side of the blade is associated with bursting of the TLV in the previous passage. Turbulence is also large in the separating shear layer, which feeds vorticity into the TLV and near the point of boundary layer detachment at the end wall. The turbulence is also high along the tip gap boundary layers, and within the area occupied by the vortex. However, the k^*_{2D} peak is located to the right of the TLV center, compare to Fig. 2.50 (b), along the line of transporting of vorticity from the shear layer to the vortex core. Note that some of what is defined as turbulence here is a result of vortex rope meandering, i.e. it is dominated by large scale coherent motions, *not all the literature identifies this unsteadiness as turbulence.*

At $sc^{-1} = 0.72$ (Fig. 2.54 (b)), i.e. before bursting, the TKE is particularly high in the shear layer, and in the vicinity of the vortex center, where vortex ropes meandering is a significant contributor. However, the highest TKE zone starts at the point of end wall detachment, but extends into the area located at the transition between positive and negative vorticity layers. In this plane, the region of elevated TKE is still circular, consistently with the vortex still having a clearly defined, multi-rope core.

At $sc^{-1} = 0.94$ (Fig. 2.54 (c)), the large TKE region expands substantially, presumably due to vortex bursting, but the signatures of the shear layer extends from the tip, and the layer with elevated turbulence, that starts at the point of end wall boundary layer detachment, are still evident. The TKE peak in this plane is located at the same elevation but slightly to the left of the vorticity center (the latter is not shown). Only a short distance downstream, at $sc^{-1} = 1.0$ (Fig. 2.54 (d)), the elevated TKE area is substantially broader, and expands to the neighboring blade. The turbulence peak is also much wider but has lower magnitude, suggesting that transport, such as turbulent diffusion, plays an important role in this region. The TKE peak is again located slightly to the left of the TLV center. Since the end wall boundary layer no longer separates in this plane, and is fed instead into the tip clearance flow of the neighboring blade, the high TKE region extending from the end wall only a short distance upstream disappears.

At $sc^{-1} = 1.17$ (Fig. 2.54 (e)), there is a broad region of elevated turbulence with a peak that is clearly located to the left of the TLV, in a region containing vortex fragments located between the TLV and the shear layer. Turbulence is also high to the right of the point of TEV roll-up. Although the blade wake is noticeable, the turbulence there is significantly lower than that in the area dominated by remnants of the TLV.

With the present 2D data, many of the important contributors to turbulence production rate cannot be evaluated,

$$P = -\overline{u'_z u'_z}\bar{S}_{zz} - \overline{u'_r u'_r}\bar{S}_{rr} - \overline{u'_\theta u'_\theta}\bar{S}_{\theta\theta} - 2\overline{u'_z u'_r}\bar{S}_{zr} - 2\overline{u'_z u'_\theta}\bar{S}_{z\theta} - 2\overline{u'_r u'_\theta}\bar{S}_{r\theta} \tag{2.32}$$

for example, the shear production in the blade boundary layer, which is undoubtedly a major contributor. However, examination of some of the in-plane terms, i.e.

$$P^*_{2D} = \frac{h}{U^3_{TIP}}(-\overline{u'_z u'_z}\bar{S}_{zz} - \overline{u'_r u'_r}\bar{S}_{rr} - 2\overline{u'_z u'_r}\bar{S}_{zr}) \tag{2.33}$$

is quite insightful. A sample P^*_{2D} along with the three terms contributing to it is presented in Fig. 2.55. Note the differences in the contour levels.

This distribution corresponds to the TKE presented in Fig. 2.54. The distribution of P^*_{2D} (Fig. 2.55) peaks in the shear layer, where the shear production term is dominant (Fig. 2.55 (d)), as expected. In the region of end wall boundary layer detachment, axial

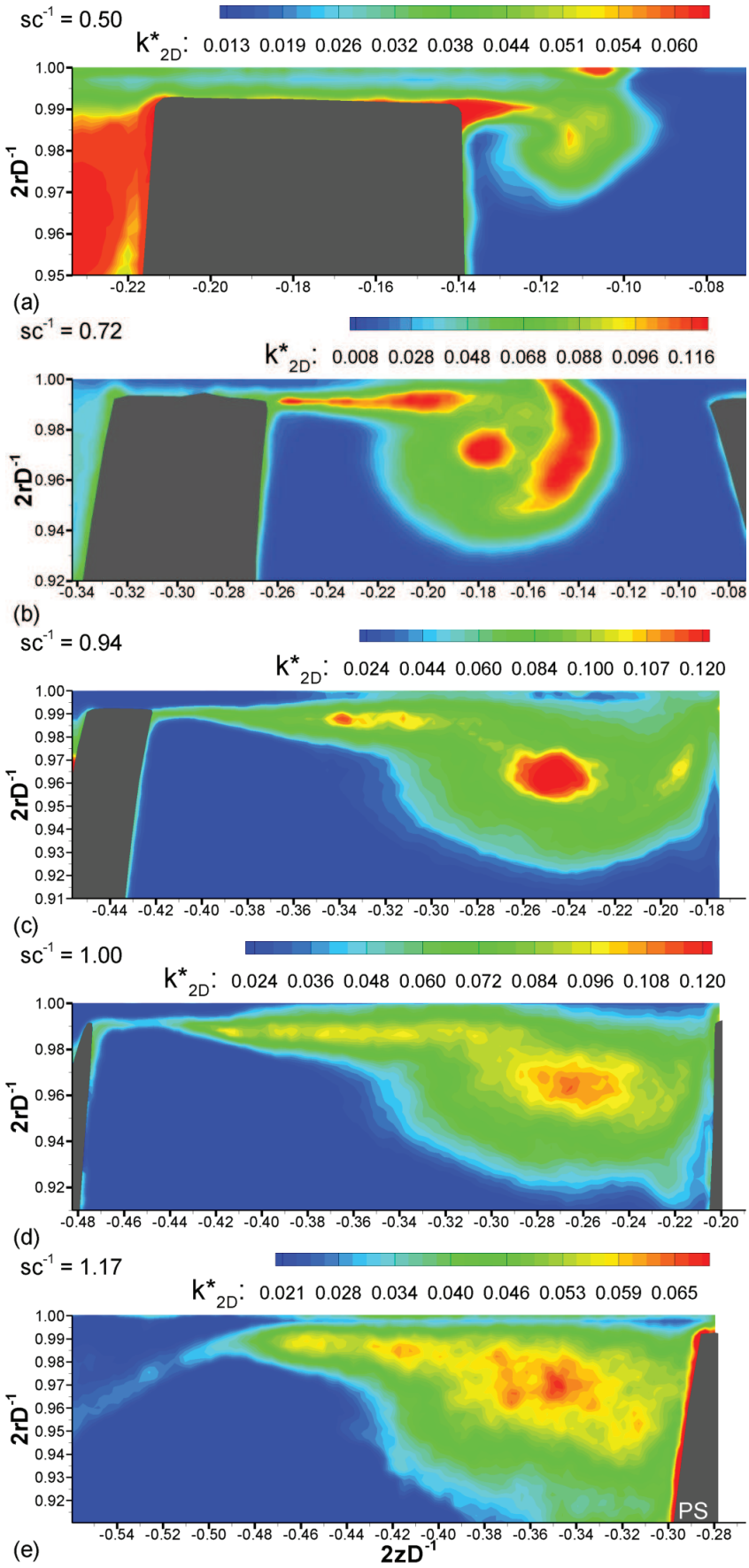

Figure 2.54: **Phase averaged planar turbulent kinetic energy at different, increasing chord-fractions**

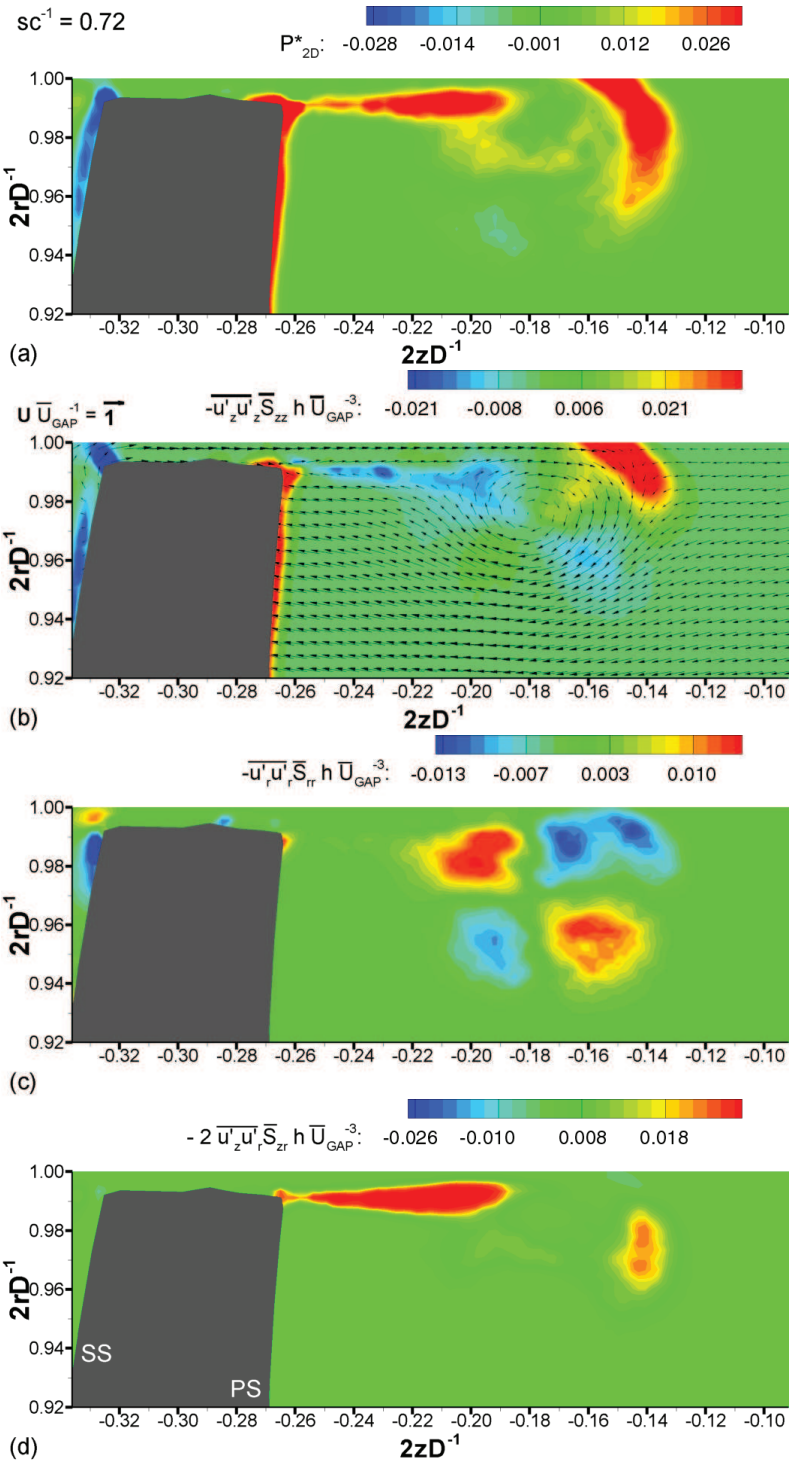

Figure 2.55: **Phase averaged planar production of 2D turbulent kinetic energy (a) and its component (b, c, d) at** $sc^{-1} = 0.72$

compression of the flow Fig. 2.55 (b) in the vicinity of the (2D) stagnation region is the main contributor to production, with radial extension reducing the magnitude of the overall in-plane production rate. Underneath this area, at the interface between positive and negative vorticity layers, shear production again plays a primary role. Stretching and compression in the region surrounding the vortex core generate peaks of alternating signs in the contributions of normal stress components. Overall, except for the end wall detachment point, the sum of these terms has little effect on P^*_{2D}.

Interestingly, P^*_{2D} is very low near the vortex center, where the TKE peaks. Effect of out of plane production (not shown), whose magnitude can be estimated as $k^*_{2D}(\bar{S}_{zz} +$

$\bar{S}_{\mathrm{rr}}$) is negligible, and cannot explain the discrepancy. This apparent disagreement must involve other turbulence sources. The first option is out-of-plane shear production due to gradients of the circumferential velocity component. The second possibility is turbulence transport into the vortex center from other areas by, e.g., entrainment of the shear layer or the detached end wall boundary layer. Present data cannot clarify this issue, future measurements in other planes as well as 3D measurements will address this issue.

Finally, in-plane stretching of the flow near the pressure side corner of the blade, which is not balanced by in-plane compression, results in a negative P^*_{2D}. Out-of plane shear production in the blade boundary layer is expected to be very high in this area, as well as circumferential compression, that must balance the in-plane stretching, most likely resulting in an overall positive production rate. Downstream of vortex bursting (not shown), P^*_{2D} is dominated by shear production in the shear layer extending from the blade tip. At $sc^{-1} = 1.17$, P^*_{2D} is much higher in the vorticity layer than in the blade wake, this is consistent with trends of the TKE distribution. Shear production is also elevated in the region of TKE peak, but is lower than that in the shear layer. Thus, turbulence transport must play a role here as well.

Because the production rate of TKE is a result of the interaction between unsteadiness and mean flow strain-rate field, it is worth to visualize how a fluid element is deformed along its trajectory, in order to justify the mechanism that enhances the TKE production. The strain-rate of a planar velocity field is a second order symmetric tensor, it can be diagonalized by rotation after having computed its eigenvectors. Then, the value of the eigenvalues are the principal component of the deformation, evaluated along the principal axis [67].

If the principal component of the strain-rate is negative in a point, there exist a direction over which the fluid element is compressed, if the principal component is positive the direction is called of stretching. In a 3D, incompressible flow there exist three principal directions and they cannot be all of compression or stretching. In a 2D flow there exist two principal direction and, if the flow is incompressible, principal deformations must be equal in module and opposite in sign. In a 2D subset of a 3D flow, and this is the presented case, there still exist two principal directions, but correspondent deformation rates can be different in module or even of the same sign indicating that locally there is out of plane deformation rate.

Fig. 2.56 shows the principal directions and deformations of the phase averaged flow at $sc^{-1} = 0.5$ near the entry section of the tip clearance. The principal direction are computed over selected points on streamlines. Because the flow is averaged in time, these streamlines coincide with trajectories; thus, fluid elements can be followed during the movement from the pressure side of the blade to the tip gap, and the variation of the induced deformation can be followed as well. First, the flow that enters the tip clearance is located at very high span and the phenomenon is very localized; the flow is pushed forward, see Fig. 2.56, right to left, by the pressure side of the blade, there is a strong stretching along the blade not compensate by enough compression perpendicularly to the wall, this can be explained first recalling that the boundary condition at the blade wall is $\mathbf{u} = U_{\mathrm{Blade}}(r)\mathbf{e}_\theta$, i.e. the velocity is purely circumferential and out of plane; in addition to that, the motion of the blade section is apparent, not material. Hence, the fluid element is not displaced by the apparent contact with the blade section but by the static pressure field induced by the aerodynamic effect of the three-dimensional blade.

In fact, strain and compression balance just a little far from the pressure side, as the fluid elements overturn to enter the clearance, as indicated by the vorticity peak always present at the pressure edge in Fig. 2.50 at each rotor phase. The overturn of the flow enhances the strain rate field because the flow is forced to enter a very narrow gap. The directional plot of the strain rate field helps understanding the peak of negative

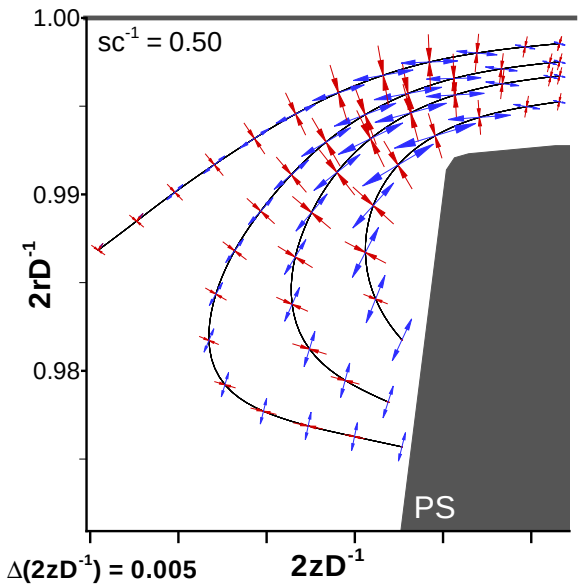

Figure 2.56: **Mean flow principal direction of the strain-rate, compression and extension directions are shown over some streamlines**

production noticeable at the pressure edge in Fig. 2.55; production is the composition of the Reynolds stresses and the mean flow strain rate field. Analyzing the phenomenon in the strain rate principal frame of reference has one great advantage: the strain rate tensor is diagonal and so the contribution of the turbulent shear stresses is null. Hence, the turbulent stresses that induce the production are solely the ones aligned with the strain rate principal directions, which vary point to point.

Fig. 2.56 shows clearly that the strain field aligns with the pump frame of reference at the clearance inlet section, exactly in the point where the strain field has also a peak, the enhancement of the strain rate combines with the stresses $\overline{u'_z u'_z}$ and $\overline{u'_r u'_r}$ while $\overline{u'_z u'_r}$ is inhibited by the absence of the extra-diagonal strain term. Because both $\overline{u'_z u'_z}$ and $\overline{u'_r u'_r}$ are positive, the sign of the production of TKE is related to the sign of the strain-rate components.

When the flow leaves the pressure side, the turbulent stress $\overline{u'_z u'_z}$ is damped by the no-slip boundary condition on the pressure side, the $\overline{u'_r u'_r}$ prevails and combines with the local stretching that is approximately oriented as the radial coordinate. As a result, the production rate is negative. Conversely, as the flow crosses the tip gap entry section, it is realigned axially. There, the radial unsteadiness is inhibited by the presence of the casing wall and the tip surface while the $\overline{u'_z u'_z}$ can combine with the now axially-oriented stretching giving, again, negative production.

Justifying the trend of the production of TKE in the TLV is more difficult than at the clearance inlet due to the presence of multiple phenomena confined in a narrow space.

Fig. 2.57 describe the phase averaged strain rate field in terms of principle directions and principle components over selected TLV streamlines. As the flow exits the tip clearance, the strain-rate is low and almost isotropic, its peaks in the shear layer that connects the TLV with the suction edge o the blade. There, the strain rate tensor is 45°-oriented as it should be in a pure shear deformation; in fact, the shear layer is a zone of intense production due to shear, see Fig. 2.55 (d).

As the tip gap back-flow jet collides with the forward passage flow at point B in Fig. 2.57, the axial compression is activated but the flow is substantially 2D, at least sufficiently far from the end-wall; as a result, because of incompressibility, stretching is

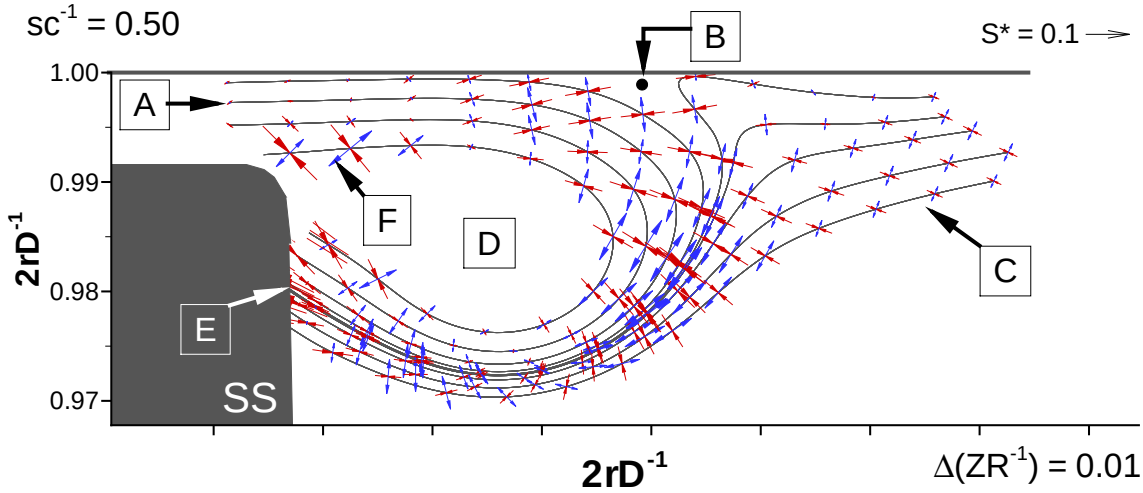

Figure 2.57: **Mean flow principal direction of the strain-rate, compression and extension directions are shown over some streamlines; A: Tip clearance flow, B: collision between the clearance jet and the forward flow, C: passage flow, D: TLV core, E: flow "compressed" over the suction side, F: pure deviatoric deformation in the shear layer**

also enhanced. Strain rate principle directions are again aligned with the pump frame of reference. It can be stated that locally, at point B, $\overline{u_r' u_r'}$ is small because of the presence of the end wall; on the other hand, $\overline{u_z' u_z'}$ is free to combine with the axial compression giving a peak of positive production, see Fig. 2.55 (a) and (b). The front of interaction between the TLV and the passage flow hosts a peak of production due to localized shear production, Fig. 2.55 (d) because the Reynolds stress tensor and the strain-rate tensor are rotated and the angle is approximately 45°.

The center of the TLV is a low strain rate zone, as the center of a vortex should be, this is the reason why the very turbulent core, see Fig. 2.54, does not host a production peak; hence, the TKE peak is only due to the so called "pseudo-turbulence", induced by the averaging of flow structures, the TLV vortex ropes, whose dynamic is extremely under-sampled in time and that are not the same entity. It is worth to highlight that, if a proper time scale is chosen, the "pseudo-turbulence" is in fact turbulence that generates, for example, noise and vibrations.

2.14 Conclusions

The investigation is focused on instantaneous phase averaged flow structures and associate turbulence in the passage of an axial water jet pump rotor. The mean circumferential vorticity gives insights into the structure and strength of vortical flows in the passage, such as the vortex sheet originated at the tip suction edge, the tip leakage vortex (TLV), the separated end wall boundary layer and the trailing edge vortex. The vortex sheet keeps ingesting vorticity from the suction edge, its circulation increases while its length and thickness also increase, and then circulation drops down at the trailing edge.

The strength of the tip leakage vortex keeps increasing from the initial roll up to 60% of the chord, where it reaches a plateau and then drops to nearly zero at the trailing edge, the circulation associated with the detached end wall vorticity is much lower than of the TLV and also decays faster.

The vorticity/shear layer and the point of end wall vorticity detachment are highly turbulent, as well as the region of transition between the TLV outer branch (negative vorticity) and the detached and entrained positive vorticity. The evaluation and the comparison of the contributors to the in-plane production of turbulent kinetic energy show that the vortex sheet is a source of shear production, as well as the transition zone at the outer branch of the TLV.

Mean flow compression is prominent at the end wall, where the boundary layer vorticity detaches; as a result, large, positive production rate is found there. The center of the TLV is also largely turbulent but the in-plane production is low there, the presented 2D data cannot describe the phenomenon completely, this open issue is to be further investigated with 3D measurements.

2.15 Future developments

The 2D approach has large limitations in an axial turbomachine because the flow is always three-dimensional. Although the plane investigated in this work has been chosen wisely in order to evaluate the evolution of the TLV, some issues about the circumferential velocity flux in the core or the alignment of vorticity at the suction edge of the blade are still unsolved. Moreover, the TLV is induced by the tip clearance back-flow, whose structure is not resolved properly in the present work due to insufficient spatial resolution.

The next step will be the investigation of the tip gap flow again with 2D-PIV in the meridional plane, using high magnification lenses in order to fit ten to twelve vectors within the gap width. Those results will shed light over the gap flow radial velocity profile and over the phenomena that occur on the flow as it exits the clearance.

A further analysis will be carried out with the stereoscopic PIV to understand the influence the circumferential momentum has on the realignment of vorticity that originated the TLV.

The stereoscopic PIV cannot provide instantaneous, circumferential velocity gradients; if a large number of STEREO-PIV velocity maps are sampled on many rotor angular position, to achieve a suitable angular resolution, the circumferential velocity gradient can be computed but averages in time are unavoidable and only the mean flow can be investigated. Moreover, large sets of stereoscopic PIV involve are extremely time costly, and require large data store capability.

In order to measure the 3D velocity in a sub-region of the pump inner space and compute the instantaneous, three-dimensional velocity gradient, the tomographic PIV system should be adopted, see §I. At the time of this writing, only few research centers and institutions are able to perform such a measurement, and only on straight channels; this technique will be available to study turbomachinery flows in the future.

Bibliography

[1] Blanco *et al.*: *Fluid-Dynamic Pulsations and Radial Forces in a Centrifugal Pump with Different Impeller Diameters*; Proc. ASME FEDSM2005-77361, 2005

[2] Wang, and Tsukamoto: *Experimental and Numerical Study of Unsteady Flow in a Diffuser Pump at Off-Design Conditions*; Journal of Fluids Engineering, **125**, pp. 767-778, 2003

[3] Ullum *et al.*: *Prediction of Rotating Stall within an Impeller of a Centrifugal Pump Based on Spectral Analysis of Pressure and Velocity Data*; Journal of Physics, **52**, pp. 36-45, 2006

[4] Pavesi *et al.*: *Time-Frequency Characterization of Rotating Instabilities in a Centrifugal Pump with a Vaned Diffuser*; Proc. ISROMAC 12-2008-20135, 2008

[5] Menter, F. R.: *Two-Equation Eddy-Viscosity Turbulence Models for Engineering Applications*; AIAA Journal, **32(8)**, 1994, pp. 1598-1605

[6] Shi F., and Tsukamoto H.: *Numerical Study of Pressure Fluctuations Caused by Impeller-Diffuser Interaction in a Diffuser Pump Stage*; ASME Journal of fluids Engineering, **123**, pp. 466-474, 2001

[7] Sano T., Yoshida Y., Tsujimoto Y., Nakamura Y., and Matsushima T.: *Rotor-Stator Interactions, Turbulence Modeling and Rotating Stall in a Centrifugal Pump with Diffuser Vanes*; ASME Journal of fluids Engineering, **124**, pp. 363-370, 2002

[8] Majidi K.: *Numerical Study of Unsteady Flow in a Centrifugal Pump*; ASME Journal of Turbomachinery, **127**, pp. 363-371, 2005

[9] Johansson P.B.V., and George W.K.: *Numerical Study of Unsteady Flow in a Centrifugal Pump*; ASME Journal of Turbomachinery, **127**, pp. 363-371, 2005

[10] Prasad A.K.: *Stereoscopic particle image velocimetry*; Experiments in Fluids, **29**, pp. 103-116, 2000

[11] Ye Pu and H. Meng: *An advanced off-axis holographic particle image velocimetry (HPIV) system* ; Experiments in Fluids, **29**, pp. 184-197, 2000

[12] Elsinga G. E., Scarano F., Wieneke B., van Oudheusden B. W: *Tomographic particle image velocimetry*; Experiments in Fluids, **41**, pp. 933-947, 2006

[13] Sinha: *Rotor-Stator Interactions, Turbulence Modeling and Rotating Stall in a Centrifugal Pump with Diffuser Vanes*; PhD dissertation, Johns Hopkins University, 1999

[14] Benrha et al.: *Measurements of the Periodic Flow Field in a Radial Diffuser Pump by the PIV-Method*; Proc. ASME FEDSM2007-37400, 2007

[15] Dupont et al.: *Rotor-Stator Interactions in a Vaned Diffuser Radial Flow Pump*, Proc. ASME FEDSM2005-77038, 2005

[16] Wuibaut et al.: *PIV Measurements in the Impeller and the Vaneless Diffuser of a Radial Flow Pump in Design and Off-Design Operating Conditions*, ASME Journal of fluids Engineering, **124**, pp. 791-797, 2002

[17] Chow et al.: *Flow Nonuniformities and Turbulent "Hot Spots" Due to Wake Blade and Wake Wake Interactions in a Multi Stage Turbomachine*, ASME Journal of fluids Engineering, **124**, 553-560, 2002

[18] Gnata: *Analisi del flusso instazionario in un diffusore di pompa centrifuga mediante misure PIV in fase*; Grad. Thesis - Politecnico di Milano - 2007.

[19] Stepanoff, A. J.: *Centrifugal and Axial Flow Pumps: Theory, Design and Application*; John Wiley & Sons Inc; 2nd edition

[20] Raffel, Kompenhans: *article Image Velocimetry: A Pratical Guide*; Springer

[21] Li, Y. S., and Cumpsty, N. A.: *Mixing in Axial Flow Compressors: Part I - Test Facilities and Measurements in a Four-Stage Compressor*; 1991, ASME Journal of Turbomachinery, **113**, pp.161-165

[22] Li, Y. S., and Cumpsty, N. A.: *Mixing in Axial Flow Compressors: Part II - Measurements in a Single-Stage Compressor and a Duct*; 1991, ASME Journal of Turbomachinery, **113**, pp.166-174

[23] Khalid, S. A., Khalsa, A. S., Waitz, I. A., Tan, C. S., Greitzer, E. M., Cumpsty, N. A., Adamczyk, J. J., and Marble, F. E.: *Endwall Blockage in the Axial Compressor*; 1999, ASME Journal of Turbomachinery, **121**, pp.499-509

[24] Denton, J. D.: *Loss Mechanism in Turbomachines*; 1993, ASME Journal of Turbomachinery, **115**, pp.621-656

[25] Goto, A.: *Three-Dimensional Flow and Mixing in an Axial Flow Compressor with Different Rotor Tip Clearances*; 1992, ASME Journal of Turbomachinery, **114(3)**, pp.675-685

[26] Farrell, K. J., Billet, M. L.: *A Correlation of Leakage Vortex Cavitation in Axial Flow Pumps*; 1994, ASME Journal of Fluids Engineering, **116**, pp.551-557

[27] You, D., Wang, M., Parviz, M., and Rajat, M.: *Vortex Dynamics and Low-Pressure Fluctuations in the Tip-Clearance Flow*; 2007, ASME Journal of Fluids Engineering, **129(8)**, pp.1002-1014

[28] Adamczyk, J. J., Celestina, M. L., and Greitzer, E. M.: *The Role of Tip Clearance in High-Speed Fan Stall*; 1993, ASME Journal of Turbomachinery, **115**, pp.28-39

[29] Offenburg, L. S., Fischer, J. D., and Hoek, T. J. V.: *An Experimental Investigation of Turbine Case Treatments*; 1987, Paper No. AIAA-87-1919.

[30] Behr, T., Kalfas, A. I., and Abhari, R. S.: *Control of Rotor Tip Leakage Through Cooling Injection From the Casing in a High-Work Turbine*; 2008, ASME Journal of Turbomachinery, **130**, pp. 031014-1 - 031014-12.

[31] Watanabe, S., Seki, H., Higashi, S., Yokota K., and Tsujimoto, Y: *Experimental Modeling of 2-D Leakage Jet Cavitation as a Basic Study of Tip Leakage Vortex Cavitation*; 2001, ASME Journal of Fluid Engineering, **123(1)**, pp. 50-56.

[32] Kimura, T., Yoshida, Y., Hashimoto, T., Shimagaki, M: *Numerical Simulation for Vortex Structure in a Turbopump Inducer: Close Relationship with Appearance of Cavitation Instabilities*; 2008, ASME Journal of Fluid Engineering, **130**, pp. 051104-1 - 0501104-9.

[33] Shen, Y. T., Gowing, S., and Jessup, S.: *Tip Vortex Cavitation Inception Scaling for High Reynolds Number Applications*; 2008, ASME Journal of Fluid Engineering, **131**, pp. 071301-1 - 071301-6.

[34] Sanders, A. J., Papalia, J., and Fleeter, S.: *Multi-Blade Row Interactions in a Transonic Axial Compressor: Part I - Stator Particle Image Velocimetry (PIV) Investigation*; 2002, ASME Journal of Turbomachinery, **124**, pp. 10-18.

[35] Liu, B., Wang, H., Liu, H., Yu, H., Jiang, H., and Chen, M: *Experimental Investigation of Unsteady Flow Field in the Tip Region of an Axial Compressor Rotor Passage at Near Stall Condition with Stereoscopic Particle Image Velocimetry* 2004, ASME Journal of Turbomachinery, **126**, pp. 360-374.

[36] Sinha, M., Pinarbasi A., and Katz J.: *The Flow Structure During Onset and Developed States of Rotating Stall Within a Vaned Diffuser of a Centrifugal Pump*, 2001, ASME Journal of Fluid Engineering, **123**, pp. 490-499.

[37] Oweis, G. F. and Ceccio, S. L.: *Instantaneous and Time-Averaged flow Fields of Multiple Vortices in the Tip Region of a Ducted Propulsor*; 2005, Experiments in Fluids, **38**, pp. 615-636.

[38] Oweis, G. F., Fry, D., Chesnakas C. J., Jessup S. D., and Ceccio S. L: *Development of a Tip-Leakage Flow Part 1: The Flow Over a Range of Reynolds Numbers*; 2006, Journal of Fluids Engineering, **128**, pp. 751-764.

[39] Oweis, G. F., Fry, D., Chesnakas C. J., Jessup S. D., and Ceccio S. L: *Development of a Tip-Leakage Flow Part 2: Comparison Between the Ducted and Un-ducted Rotor*; 2006, Journal of Fluids Engineering, **128**, pp. 764-773.

[40] Boccazzi, A., Miorini, R., Sala, R., and Marinoni F: *Unsteady flow field in a radial pump vaned diffuser*; 2009, Proc. the 8th European Turbomachinery Conference, F. Heitmeir et al., eds.

[41] Dazin, A., Cavazzini, G., Pavesi, G., Dupont, P., Coudert, S., Ardizzon, G., Caignaert, G., Bois, G.: *Rotating Instabilities in a Radial Vaneless Diffuser. Part I: High Speed Stereoscopic Measurements*; 2009, Proc. the 8th European Turbomachinery Conference, F. Heitmeir et al., eds.

[42] Uzol, O., Chow Y. C., Katz J., and Meneveau C: *Unobstructed PIV Measurements within an Axial Turbo-Pump Using Liquid and Blades with Matched Refractive Indices*; 2002, Experiments in Fluids, **33(6)**, pp. 909-919

[43] Rains, D. A.: *Tip Clearance Flows in Axial Flow Compressors and Pumps*; 1954, California Institute of Technology, Hydrodynamics and Mechanical Engineering Laboratories, Report No. 5.

[44] Lakshminarayana, B.: *Methods of Predicting the Tip Clearance Effects in Axial Flow Turbomachinery*; 1970, ASME J. Basic Eng., 112, pp. 609-617.

[45] Chen, G. T., Greitzer, E. M., Tan, C. S., and Marble, F. E: *Similarity Analysis of Compressor Tip Clearance Flow Structure*; 1970, ASME Journal of Turbomachinery, **113**, pp. 260-271.

[46] Chen, G. T., Greitzer, E. M., Tan, C. S., and Marble, F. E: *Similarity Analysis of Compressor Tip Clearance Flow Structure*; 1970, ASME Journal of Turbomachinery, **113**, pp. 260-271.

[47] Fan, S., Lakshminarayana B., and Barnett, M: *Low Reynolds Number k-ε Model for Unsteady Turbulent Boundary-Layer Flows*; 1990, AIAA J., **28**, pp. 1707-1717.

[48] Gerolymos, G.A., and Vallet, I.: *Tip-Clearance and Secondary Flows in a transonic Compressor Rotor*; 1999, ASME Journal of Turbomachinery, **121**, pp. 751-762.

[49] Launder, B. E., and Sharma, B. I.: *Application of the Energy Dissipation Model of Turbulence to the Calculation of Flows Near a Spinning Disk*; 1974, Lett. Heat Mass Transf., **1**, pp. 131-138.

[50] Jones, W.P., and Launder. B. E.: *The Prediction of Laminarization with a 2-D Equation Model of Turbulence*; 1972, Journal of Heat and Mass Transf., **15**, pp. 301-314.

[51] Furukawa, M., Inoue, M., Saiki, K., and Yamada, K: *The Role of Tip Leakage Vortex Breakdown in Compressor Rotor Aerodynamics*; 1999, ASME Journal of Turbomachinery, **121**, pp. 469-480.

[52] Storer, J. A., and Cumpsty, N. A.: *Tip Leakage Flow in Axial Compressors*; 1991, ASME Journal of Turbomachinery, **113**, pp. 252-259.

[53] Dring, R. P., Joslyn, H. D., and Hardin, L. W.: *Tip Leakage Flow in Axial Compressors*; 1982, ASME Journal of Engineering for Power, **104(1)**, pp. pp. 84-96.

[54] Dring, R. P., Joslym H. D., and Wagner, J. H.: *Compressor Rotor Aerodynamics and Viscous Flow Effects in Turbomachines*; 1983, AGARD-CP-351, Paper No. 24, Copenhagen, Denmark.

[55] Xiao, X., McCarter, A. A. and Lakshminarayana, B: *Tip Clearance Effects in a Turbine Rotor: Part I Pressure field and Loss*; 2001, ASME Journal of Turbomachinery, **123**, pp. 296-304.

[56] McCarter, A. A., Xiao, X. and Lakshminarayana, B: *Tip Clearance Effects in a Turbine Rotor: Part II Velocity Field and Flow Physics*; 2001, ASME Journal of Turbomachinery, **123**, pp. 305-313.

[57] Stauter, R. C.: *Measurement of the Three-Dimensional Tip Region Flow Field in an Axial Compressor*; 1993, ASME Journal of Turbomachinery, **115**, pp. 28-39.

[58] Zierke, W. C., Farrell, K. J., and Straka W. A: *Measurements of the Tip Clearance Flow for a High-Reynolds-Number Axial-Flow Rotor*; 1995, ASME Journal of Turbomachinery, **117**, pp. 522-532.

[59] Soranna, F., Chow, Y., Uzol, O., and Katz, J.: *Rotor Boundary Layer Response to an Impinging Wake*; 2004, ASME Journal of Turbomachinery, Proceedings of ASME Heat Transfer/Fluids Engineering Summer Conference, Charlotte, NC, July 11-15.

[60] Soranna, F., Chow, Y., Uzol, O., and Katz, J.: *The Effect of Inlet Guide Vanes Wake Impingement on the Flow Structure and Turbulence Around a Rotor Blade*; 2006, ASME Journal of Turbomachinery, **128**, pp. 82-95.

[61] Soranna, F., Chow, Y., Uzol, O., Katz, J.: *Evolution of Flow Structure and Turbulence around a Rotor Blade due to Interaction with the Non-Uniform Strain Field Generated by Upstream Blades*; 2006, 26th Symposium on Naval Hydrodynamics, Rome, Italy, Sep. 17-22.

[62] Wu, H., Soranna, F., Michael, T., Katz, J. and Jessup, S: *Cavitation in the Tip Region of the Rotor Blades within a Waterjet Pump*; ASME Fluid Engineering Conference.

[63] Roth G. I., and Katz, J.: *Five techniques for increasing the speed and accuracy of PIV interrogation*; 2001, Meas. Sci. Technol., **12**, pp. 238-245.

[64] [16] Tan, S., 2006, *Three-dimensional and Tip Clearance Flows in Compressors in Advances in Axial Compressor Aerodynamics* Von Karman Institute for Fluid Dynamics, Lecture Series 2006-06.

[65] Jeong, J., and Hussain, F.: *On the Identification of a Vortex*; 1995, Journal of Fluid Mechanics, **284**, pp. 69-94.

[66] Courant, R., and Hilbert, D.: *Methods of Mathematical Physics*; vol. 1, Interscience.

[67] Moore, J. G., Schorn, S. A., and Hussain, F.: *Methods of Classical Mechanics Applied to Turbulence Stresses in a Tip Leakage Vortex*; 1996, Journal of Turbomachinery, **118**, pp. 622-629.